Investigating the Role of Particle Engineering and Excipients in the Processability of Pepsin Powder

Implications for Powder Flow and *in vitro* Dissolution in Parenteral Protein Formulations

Derya Özsökmen Hick

LUND
UNIVERSITY

Investigating the Role of Particle Engineering and Excipients in the Processability of Pepsin Powder
Implications for Powder Flow and *in vitro* Dissolution in Parenteral Protein Formulations

Published by
Department of Process and Life Science Engineering
Faculty of engineering LTH, Lund University
P.O. Box 118, SE-221 00 Lund, Sweden

Subject: KLGM06 Degree Project in Pharmaceutical Formulation

Division: Department of Process and Life Science Engineering

LU Supervisor: Stephen Burleigh

Novo Nordisk Supervisors: Zacharias Brimnes Visby Damholt and Jari Pekka Pajander

Examiner: Marie Wahlgren

Investigating the Role of Particle Engineering and Excipients in the Processability of Pepsin Powder

by

Derya Özsökmen Hick

Process and Life Science engineering

June 2026

LU Supervisor: Stephen Burleigh

Novo Nordisk Supervisors: Zacharias Brimnes Visby Damholt and Jari Pekka Pajander

Examiner: Marie Wahlgren

How Powder Particles affect a Drug's Success

Only about 10% of drug products that enter human critical trials ever receive approval for further production. Surprisingly, the problem is often not the drug itself but whether it can be turned into a product that behaves properly during manufacturing.

Many medicines are produced as powders that need to pass through various manufacturing steps before they can reach patients. During production, it is important that the powder flows smoothly through equipment, mixes evenly and is stable during storage. If the particles stick together, absorb too much moisture or behave unpredictably, manufacturing can slow down or fail completely. Processability problems like these cost pharmaceutical companies both time and money, which can delay important medicines from reaching patients.

To improve how powders behave, pharmaceutical companies often add substances called excipients. Two common examples are mannitol and lactose monohydrate. These ingredients can help protect sensitive drug compounds and make manufacturing easier and at the same time, they can also change the properties of the powder.

In this project, a model protein called pepsin was mixed with mannitol or lactose monohydrate to change its size, shape and surface structure, all of which had a major impact on processability. To modify the powder, spray drying was used, which is a process where liquid droplets are dried into small particles.

The results from the study showed that spray drying made the powder stickier and more humid, which affected how it flowed and dissolved. Overall, it was the size, shape and surface structure of the particles what had the biggest impact on processability. The powders with mannitol showed the best flow and dissolution compared to those with lactose. Interestingly, even powders that looked very similar still behaved different just because of small changes to their surface structure.

The main conclusion is that there is not a magic recipe to make the perfect pharmaceutical product so instead it's important to carefully choose the process to make the powder, the excipients that are added, the shape of the particles, and other powder properties. By applying these findings to other protein-based medicines, researchers may be able to design drug products that are easier to produce, more stable and quicker to reach the patients who need them.

Abstract

Pharmaceutical manufacturing of parenteral injections must be fine-tuned to yield a stable API through efficient production methods. Assessing a products processability is essential to ensure consistent manufacturing and safe drug administration, of which powder flowability and dissolution both have a direct impact. Spray drying is a particle engineering technique to modify these parameters, however, the relationship between spray drying conditions, particle properties and processability is not completely understood.

Spray drying was investigated as a particle engineering technique to determine its effects on the processability of protein powders. Pepsin was used as a model protein API to explore how both spray-drying conditions and excipient selection, specifically mannitol and lactose monohydrate, influence powder processability. The powders were produced with different spray drying conditions to generate samples with different particle size, morphology and solid-state properties. Processability was evaluated through powder flowability via ring shear testing and bulk and tap density measurements, and *in vitro* dissolution in PBS (pH 7.4, 15 °C). These results were supported by BET surface area analysis and inverse gas chromatography (iGC) for surface energetics.

Spray drying produced amorphous samples which altered their hygroscopicity, surface area and cohesive behaviour. Mannitol-containing formulations showed the best flowability attributed to their spherical morphology and moderately high surface energy, while lactose-containing samples exhibited the poorest flow due to creased morphology and high total surface energy. From analysis of spearman correlation results, surface energetics proved to be the strongest predictor of flowability, while particle morphology was the best determinant of dissolution, with porosity and surface roughness enhancing wetting. Water content analysis was able to connect spray drying conditions, agglomeration and processability results.

All in all, there is no single parameter governing powder processability and it was instead the combination of morphological differences, excipient type, water content and surface energetics what affected powder performance. This emphasizes the importance of solid-state characterization when optimizing spray-dried formulations for pharmaceutical manufacturing.

Acknowledgements

I would like to thank first and foremost all my supervisors for all their support. To my Lund University supervisor; Stephen Burleigh, and my supervisors at Novo Nordisk; Zacharias Brimnes Visby Damholt, PhD, and Jari Pekka Pajander, PhD. Your help, patience and invaluable knowledge is something I am very lucky to have experienced. I would also like to thank Georgia Kasten Korgaard for teaching me the ins and outs of spray drying, and to team PaC at Novo Nordisk for welcoming me so warmly and having me as one of your own; to Sarah Kelly Mortensen for instilling confidence in me from the beginning, as well as to all chemists and lab technicians in the team including; Annette Breest, Anna Esben Esbensen, Johan Peter Bøtker, Karina Sørensen, Linnea Norrbohm Byrnard, Lone Overgaard Andersen, Mai Akkarya Saen-arj Nielsen, Malene Hillerup Byskov, Paolo Lucaioli, and Keyoomars Khorami. The knowledge sharing, coffee chats and laughs throughout these past few months have made all the difference.

None of my successes would have been possible without the wholehearted support from my family since the beginning, especially that of my mom, my dad and my brother. Your support and encouragement throughout the years have been my motivation. And to my life partner, Juan, thank you for being my biggest cheerleader always, I look forward to continuing witnessing each other's successes.

This thesis represents the culmination of my studies to this date as well the end to this two-year master's program that I have enjoyed so much. Much of this is thanks to all the amazing people I have met throughout my time in Lund, and that will remain as lifelong friends for years to come. You all know who you are, thank you for being there and making this time so special.

Finally, thank you to anyone reading this thesis. May this be a reminder to everyone to chase your dreams and that anything is possible if you put your mind to it!

Best,

Derya Özsökmen Hick

Table of Contents

Abbreviations

API	Active Pharmaceutical Ingredient
BET	Brunaeur-Emmett-Teller
DSC	Differential Scanning Calorimetry
DVS	Dynamic Vapor Sorption
FFC	Flow Function Coefficient
GI	Gastrointestinal
HTS	High-Throughput Screening
ID	Intradermal
iGC	Inverse Gas Chromatography
IM	Intramuscular
IV	Intravenous
PBS	Phosphate-Buffered Saline
pH	Potential of Hydrogen
PSD	Particle Size Distribution
RH	Relative Humidity
RST	Ring Shear Tester
SC	Subcutaneous
SE	Surface Energy
SEM	Scanning Electron Microscopy
Tg	Glass transition temperature
TGA	Thermo-gravimetric Analysis
TM-DSC	Temperature-modulated DSC
UV	Ultraviolet
USP	United States Pharmacopeia
XRPD	X-ray Powder Diffraction

1. Introduction

Pharmaceutical manufacturing enables the mass production of drugs through a series of complex processes that transform raw compounds into safe drug products. Among these processes, spray drying is one of the particle engineering techniques which can be used to make changes to material properties. It converts liquid solutions into dry powders through atomization by pressurized air, followed by drying via heating (Milanesi et al., 2025). As these droplets form and dry quickly, the spray-drying settings strongly influence what kind of particles are produced and the overall process often helps improve stability, storage and ease of transport. This is particularly relevant for protein-based therapeutics, where maintaining stability is a key challenge.

In spray-dried protein formulations the performance of the final product and the processability of the powder are two different but interrelated parameters. These, however, can at times overlap, as poor processability can compromise the efficacy and quality of the final drug product. For powders to be successfully manufactured and administered they must be easily processable, meaning they should flow, mix, disperse and dissolve in a predictable way (Shah et al., 2023). Poor processability can lead to manufacturing problems like inconsistent powder handling and challenges during reconstitution, such as poor wetting or incomplete dispersion (Tharanon et al., 2024).

Powder processability is closely linked to particle properties such as particle size distribution, particle morphology and the way particles pack together, which affect how strongly particles interact with each other (referred to as cohesion) and how easily the powder moves under stress (adhesion) ("Particle, Powder, and Compact Characterization," 2017). Powder properties also influence reconstitution as dissolution depends on how quickly liquid can access and interact with the particle surfaces. According to the Noyes-Whitney equation, particle size is connected to surface area, and it thereby influences dissolution rate, which further affects the administration of the drug (Bansal, 2002). Two critical processability attributes for parenteral application are dissolution rate and powder flowability (Bansal, 2002). Dissolution rate is critical to ensure complete and homogeneous reconstitution of the protein prior to injection, while powder flowability impacts consistency of vial filling during manufacturing.

Particle size alone does not determine powder behaviour. The powder matrix formed by the addition of excipients also plays a major role in how the powder interacts with water and how it behaves. Therefore, this work considers the following two excipient systems: Mannitol and Lactose monohydrate. Among saccharides used as excipients in spray-dried protein pharmaceutical formulations, mannitol and lactose both have high prevalence, accounting for ~ 80% and ~20% use respectively (Pinto et al., 2021). Both have shown evidence of improved flowability, stability of the protein formulation and prevent protein unfolding during drying by serving as a protective matrix (Zhang et al., 2020). As these excipients differ in their solid-state characteristics, moisture interactions, thermal properties and surface energetics, variations in these can lead to difference in the final powder performance, even when particle size is modified in a similar manner.

In this thesis, particle properties are varied by changing spray-drying conditions such as inlet temperature and feed rate. This thesis will use pepsin as a model molecule for protein active pharmaceutical ingredients (APIs) used for parenteral dosing due to their extensive use in Novo Nordisk ®. The goal is to generate pepsin powders that differ in particle size distribution and then evaluate how those differences translate into changes in processability, as measured by the powder dissolution and flow. The central question is how changing the particle properties of the powder, in combination with the type of excipient used (mannitol vs lactose monohydrate), affect the processability of pepsin-containing powders.

Processability is evaluated using a set of measurements that connect powder mechanics and reconstitution performance. Powder flow is assessed using ring shear testing, supported by bulk and tap density. For reconstitution-related behaviour, processability is investigated using dissolution in Phosphate Buffered Saline (PBS) (pH 7.4, 15 ℃). To help interpret the observed performance, the powders also undergo extensive solid-state characterizations and inverse gas chromatography (iGC) for surface interaction-related properties.

2. Aims of thesis

The aim of the project is to explore the effect of addition of different excipients and altering particle size on powder processability by using spray drying as the particle engineering method. The main goal of the thesis will be to provide scientific knowledge to apply the findings to other protein parenteral formulation systems. The main hypotheses this paper will explore are:

1. Changing spray-drying conditions and adding excipients alters the processability of pepsin powder.
2. Powders with smaller particle size and thereby higher surface area will show reduced flowability.
3. The processability of formulations containing mannitol versus lactose monohydrate will be different due to excipient-dependent differences in solid-state properties.
4. Powders with high surface area will exhibit a faster dissolution, indicating improved wetting.
5. An increase in moisture content will affect processability by altering particle surface interactions.

3. Theoretical Background

3.1.Parenteral drug formulation

Parenteral drugs involve administration of a therapeutic by injection or infusion that bypasses the gastrointestinal (GI) tract, thereby evading the first-pass metabolism ("Drug Delivery," 2023). Orally available drugs often exhibit a reduction in concentration before reaching circulation due to prior metabolism in the liver or intestines after administration. The typical parenteral routes include, intravenous (IV), intramuscular (IM), subcutaneous (SC) and intradermal (ID) injections (Holm, 2024). All of these achieve higher bioavailability due to more rapid entry into circulation, defined by the fraction of an administered dose that reaches systemic circulation in an unchanged form (Price & Patel, 2026). Parenteral administration allows for faster onset of action, better control over dosage and facilitates intake of poorly soluble drugs (Kwatra et al., 2012).

The formulation of parenteral products also presents significant challenges as the systems must meet specific requirements for sterility, stability and safety. As described in the United States Pharmacopeia (USP), parenteral preparations can be classified into five major types (USP, 2016):

1. Injection: liquid drug substance ready for injection
2. For injection: dry solid that upon mixture yields a liquid solution that is ready for injection
3. Injectable emulsion: liquid drug substance dissolved or dispersed in emulsion medium
4. Injectable suspension: ready-to-use suspension preparation
5. For injectable suspension: dry solid requiring reconstitution into suspension

Powder-based parenteral formulations, including dry powders for injection, are commonly employed when the API exhibits limited stability in solution (Emami et al., 2023). These can exist in both a crystalline and amorphous state. The former is when molecules are arranged in a highly ordered and three-dimensional lattice structure and the latter is a disordered arrangement (Greene, 2021). Crystalline solids are known to be more thermodynamically stable, they exhibit a defined melting point and are less susceptible to changes in moisture content. While amorphous solids exist at a higher energy state and are less stable but have better dissolution than crystalline ones (Valenti et al., 2021).

In the case of amorphous solids, they have a glass transition temperature (Tg) which is the temperature at which the material transforms from a glassy state to a rubbery state (Greene, 2021). Below their Tg, the molecules are less mobile while above Tg, molecular mobility increases which facilitates relaxation and crystallization. Samples should ideally be stored below their Tg to minimize solid-state transformations (Greene, 2021). Moisture is a factor that must also be considered as water acts as a plasticizer which can reduce intermolecular interactions and lower the Tg, resulting in lower mobility (Yang et al., 2005).

3.2.Processability of powder formulations

The top three reasons that lead to drug product recall include; 1) the product not having uniform amounts of API, 2) the API within each product unit do not dissolve at the required rate, and 3) an unsuitably high concentration of impurities (Hamad et al., 2010). All of these affect the manufacturing efficiency, product quality, and therefore, the overall processability of the drug product. Processability refers to the ability of a powder system to be handled, mixed, transported and filled in a reproducible manner (Shah et al., 2023). Particle size distribution, morphology, density and surface properties all influence powder behaviour during processing, including its flowability, compressibility, cohesion and adhesion. Understanding these characteristics is particularly important for formulations with excipients such as mannitol and lactose, as one must maintain stability while enhancing processability.

Inadequate flow behaviour can lead to inconsistent filling of vials, reduced dosing accuracy and inefficiencies, such as slow processing and clogging when scaling up the process (Tharanon et al., 2024). Additionally, it can increase the likelihood of powder retention within equipment, leading to product loss. Poor flowability can arise from small particle size, irregular particle shape or strong interparticle forces such as van der Waals interactions (Shah et al., 2023). These interparticle forces can be categorized as cohesion, occurring between particles of the same material, or adhesion, occurring between particles and surfaces such as equipment walls.

Dissolution describes the ability of a powder to interact with and become uniformly dispersed in a liquid medium (Tinke et al., 2009). It can be understood by a series of steps; 1) wetting and immersion of a particle surface by the dissolution medium, 2) liquid penetration into pores or interparticle spaces driven by capillary pressure and surface energy, and 3) surface dissolving and dispersing, where drug molecules at the particle surface dissolve and diffuse into the medium (Bansal, 2002). Hydrophobic particle surfaces or inadequate wetting conditions can lead to incomplete dispersion and formation of aggregates (He et al., 2008). This in turn can compromise the dissolution rate and lead to uneven dosage and decreased product performance (Karde & Ghoroi, 2014). The wettability of powders is strongly influenced by surface chemistry, particle morphology and the presence of excipients.

Due to the significant impact of these processability challenges on powder handling and product quality, it is essential to control particle characteristics. Particle engineering techniques are commonly employed to modify surface properties, and thereby improve powder flow, wettability and overall processability.

3.3.Particle engineering

Particle engineering is an important step that is necessary to produce the most optimal pharmaceutical product. Many different methods exist (Table 3.1) and the choice of method depends on the route of administration, dosage and components within the parenteral formulation.

Table 3.1. Different particle engineering techniques often used for pharmaceutical formulations.

Property	Effect
Size reduction and milling	Milling techniques enable uniformity and controlled dissolution of drug particles. The milling design decides the particle size and morphology of the powder (T. Mehta et al., 2025). Stabilizers include polymers and surfactants to enhance bioavailability.
Granulation	Granulation transforms fine powders into free-flowing granules that have high compressibility (Shanmugam, 2015). The two types are; wet and dry, and the choice of which process to use depends on the drug properties.
Fluidized bed processing	This method produces drug-polymer layered composites or coat carrier particles with nanosuspensions. They are also used for amorphous solid dispersion preparation which controls solvent exposure and drying kinetics (Bhakay et al., 2018).
Crystallization	Crystallization focuses on controlling polymorphism, particle size, shape and porosity through transformations and evaporation (Ragab & Rohani, 2009). It can yield large porosity and low surface-energy particles which often reduces aggregation.
Supercritical fluid-assisted methods	Supercritical fluid technology is a sustainable particle engineering method which has precise control over size, morphology and crystallinity (Tabernero et al., 2012). It works at low temperatures which is ideal for unstable compounds. Supercritical carbon dioxide acts as a solvent which forms uniform small particles ranging from 5 μm – 500 nm in size (Tabernero et al., 2012).
Melt-based processes	These include hot-melt extrusion, melt granulation, and melt-based coating, and all create particles by heating a formulation above the melting point. The melt solidifies into droplets, granules or rods which are later milled into powders (Rajeshwari et al., 2020).
Freeze drying	Freeze drying transforms dissolved or suspended material into a solid powder through freezing. As temperature drops, the solvent used crystallizes and under vacuum, ice sublimates, leaving a cake or solid powder. It is often used to preserve fragile molecules (Jakubowska & Lulek, 2021).

3.3.1. Spray Drying

Spray drying is a continuous process which converts liquid feed into a dry powder through the rapid evaporation of solvent (Milanesi et al., 2025). The process of drying involves several key stages: (1) atomization of the feed into fine droplets, (2) the droplets come into contact with the drying gas, which is heated at a desired temperature, (3) evaporation of the solvent and drying of the droplets, and (4) separation and collection of the dried powder as seen in *Figure 1.1* (Milanesi et al., 2025).

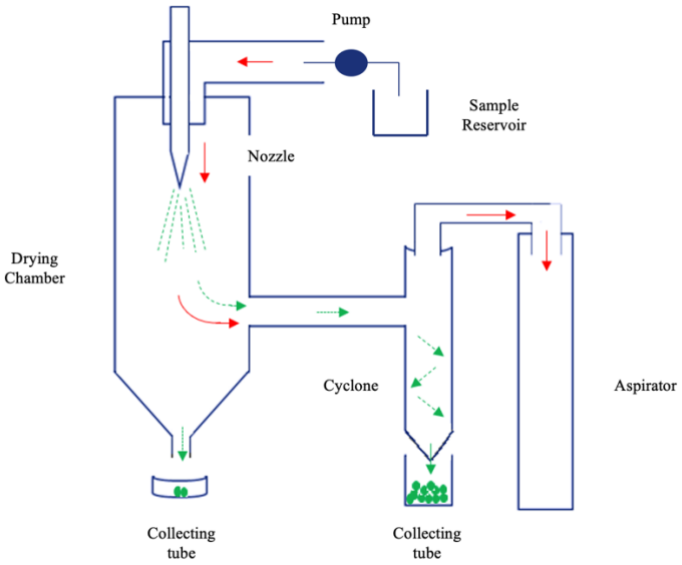

Figure 1.1. Schematic diagram of a spray dryer where the red arrows indicate the direction of drying gas and the green arrows indicate the direction of product.

Through drying, protein powders often show increased stability, improved shelf-life and there is easier adjustment of particles for the route of administration (Emami et al., 2018). The versatility of spray drying makes it useful for pharmaceutical applications, as the process parameters can be changed to achieve a powder with the desired properties (Table 3.2). These could include morphology, particle size, moisture content and glass transition temperature (Tg) (Ziaee et al., 2020).

Table 3.2. Spray drying properties that can be changed to yield different powder characteristics.

Property	Effect
Atomization	Atomization breaks down liquid feed into smaller droplets, determining their size and size distribution. The type of atomizer that is used (rotary atomizer, two-fluid nozzle, pressure nozzle or ultra-sonic nozzle), and the atomization setting influence particle size, morphology and bulk density of the final product (Milanesi et al., 2025).
Drying gas temperature	Higher temperatures reduce particle size by lowering the surface tension and accelerating drying which leads to particle collapse (Bałdys et al., 2025).
Feed rate	Higher feed flow rate leads to increased average particle density (Bałdys et al., 2025). Feed rate also influences the time of droplets in the drying cyclone which affects the degree of drying and morphology.
Feed concentration	Concentrations of solids in feed solution should be maintained below 30% w/v for optimal spray drying (Bałdys et al., 2025). Higher concentrations can lead to nozzle blockage and higher degree of sticking in the cyclone walls.
Drying rate	Drying rate describes how fast the solvent evaporates from the droplets during drying, which is affected by the temperature, humidity, droplet size and surface area. Incomplete drying can cause sticking of the droplets to the wall of the dryer (Wahab et al., 2025).
Outlet temperature	A lower outlet temperature may result in higher moisture which affects product stability (Masum et al., 2020).
Inlet temperature	Influences evaporation rate of the solvent (Masum et al., 2020).
Solvent type	This choice affects drying rate, particle morphology and levels of residual solvent in the final product. Organic solvents generally evaporate faster than water which can alter particle characteristics (Dedroog et al., 2022).

3.4.Methods for the characterization of powder pharmaceuticals

Many different methods exist to characterize pharmaceutical powders, whether that be in terms of solid-state properties including particle size, morphology and crystallinity or bulk behaviour, with dissolution and flowability analyses.

3.4.1. Solid-state characterization methods

Thermal

Thermal characterization methods aim to analyse how heat affects materials and to determine the phase change temperatures which are both helpful to determine the contents of powder material ("Powder Characterization—Methods, Standards, and State of the Art," 2021). Two complementary techniques that do such are Thermo-gravimetric analysis (TGA) and Differential scanning calorimetry (DSC). In both TGA and DSC, the sample is measured against an inert reference sample ("Powder Characterization—Methods, Standards, and State of the Art," 2021). The former yields a thermogram, which represents the sample mass change versus temperature or time. This curve is unique for each compound and gives information about thermal stability, oxidative stability, and moisture and volatility content (Saadatkhah et al., 2020).

Once the thermal stability of the sample is noted from the aforementioned technique, a DSC analysis can be run to detect specific interactions within the sample (Rastegari et al., 2017). During measurement, the temperature of the sample changes at a different rate from the reference which can give information on whether a thermal events such as crystallization, freezing, melting, dehydration or glass transition. A variation of this technique is temperature-modulated DSC (TM-DSC) which involves temperature modulation over time alongside the regular temperature ramp ("Solid-State Characterization and Techniques," 2017). The difference between them is that the regular DSC uses a linear heating rate while TM-DSC uses a sinusoidal heating rate which separates the total heat flow into heat-capacity component and a kinetic component (Thomas et al., n.d.). This allows for better separation of transitions such as glass transition which can be hard to detect when the sample contains many components.

Crystal Structural

During formulation of a pharmaceutical powder, the structural components of the materials help determine their processability. Crystal structure determines the effect of specific particle engineering techniques and therefore, determine its effectiveness. X-ray (powder) diffraction (XRPD) is a method that achieves this aim. The working principles involve a beam of X-rays directed on the crystalline solid which diffracts due to the crystalline planes inside the solid, into discrete peaks ("Powder Characterization—Methods, Standards, and State of the Art," 2021). The diffraction pattern can be used as a fingerprint to distinguish polymorphs of a molecule.

Closely related to the structure, is the crystal density of the sample. This measurement, often determined through helium pycnometry, can determine the density of a crystalline material and is crucial for analysing molecular packing. The sample is weighed and then placed in the sample holder which is then dosed with helium at a specific pressure (Nguyen et al., 2019). The volume of the sample (V_s) can then be determine based on the change in pressure, the reference volume and the sample mass (m_s) which is used to calculate the crystal density using Equation 1 (Nguyen et al., 2019).

$$\rho_s = \frac{m_s}{v_s} \quad (1)$$

Particle Size and Morphology

The particle size and morphology can also be altered using particle engineering techniques. Scanning electron microscopy (SEM) employs an electron beam to scan the surface and determine the number of electrons hitting the sample surface. This is then detected and converted into an image ("Solid-State Characterization and Techniques," 2017).

Particle size distribution (PSD) apparatus can then be used to determine the size of said sample. It provides information about average particle size, size distribution and shape by using laser diffraction ("Particle, Powder, and Compact Characterization," 2017). The light scattering pattern obtained is proportional to the particle diameter that produces the pattern. The particle size information given by this apparatus includes percentile descriptors like D10, D50 and D90 which represent the particle diameter below which 10%, 50% and 90% of the sample volume falls.

Hygroscopicity and Water Content

Dynamic vapor sorption (DVS) can determine how rapidly and how much water a sample sorbs at specific relative humidity (RH) levels ("Solid-State Characterization and Techniques," 2017). This gives important information about the hygroscopicity of the material which then in turn indicates the stability of samples and informs on the selection of storage conditions. The relative humidity in the sample chamber is controlled and the effect of changes to the RE is observed as a mass change of the sample ("Solid-State Characterization and Techniques," 2017).

Similarly, Karl Fisher titration can be employed to determine the total water content of a sample. The titration is performed volumetrically when a large amount of water is present in the sample, and methanol is commonly used in the presence of a base and iodine ("Solid-State Characterization and Techniques," 2017). One disadvantage that this method offers is the lack of distinguishing between surface water and water as part of the sample structure.

3.4.2. Methods to characterize bulk behaviour

Powder flowability assessment: Ring Shear Tester and Tapped & Bulk Density

Flowability is affected by particle size, moisture content, particle size distribution, morphology and surface energy (Tay et al., 2017). In general, literature reports that smaller particles (<20 µm) lead to increased surface properties, including van der Waals forces which results in decreased flow (Visser, 1989). This phenomenon is an important one to analyse as it affects the manufacturing process of a pharmaceutical.

Methods for characterizing the flowability of powder can be divided into two main groups, static and dynamic. Those that are static involve a fixed powder bed such as in tapped and bulk density while dynamic methods characterize the powder while in motion, like shear cell methods (Tharanon et al., 2024). While both offer equally valuable information about the flow conditions of a system and are often performed complementarily, static methods are best for predicting behaviour in storage and cohesive forces, which is the focus at hand (Krantz et al., 2009).

Bulk density measures the density of loose powder poured into a glass container, which can be calculated using Equation 2, where V_0 represents the untapped apparent volume, and M is the sample mass (Chan & Heng, 2005). Therefore, both offer complementary results, with the former taking into account any gaps in the powder and the latter considering the non-compacted version.

$$Bulk\ density\ \left(\frac{g}{mL}\right) = \frac{M}{V_0} \tag{2}$$

Tap density can be described as the bulk density of a compacted powder after it has been tapped to minimize gaps and is a function of particle shape, porosity and particle size distribution ("Particle, Powder, and Compact Characterization," 2017; "Powder Characterization—Methods, Standards, and State of the Art," 2021). The sample mass is divided against a final constant tapped volume (V_f), after increasing tapping, to calculate the density ("Particle, Powder, and Compact Characterization," 2017).

$$Tapped\ density\ \left(\frac{g}{mL}\right) = \frac{M}{V_f} \tag{3}$$

Both the compressibility index, or Carr Index, and the Hausner Ratio can be calculated to compare these two results, as seen in Equation 4 and 5, respectively (Montanari et al., 2017).

$$Carr\ index = \frac{\rho_{B max} - \rho_{B min}}{\rho_{B max}} \times 100 \tag{4}$$

$$Hasuner\ ratio = \frac{tapped\ density\ (\rho_{B max})}{bulk\ density\ (\rho_{B min})} \times 100 \tag{5}$$

Powders with lower bulk density show larger Carr index and Hausner Ratio which indicate poor flowability due to a higher degree of cohesion between particles, as shown in Table 3.3 (Montanari et al., 2017).

Table 3.3. Ranking of flow by compressibility index and Hausner ratio (Powder Flow, 2024).

Compressibility index (%)	Type of Flow	Hausner Ratio
1-10	Excellent	1.00 -1.11
11-15	Good	1.12-1.18
16-20	Fair	1.19-1.25
21-25	Passable	1.26-1.34
26-31	Poor	1.35-1.45
32-37	Very poor	1.46-1.59
>38	Very, very poor	>1.60

In order to more accurately assess powder flowability under common powder processing conditions, ring shear cell testing is often used as it measures cohesion and friction under controlled stresses (Tharanon et al., 2024). The instrument works by filling a shear cell with powder and first undergoing a pre-shear test where the top of the powder is sheared under normal stress (P_{pre}). After such, the P_{pre} is lowered and the powder is sheared further by unidirectional rotation of the shear cell (C. Wang et al., 2022). The powder is sheared until failure, and the procedure is repeated several times until a yield locus is determined, which describes the strength of a bulk solid (Y. Wang et al., 2016). This can also be explained by the relationship between normal stress and resulting shear stress at different degrees of powder consolidation.

The result obtained from plotting the yield locus are the major principal stress (σ_1), representing the largest normal stress acting on the sample at a particular point which happens without shear stress, and the unconfined yield strength (σ_c) (C. Wang et al., 2022). This is the stress at which a sample that has undergone P_{pre} will fail when no confinement is applied. The flow function coefficient (*FFC*) is shown below in Equation 6.

$$FFC = \frac{\sigma_1}{\sigma_c} \tag{6}$$

The *FFC* values represent different types of flow, an *FFC* < 2 represents very cohesive flow; 2-4 cohesive flow; 4-10 easy-flowing; and >10 if for free-flowing powder ("Bulk Flow Optimisation of Amorphous Solid Dispersion Excipient Powders through Surface Modification," n.d.) .

In vitro Dissolution

As introduced, wettability and solubility directly influence dissolution rate, all of which are critical parameters affecting processability (Lu et al., 2014). More specifically, a products' dissolution profile is affected by other powder properties including particle size, surface area and morphology, and is best explained through the Noyes-Whitney equation (Hamad et al., 2010).

$$\frac{dC}{dt} = (\frac{DA}{Vh})(C_S - C)$$

(7)

This equation shows that the dissolution rate (*dC/dt,* $mol \cdot L^{-1} \cdot s^{-1}$) depends on the diffusion coefficient (*D,* $m^2 \cdot s^{-1}$)), the surface area (*A,* m^2), the thickness of the diffusion layer (*h,* m), the solubility of the drug (C_S, $mol \cdot L^{-1}$), the bulk concentration (C, $mol \cdot L^{-1}$) and the volume of solution (*V, L*) (Hamad et al., 2010). This describes *in vitro* dissolution which allows to imitate dissolution performance in the human body. As described by USP, solid dosage forms can be analysed through four different apparatus: basket, paddle, reciprocating cylinder and flow-through cell (USP, 2011). The method that is used for the present study involves the paddle, where the sample is placed in a bath with media and ultraviolet (UV) detection is used to calculate the concentration at different timepoints (Laitinen et al., 2010). The information obtained from a dissolution curve will be able to give information about the speed at which a dosage form releases the API into a medium.

Wettability itself is a factor governing how readily dissolution occurs and can be characterized through surface energy determination (Forny et al., 2011). This parameter determines physiochemical properties which includes wettability as well as adhesion, flowability, packing, and many more (Karde & Ghoroi, 2014). As the polar component (γ_p) of surface energy increases, wettability increases, meaning powder particles will have higher affinity for water leading to improve solid-liquid interaction (Karde & Ghoroi, 2014).

Surface Area and Surface Energetics

The surface area and surface energy of a powder govern how a particle interacts with its surrounding environment, other particles, excipients and processing equipment. Surface area is often quantified using the Brunauer-Emmett-Teller (BET) method. This method is able to measure surface area by measuring the amount of gas that is adsorbed onto the surface of a sample (Giesche, 1998). By knowing the size of the nitrogen molecule and assuming monolayer conditions, the size of the surface area can be determined (Giesche, 1998). BET surface energy is relevant in the context of dissolution, which as explained directly influences the dissolution rate as described previously by Equation 7.

Surface energy describes the excess energy present at the surface of a material relative to its bulk, arising from molecular interactions at the solid-vapor layer (Das et al., 2011). It is important in determining wettability, adhesion, cohesion, flowability and packing. To determine the total solid surface energy (γ), the sum of dispersive (γ_d) and polar components (γ_p) is taken (Das et al., 2011).

$$\gamma_d + \gamma_p = \gamma$$

(8)

Both surface area and surface energy can be characterized using inverse gas chromatography (iGC), which is regarded as one of the most accurate and sensitive methods compared with the contact angle approach (Karde & Ghoroi, 2014). In iGC, the powder sample is placed in a silanized glass column, which serves as the stationary phase. A series of volatile probe molecules are injected via a carrier gas, typically helium, at a controlled flow rate. The results will show different retention times based on the interactions between the stationary phase and the volatile substance (Mohammadi-Jam & Waters, 2014). A key advantage of iGC over contact angle measurements is that it analyses the bulk powder instead of a flat surface, making it more representative. Further, iGC can detect surface heterogeneity and can detect subtle differences in surface chemistry (Karde & Ghoroi, 2014).

4. Materials and Methods

4.1. Materials

The model protein used was Pepsin (Sigma-Aldrich, ≥400 units/mg protein). USP grade Mannitol (Pearlitol® 200 GT – Mannitol) and Lactose monohydrate (InhaLac® 160) were used as received. All excipients were stored at room temperature while the pepsin was stored in the fridge at 4 °C.

4.2. Methods

The following identifier numbers were given to each of the samples as seen in Table 4.1. To prepare the spray-dried solutions, 60g of pepsin were combined with 5g of the excipient in 1200 mL deionized water with NaOH to adjust to pH 12 to ensure dissolution.

Table 4.1. Summary of samples.

Sample	Formulation	Spray-drying temperature condition
Raw Pepsin	Non-spray-dried pepsin	N/A
S1.1	Spray dried 5% w/v pepsin	Low
S1.2	Spray dried 5% w/v pepsin	High
S2.1	Spray dried 5% w/v pepsin: mannitol (70:30 w/w)	Low
S2.2	Spray dried 5% w/v pepsin: mannitol (70:30 w/w)	High
S3.2	Spray dried 5% w/v pepsin: lactose monohydrate (70:30 w/w)	High

4.2.1. Particle engineering: Spray drying

Spray drying was conducted on a Buchi ® Mini Spray Dryer S-300 with a two-fluid nozzle using the conditions written below (Table 4.2). The drying was carried out at 21 °C room temperature and 23% RH.

Table 4.2. Spray drying parameters for the different sample conditions.

Parameter	Sample				
	S1.1	S1.2	S2.1	S2.2	S3.2
T_{in} (°C)	93	115	140	130	125
T_{out} (°C)	52	57	77	70	70
T_{cond} (°C)	7	7	16	16	16
Nitrogen (m^3/h)	22	23	24	23	23
$Qfeed$ (mL/min)	3	6	4.5	5.5	6
$Qatom$ (L/h)	800	650	800	650	650
Feed (mL)	1200				

Spray dried powder was collected and stored in 150 mL Duma ® bottles. After spray-drying, all samples underwent secondary drying in a desiccator until RH% was below 10%. The dehydrating agent used was phosphate pentoxide. After the desired RH% was reached, the bottles were placed in crimped aluminium bags with a 10g desiccant sachet (Supelco ®) to preserve the humidity.

4.2.2. Particle characterization

Thermo-gravimetric Analysis (TGA)

The thermal degradation of the compounds was determined through use of a TA Instruments Discovery ® TGA 5500. The samples were placed in a platinum pan and weighed, followed by heating at a rate of 10℃/min with a temperature range of 25-250 ℃.

Differential Scanning Calorimetry (DSC) and Temperature-modulated DSC (TM-DSC)

Thermal properties were evaluated via DSC using a TA Instruments Discovery ® DSC 2500. The samples were placed on a T-zero aluminium pan with T-zero lid and weighed. The amount of sample used was 6-8 mg. The temperature procedure used was 25-250℃. To determine the Tg of spray-dried powders, TM-DSC were conducted with a temperature procedure of -25-175℃ with heating at a rate of 5℃/min.

X-ray Powder Diffraction (XRPD)

The crystal form of both pepsin, mannitol and lactose monohydrate were determined with a Malvern Panalytical ® Empyrean. Between 10-15 mg of sample was placed on a High Throughput Stage (HTS) 96well without needing prior sample preparation. The method employed ran from 2-40 2Theta (º) for a total of 20 minutes per sample.

Pycnometry

Prior to taking measurements of crystal density, samples were placed for two days in a desiccator. The density measurements were made by using an AccuPyc III (Micromeritics ®). About 500 mg of each sample was measured in the sample holder, pressed down, and covered with a lid to then be placed inside the instrument.

Particle Size Distribution (PSD)

Particle Size Distribution (PSD) was performed using a Mastersizer 3000+ Ultra Aero S (Malvern Panalytical ®). Prior to analysis, each sample is tumbled at least 10 times and around 200 mg of samples are used per measurement, equivalent to three spatula scoops. To determine the PSD of each sample, two measurements were taken of each, using the method shown below.

Table 4.3. Description of the main parameters used to run PSD on all samples

Parameter	Set Point
Dispersion Unit	Aero S
Particle Type	Non-spherical particles
Refractive Index	1.56
Background measurement duration	10 s
Sample measurement duration	10 s
Dispersion pressure	2 Barg
Feed rate	40%
Hopper gap/slit width	1.50 mm
Sample amount	200 mg

Scanning Electron Microscopy (SEM)

To evaluate particle morphology Scanning Electron Microscopy (SEM) using a Phenom ProX G7 Desktop SEM (ThermoFisher Scientific ®) was performed. The sample was stuck to a circular shelf using an adhesive carbon tab. The images were acquired at a magnification of 2900x and 750x with a minimum detection size of 2.5%.

Dynamic Water Vapor Sorption (DVS)

Dynamic Water Vapor Sorption was performed on a ProUmid ® SPS Moisture Sorption Analyzer was employed. Around 110 mg of each sample was weighed and placed in the metal crucibles inside the 23-sample dish alongside a reference crucible. The samples were dried at 25 °C and 0% RH for 17 hours and then subjected to 10°C steps from RH 0% to 80%. The weighing interval was set to 10 minutes, and the equilibrium condition (dm/dt) was 0.0100% per 40 minutes.

Karl-Fischer Titration

The Metrohm ® KF titration system with tiamo ™ software was used for Karl Fisher measurements. Samples are tumbled several times before being weighed and crimped in glass tubes (Metrohm ®). An oven temperature of 100 °C with a start operation criterion of 15 µg/min was used.

***In vitro* Dissolution**

Dissolution tests were performed on the powder using the parameters described below (Table 4.4). The system used was Distek ® Opt-Diss 410 UV meter, fiber optic cables, probes with 1mm pathlength and the 2500 Select bath (Distek ®). Each of the samples was weighed individually and then dropped manually in the dissolution baths at the same time.

Table 4.4. Description of the parameters employed to perform dissolution studies on all samples.

Parameter	Set Point
Dissolution medium	50 mM PBS buffer pH 7.4
Apparatus	USP Apparatus II
Agitation rate	25 rpm
Analytical method	UV, 205 nm
Temperature	15 ℃
Volume	500 mL
Mass to dissolve	1 g

Ring Shear Tester

A Ring Shear Tester (RST) of the brand Dietmar Schulze, model/type: RST-XS.s was employed to test for flowability with a stress walk program. Each powder sample was tumbled 15-20 times and then spread in a shear cell (V=30 mL, maximum particle size < 1000 μm) and distributed evenly using a scraper. Shear testing was conducted at three normal stresses during preshear: 1500, 2500, 4000 Pa, where four shear-to-failure points were measured, corresponding to 50%, 65%, 80% and 50% of the normal stresses. Each sample resulted in one replicate with three yield loci per sample which was used to plot flow function curves.

Bulk & Tapped Density

A Sotax ® tapped density tester TD 1 was used to determine the bulk/tap density of all samples after Ring Shear Tester was run. Approximately 4g of each sample was used and the tap frequencies tested were 0, 500, 1250 and 2500.

Brunauer-Emmett-Teller (BET) Surface Area

The surface area of the spray dried powder was measured using the BET instrument TriStar II Plus 3030 from Micromeritics. Prior to analysis of the sample, the Smart VacPrep instrument from Micromeritics was used to degas the sample to remove any loose molecules. The sample was degassed at 80 ℃ for 300 minutes using nitrogen gas. Approximately 1 g of sample was used to perform the analysis.

Inverse Gas Chromatography (iGC)

To perform analyses on the surface area and surface energetics of each of the post- ring shear samples, the Inverse Gas Chromatography Surface Energy Analyzer (iGC-SEA, Surface Measurement Systems) was employed. Samples were packed into pre-silanized glass columns (30mm length, 3mm I.D) and plugged with Supelco ™ silanized glass wool (Sigma-Aldrich) at both ends. The surface area of powders was determined at 0% RH and 25 ℃ column conditions. Each column underwent a conditioning of 60 minutes prior to the analysis. A full report of the

methods employed for both Specific surface area (SSA) and Surface energy (SE) can be seen in the **Appendix**.

Table 4.5. Description of the parameters employed to perform iGC analyses on all samples.

Parameter	**Set Point**
Mass	80 mg
Solvent for SSA	Octane
Solvents for SE	Heptane, Octane, Nonane, Decane, Dichloromethane, Ethyl acetate, Acetone, Ethanol
Temperature	25 ℃
Carrier gas	Helium

4.3. Statistical methods of analysis

As the sample size for this study was small, normality could not accurately be determined and therefore non-parametric statistical test were conducted. Replicates were only taken for ring shear tester analysis and *in vitro* dissolution, and statistical test were only performed on such as they require a minimum of three replicates per sample. All means and standard deviations were calculated for the replicates; boxplots were plotted for medians and Kruskal-Wallis H-Statistical test was conducted. Finally, spearman correlation was conducted and chosen as it is a non-parametric measure of rank correlation which is appropriate for the small sample size used in this study. All data analysis was conducted by using Python 3 (Appendix D).

5. Results and Discussion

This study was done to determine the effect of particle engineering and addition of an excipient on the processability of pepsin powder. The particle engineering technique employed to produce powder samples was spray drying. It was performed at both a low and high temperature condition for each of the formulations, except the lactose-containing sample which was only produced at high temperature. The temperature condition mainly influenced the particle size; however, other solid-state properties were affected as well. A summary of the spray drying parameters used can be seen in Table 4.2. It is important to note that under the high pH conditions used to dissolve the pepsin powder (pH 12) it is hypothesized that the pepsin was denatured as it often does so at above neutral pH (Campos & Sancho, 2003). However, enzyme properties or activity are not under investigation here and therefore will not be considered.

5.1. Solid-state characterizations

The powder characteristics are presented in Table 5.1. The pycnometric density revealed all samples were approximately 1.59 ± 0.03 g/cm^3. All spray-dried samples were amorphous as seen by the presence of a halo in the diffractogram (Figures 9.5-9.7, Appendix A) compared to the raw pepsin (Figure 9.4, Appendix A) which showed sharp distinct peaks. This coincides with the purpose of using spray drying as a particle engineering method which is often associated with producing amorphous solid dispersions (Klimša et al., 2024). The amorphous nature of the samples is relevant to processability as amorphous materials often exhibit higher surface energy and higher hygroscopicity as compared their crystalline counterparts (Brum & Burnett, 2011). This can lead to increased stickiness and cohesion between particles, which is especially relevant for small particles, where surface phenomena become more dominating than gravity. The analysis by TM-DSC showed different melting point values, with crystalline raw pepsin having the highest at 163.8°C. The melting temperatures for crystalline mannitol (168.49 °C) and lactose monohydrate (148.39 °C) were determined (Figures 9.10, 9.11 in Appendix A). The subsequent analysis of the spray dried samples all revealed glass transitions and no melting points indicating that the samples are all amorphous. Interestingly, two Tg's were noted for one of the mannitol-containing samples (S2.2), which could indicate that the sample is not homogenous causing it to have two separate amorphous phases (Sichina, n.d.).

Excipient-containing samples exhibited decreased Tg values as compared to the non-excipient containing samples, which represent the glass transition of amorphous pepsin (~63 °C). The addition of mannitol lowers the combined Tg to ~ 23°C while the addition of lactose lowers it to 53 °C. Literature reports that amorphous mannitol has a Tg of 13 °C while lactose has a Tg of 110 °C, which explains the lesser drop of Tg in lactose as compared to mannitol (Gabbott et al., n.d.; Kim et al., 1998). Both excipients are acting as plasticizers, lowering the Tg of the sample. The glass transition values are practically relevant as processing at a temperature approaching the Tg can increase the risk of particle collapse and stickiness (Yang et al., 2005).

Table 5.1. Physical characteristics of the six experimental samples.

Sample	Crystallinity	Thermal Events (°C)	Pycnometric density (g/cm^3)	Water content (%)
Raw Pepsin	Crystalline	163.84	1.61	0.60
S1.1: Pepsin, low temp	Amorphous	63.50	1.55	5.20
S1.2: Pepsin high temp	Amorphous	62.41	1.57	7.90
S2.1: Pepsin & Mannitol, low temp	Amorphous	24.20	1.60	3.10
S2.2: Pepsin & Mannitol, high temp	Amorphous	21.57, 57.75	1.60	4.90
S3.2: Pepsin & Lactose, high temp	Amorphous	53.36	1.63	7.60

The Karl-Fisher analysis showed an average water content of 4.89 ± 2.76 %. The samples that underwent harsher drying with higher inlet temperature, outlet temperatures and flow rate (Table 4.2, Materials & Methods) resulted in increased water content. During harsher drying, the increased stickiness of the powder leads to deposition on the cyclone walls, reducing drying efficiency and resulting in higher residual moisture. The higher temperatures might also have induced conformational changes in the protein structure which can cause denaturation, which potentially can also increase stickiness (Haas et al., 2024). The proteins in the samples were probably already denatured due to the increased pH used during dissolving; however, the effect of higher temperature can often cause increased denaturation or aggregation (Akkerman et al., 2016). Zhang et al. explains that spray drying mixtures with high sugar content (S2.1, S2.2, S3.2) can lead to sticking of the powder to the inner cyclone walls, especially in sugars with lower Tg which have increased water content and decreased flow properties (Lechanteur & Evrard, 2020). Typically, the water content of spray-dried samples falls between 2-4%, however, incorporation of increased moisture during the drying process can increase this value further as shown for most samples (Table 5.1) (Osanlóo et al., 2023). A higher water content led to a more heavily plasticized sample where water more easily inserts itself between the protein chain which increases molecular mobility and lowers Tg (M. Mehta et al., 2016).

The DVS curves for all six samples are shown in Figure 5.1. Based on the figure, spray drying increases hygroscopicity of the samples as compared to raw pepsin which is consistent with the amorphous conversion during drying. Amorphous materials have higher free energy and a greater capacity to absorb moisture (Brum & Burnett, 2011). Sample S1.1 with pepsin, S2.2 with pepsin & mannitol standard, and S3.2 with pepsin & lactose standard, showed similar sorption profiles which suggests similar degree hygroscopicity. In the case of the sample with pepsin & mannitol standard (S2.1), the inflection at 40% RH could indicate a recrystallization event where amorphous regions convert to crystalline, releasing water and causing a mass decrease (Müller et al., 2015). Since samples underwent conditioning at 25°C which is slightly above the Tg for this sample, crystallization is probable. The event coincides with the lower

water content (3.1%) and Tg (24.2°C) for that sample indicating it is more plasticized compared to the sample with pepsin & lactose and to pure amorphous pepsin.

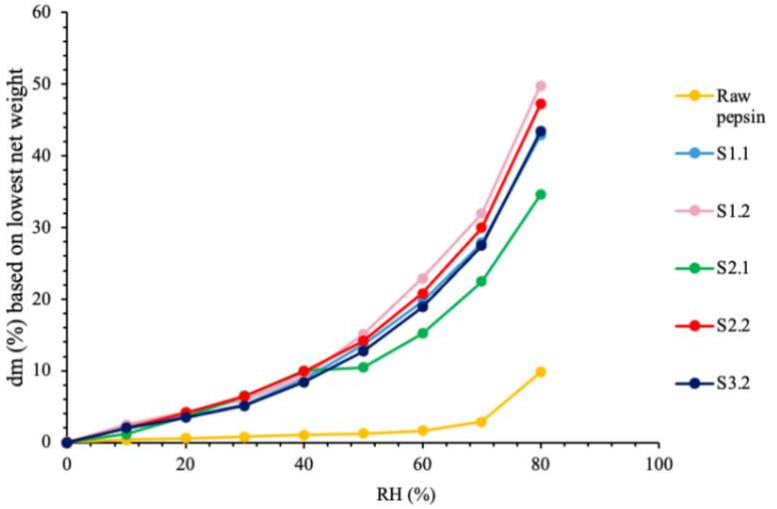

Figure 5.1. Dynamic Vapor Sorption (DVS) curve for all six samples, analyzing the mass change (dm)if the sample between 0-80% relative humidity (RH). All samples were conditioned to reach 0% RH prior to starting sorption analysis

Spray drying had the aim to produce powders with both large and small particle sizes in order to determine the effect that size has on processability. Results (Figure 5.2) showed that while a slight difference is seen between conditions, most spray-dried powder samples had a similar D50%, with an average of 8.43 $\pm$ 2.56 µm. The spray drying conditions used did not produce the clearly distinct size differences that were originally intended. The D90% does differ between samples, with excipient-containing samples being composed of larger particles, indicating a higher degree of agglomeration. This agglomeration may be linked with the higher water content observed in these samples. Despite the similarities in D50, the differences in D90% can still contribute to differences in processability.

A

Sample	Particle size distributions (µm)		
	D10%	D50%	D90%
Raw Pepsin	5.56	37.1	123
S1.1	1.97	4.84	9.66
S1.2	2.73	7.03	15.3
S2.1	3.63	9.60	757
S2.2	4.27	11.5	679
S3.2	3.44	9.16	220

B

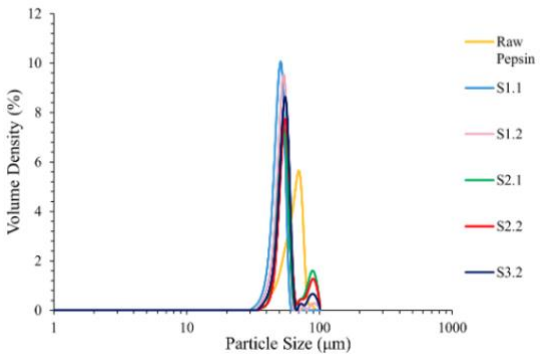

Figure 5.2. a) Table summary b) Particle Size Distribution curves for all six experimental sample

Spray drying produced more spherical particles as seen by comparing raw pepsin imaging versus spray-dried powders (Figure 5.3). Figure 5.3A shows raw pepsin has an angular particle

shape while all other samples (Figure 5.3B-F) have a more spherical shape. The sample with pepsin & mannitol standard (S2.1) showed the most roundness in all powder particles which has previously been seen in formulations containing mannitol (Maas et al., 2011). A slower spray drying leads to more uniform particles and harsher drying is commonly associated with particle wrinkling as seen for samples under the high temperature condition (S1.2, S2.2 and S3.2) (Milanesi et al., 2025). The higher temperatures used for their drying alongside the stickiness seen in the cyclone (Figure 9.1, Appendix) results in more hollow particles which can inflate and shrivel (Milanesi et al., 2025). This wrinkled morphology has been observed in literature with a protein: sugar ratio of 70:30, as exhibited in the present study (Haque et al., 2015). In contrast, the sample containing lactose (S3.2), showed a more spherical and less collapsed morphology with surface creasing, consistent with literature (Wu et al., 2014). This can be attributed to the higher Tg of amorphous lactose as compared to mannitol which could provide greater structural resistance to particle deformation during spray drying (Milanesi et al., 2025).

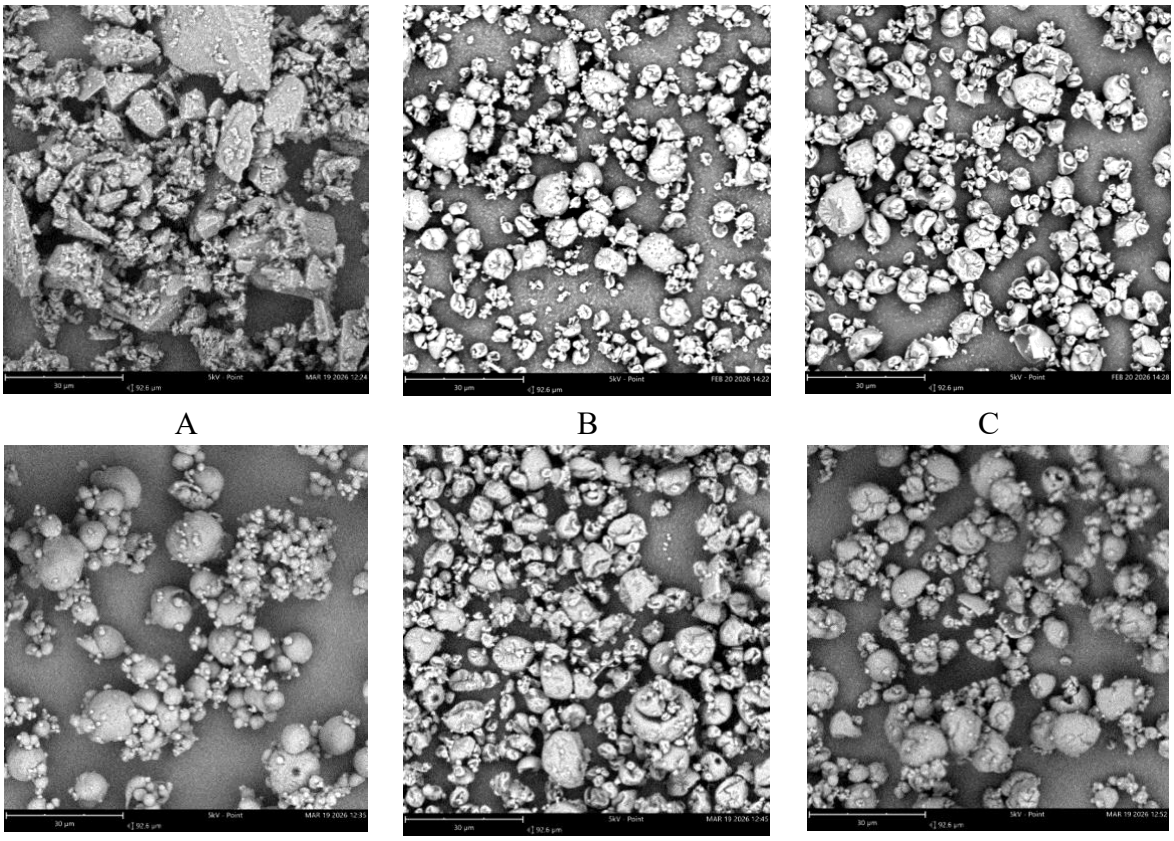

Figure 5.3. Scanning Electron Microscopy imaging for all six experimental samples. a) Raw pepsin, b) S1.1, c) S1.2, d) S2.1, e) S2.2, f) S3.2. The scale bar corresponds to 50 µm. Raw pepsin is crystalline, while all other samples are amorphous, and S1 samples contain only pepsin, S2 samples contain pepsin & mannitol, and S3 sample contains pepsin & lactose.

5.2. Determining the effect on processability

The solid-state properties of each of the powder samples will be used as a basis for understanding processability which was analysed through powder flowability and *in vitro*

dissolution. Flowability is assessed using ring shear testing and bulk and tap density measurement. Dissolution is assessed in PBS (pH 7.4, 15 °C) by using USP Apparatus II to evaluate reconstitution behaviour, essential for parenteral administration. Surface area and surface energetics measured with iGC provide insights into the particle interactions that drive both processability parameters.

5.2.1. Testing flowability

Ring shear tester

Powder flowability was first assessed by performing a stress walk test using a ring shear tester on all six samples. In order to accurately compare all samples, their flow function coefficients (FFC) were interpolated by using a common consolidation stress, 3.606 kPa. Three replicates were analysed for each sample except for sample S2.2 which was only able to be run once on the instrument due to increased powder cohesion during analysis. The FFC was calculating by using Equation 7, where the σ_1 was 3.606 kPa and σ_c was the FC calculated for each sample. The mean of the results (Table 5.2) revealed that the sample with best flow was S2.2 (FFC: 2.25), containing pepsin and mannitol and the worst flow was observed for the lactose-containing sample (FFC: 1.88). A Kruskal-Wallis statistical test (Table 9.3, Appendix C) revealed that by comparing each of the samples' medians, the results obtained were not statistically significant different between the replicates of the six samples (p-value: 0.6234). The overall decreased flowability in all samples might be caused by the potentially denatured pepsin which contains fully exposed side chains which can cause increased cohesion between particles (Shah et al., 2023). Alternatively, given that moisture affects the flowability of powder, the higher water content seen in excipient-containing samples could cause decreased flow due to the plasticization of water (Shah et al., 2023). The higher content of liquid within the samples increases the strength of liquid bridges formed between particles which causes them to stick together through capillary action and hydrogen bonding (Shah et al., 2023). Raw pepsin exhibited one of the lowest FFC values (2.06) which is likely caused by its irregular shape (Figure 5.3) which has been shown to increase friction between particles and cause poor flow (Shah et al., 2023).

Mannitol-containing formulations showed improved flow as compared to those without mannitol or with lactose, as often described in literature (Al-Zoubi et al., 2021). Lactose-containing formulations also often exhibit improved flow, however, the reduced flow for this sample compared to other samples may be attributed to its surface morphology which was creased and less smooth (Figure 5.3) (Al-Zoubi et al., 2021). In general, the smoother the particle the better the flow as spherical particles are able to easily glide over each other, which was exhibited for mannitol-containing samples (Figure 5.3 C and D) (Shah et al., 2023).

Even though the particle size distributions were quite similar, the material spray dried under harsher conditions which also had marginally larger particles did lead to improved flow, comparing S1.1 to S1.2 as well as comparing S2.1 to S2.2 in Table 5.2. Larger particles have a lesser degree of attraction to neighbouring powder particles and therefore when pressure is applied, they experience less interactions (Shah et al., 2023).

Table 5.2. Mean interpolated FFC results at consolidation stress 3.606 kPa for all samples ("(PDF) Bulk Flow Optimisation of Amorphous Solid Dispersion Excipient Powders through Surface Modification," n.d.) .

Sample	FFC (at 3.606 kPa)	Type of Flow
Raw Pepsin	2.06	Cohesive
S1.1	1.94	Very cohesive
S1.2	2.24	Cohesive
S2.1	2.08	Cohesive
S2.2	2.25	Cohesive
S3.2	1.88	Very cohesive

It is important to note that all other analyses performed on the samples, including bulk and tapped density, *in vitro* dissolution, BET surface area and iGC were performed on post-ring shear tester powder samples. These differ slightly in morphology (Figure 5.4) and particle size (Figure 5.5) due to the harsh apparent stress placed on samples during analysis. While the morphologies for raw pepsin, and only-pepsin containing samples remain similar to the original pre-ring shear tester samples (Figure 5.3), the results for samples containing mannitol or lactose monohydrate differed significantly. Mannitol-containing samples appear to be more porous and more highly agglomerated (Figure 5.3D and Figure 5.3E) which explain the difficulty during analysis, specifically for sample S2.2. While the lactose-containing sample showed more spherical particles (Figure 5.3F). The morphological changes post-shear testing highlights the sensitivity of amorphous powder matrices to mechanical stress, particularly for samples containing excipients.

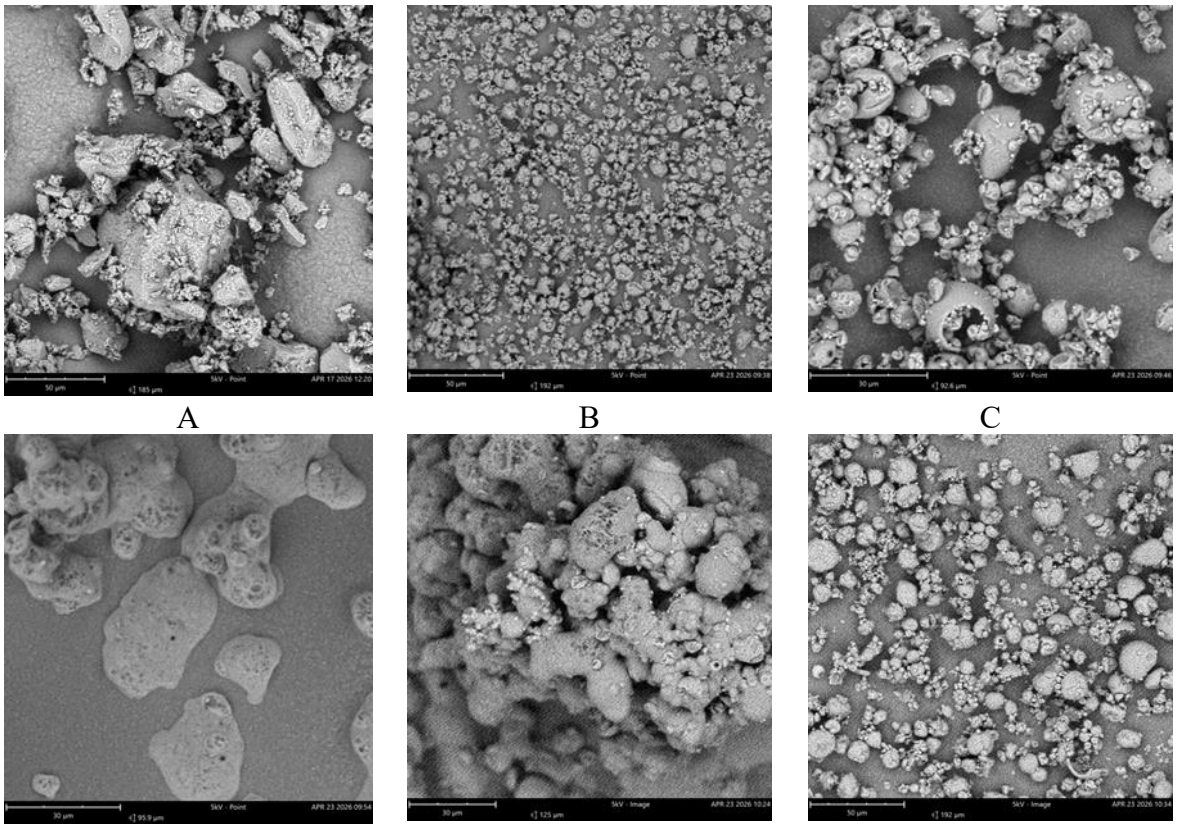

Figure 5.4. Scanning Electron Microscopy imaging for all six experimental samples after ring shear testing. a) Raw pepsin, b) S1.1, c) S1.2, d) S2.1, e) S2.2, f) S3.2. The scale bar corresponds to 50 µm. Raw pepsin is crystalline, while all other samples are amorphous, and S1 samples contain only pepsin, S2 samples contain pepsin & mannitol, and S3 sample contains pepsin & lactose.

A

Sample	Particle size distributions (µm)		
	D10%	D50%	D90%
Raw Pepsin	5.46	36.2	117
S1.1	1.98	4.89	9.86
S1.2	2.87	7.54	302
S2.1	3.80	11.1	1030
S2.2	4.41	11.2	146
S3.2	3.38	8.94	104

B

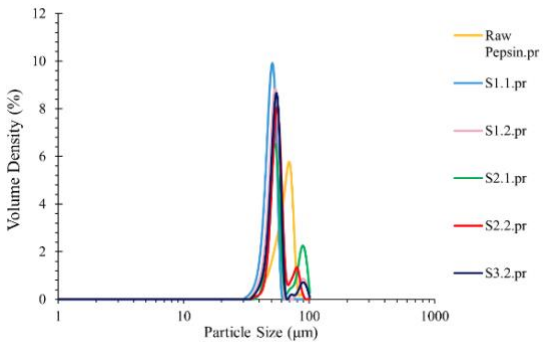

Figure 5.5. a) Table summary b) Particle Size Distribution curves for all six experimental samples after performing ring-shear tester.

Bulk and tapped density

As an additional measure of flowability, the bulk and tap density of all samples post-ring shear tester were determined (Table 9.2, Appendix B). From such, by using Equation 5 and Equation 6 (Section 3.4.2), the Hausner ratio and Compressibility index were calculated to measure the type of flow. The results (Table 5.3) showed that samples with mannitol and lactose had the

most improved flowability. This again, coincides with the statement that larger and more spherical particles show improved flow, both of which apply to the three excipient-containing formulations. When comparing both the ring shear tester and bulk and tap density results, mannitol-containing formulations have the best flow.

Notably, while the ring shear tester classified all samples as either cohesive or very cohesive, bulk and tap measurements suggested passable flow for excipient-containing samples, reflecting the sensitivity of each method to different flow behaviours. It is important to note that bulk and tap measurements can have more bias and variance as the results heavily depend on the method of analysis and can differ between operators (Akseli et al., 2019). It has been found that when a powder mixture is evaluated by using different flowability testers the results often cannot be well correlated, as is for this case (Shah et al., 2023). The ring shear tester applies consolidation stress stimulating conditions during manufacturing like hopper flow in a controlled environment, while bulk and tap density measurements reflect the packing behaviour under gravitational force (Shah et al., 2023). Therefore, the discrepancy between results from both is not a contradiction but rather captures different aspects of powder flowability during manufacturing.

Table 5.3. Flowability properties for all six experimental samples (Powder Flow, 2024).

Sample	Compressibility index (%)	Hausner ratio	Type of flow
Raw Pepsin	30.137	1.431	Poor
S1.1	33.333	1.500	Very poor
S1.2	26.415	1.359	Poor
S2.1	25.532	1.343	Passable
S2.2	23.913	1.314	Passable
S3.2	22.917	1.297	Passable

5.2.2. *in vitro* dissolution study

In vitro dissolution was carried out in PBS pH 7.4 at 15 ℃ using Apparatus II, a rotating paddle, with UV detection. Three replicates of each sample were taken to assess the dissolution for a total of 15 minutes. The different powder samples showed varying behaviour during dissolution tests, however, this is expected give the varying solid-state properties observed. Figure 5.6 shows the average % dissolved profile for the 15-minute dissolution test as well as the data fitted to the Weibull model, as described by Equation 9 (Table 5.4). This model is able to estimate the amount of drug dissolved over time (M) for many different types of dissolution profiles (Dash et al., 2010).

$$M = 1.0 - e\left(\left(-\left(\frac{t}{\lambda}\right) * k\right)\right) \quad (9)$$

In such, t represents time, λ is the time scale of the process and k describes the shape of the dissolution curve, where values below 1 indicate a parabolic profile, values above 1 indicate a sigmoidal profile with an initial lag phase and $k = 1$ represents first-order exponential kinetics

(Dash et al., 2010). The Weibull estimated parameters λ, can then be used, alongside the k parameter, to analyze the dissolution kinetics, which proved to be statistically significant ($p = 0.022$) when comparing all samples against each other (Dash et al., 2010). The root mean square deviation (RMSD) is pictured in Figure 9.36 of Appendix C, which gives information about the deviation of the raw data from the predicted Weibull fit, which shows that S2.1 had the greatest difference in values, caused by the deviation between the models and the data especially between 200 and 400 s. This indicates that the Weibull fit for this sample might not be entirely accurate in capturing the dissolution profile.

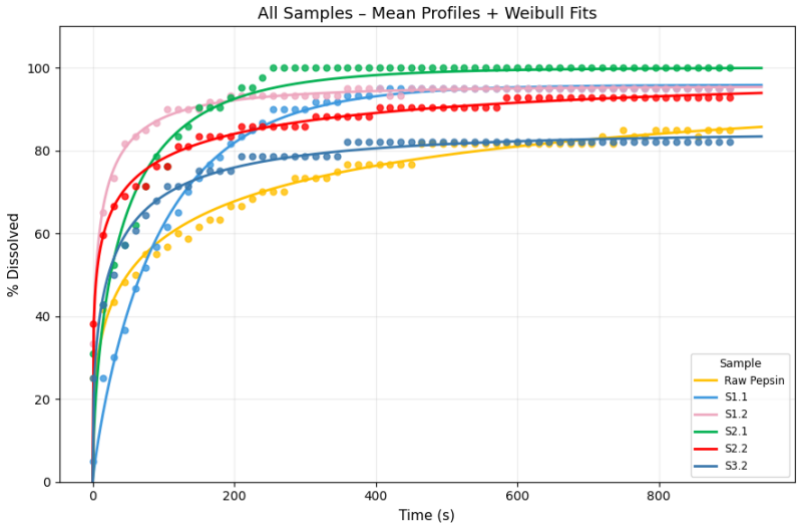

Figure 5.6. Mean in vitro dissolution curve with fitted Weibull models. Raw pepsin is crystalline, while all other samples are amorphous, and S1 samples contain only pepsin, S2 samples contain pepsin & mannitol, and S3 sample contains pepsin & lactose.

In order to accurately capture the dissolution, the t_{25} and t_{50} were determined based on the Weibull equation, representing the time at which 25% or 50% of the powder has dissolved (Table 5.4). Alongside this, a linear regression was fitted to the data for the first 100 seconds of the dissolution curve, and the initial slope was found (Table 5.4). Through performing a Kruskal-Wallis statistical test , all of these dissolution parameters proved to show statistical significance (Table 5.4) except t_{50}, however, due to the small sample size this cannot be concluded with certainty.

The results showed that raw pepsin had the slowest dissolution profile when comparing the λ of all samples, and low initial slope which confirms that in this case spray drying improves dissolution. However, from the t_{25} and t_{50} for this sample, at those timepoints crystalline pepsin dissolves faster than an amorphous pepsin sample (S1.1). But all in all, it is true that amorphous samples have higher solubility and faster dissolution than crystalline samples (Kwon et al., 2020). Interestingly, a sample with only pepsin (S1.1) had $k = 0.88$ exhibiting a near sigmoidal curve which suggests a lag phase before dissolution accelerates.

Samples without excipients (S1.1, S1.2) showed that larger particles dissolved faster than smaller particles (Figure 5.6). This appears counterintuitive based on the Noyes-Whitney equation which predicts faster dissolution with decreasing particle size due to increased surface

area. This can be explained by the morphological differences between non-excipient-containing samples, where S1.1 showed a more irregular and wrinkled particle (Figure 5.4B), while S1.2 (Figure 5.4C) had a rounder and more spherical morphology. Samples with spherical and rougher surfaces have been shown to have a faster dissolution as they expose a higher surface area to the solvent both through the shape and the textures within the particle (Kwon et al., 2020). The wrinkling in S1.1 likely causes tighter packing between particles, which reduces the surface area exposed to the media, hindering wetting. This suggests that in the absence of excipients, particle morphology may be a stronger determinant of dissolution rate than particle size alone for these pepsin samples.

The addition of saccharide excipients showed, in general, enhanced dissolution rate due to their ability to increase the physical and chemical stability, and the surface area of amorphous materials at low storage temperatures, low relative humidity and proper ratios (Vranić, 2004; Wong et al., 2006). While both mannitol-containing samples showed enhanced dissolution compared to non-excipient samples, S2.2 showed faster initial dissolution rate than S2.1, seen by the lower k value (0.72) and shorter t_{25} (0.22 s). This is consistent with the higher porosity and more wrinkled morphology seen in S2.2 (Figure 5.4E) compared to the rounder, smoother particles in S2.1 (Figure 5.4D). For the samples with lactose, they also showed enhanced dissolution as compared to non-excipient samples, but their rate was higher than that for samples with mannitol. In this case, while samples are more spherical than mannitol (Figure 5.4F), they are also less porous and thus underwent slower wetting. This suggests for these samples, more porous and spherical particles lead to faster dissolution. Furthermore, the higher Tg of lactose results in a more rigid amorphous matrix that is less plasticized which can slow the initial wetting, contributing to the slower dissolution rate observed.

Table 5.4. Summary of Weibull fitted samples alongside the different parameters.

Sample	λ^{*}	k	t_{25}(s)**	t_{50}(s)***	Initial Slope (%/s)****	Initial Slope R^2
Raw Pepsin	140.50	0.35	3.96	49.19	0.29	0.83
S1.1	95.48	0.88	24.68	67.66	0.54	0.95
S1.2	9.69	0.40	0.48	4.56	0.50	0.73
S2.1	45.03	0.64	6.37	25.32	0.50	0.98
S2.2	21.52	0.27	0.22	5.59	0.34	0.74
S3.2	28.48	0.43	2.45	22.11	0.44	0.89

* p-value = 0.022

** p-value = 0.016

*** p-value = 0.088

**** p-value = 0.010

5.2.3. Surface Area and Surface Energetics

In order to relate the inter-particle and morphology differences between particles with the flowability and dissolution performance, their surface area and surface energetics were determined. Interestingly all samples showed some level of browning after BET surface area

analysis (Figure 9.18, Appendix B), especially excipient-containing samples. The browning for mannitol-containing samples could be attributed to thermal degradation at the operated temperature (80 °C) or the presence of impurities in the sample. The darker browning specifically for sample S3.2 can be due to a Maillard reaction occurring upon exposure to high temperature during BET analysis which occurs between amino acids and reducing sugars upon heating (El Hosry et al., 2025).

The results from BET surface area analysis showed that samples without excipients (S1.1. S1.2) had the highest surface area as compared to those with excipients, which is contradictory according to literature, where excipients usually increase surface area (Vranić, 2004). Furthermore, the surface area of the mannitol and lactose samples are low compared to what nitrogen adsorption can measure reliably, and therefore the results should be interpreted with caution. The discrepancy can again be likely attributed to morphological differences (Figure 5.4) due to increased agglomeration and cohesion between particles during spray drying, as the presence of excipients with low Tg promotes particle sticking. This reduces the accessible surface area measured by the BET. This is confirmed by the greater agglomeration seen in the D90% values for mannitol-containing samples as compared to the lactose-containing sample (Figure 5.5), discussed earlier (Bonakdar & Ghadiri, 2017).

Table 5.5. BET surface area (m^2/g) results from the BET instrument for all samples. Raw pepsin is crystalline, while all other samples are amorphous, and S1 samples contain only pepsin, S2 samples contain pepsin & mannitol, and S3 sample contains pepsin & lactose.

Sample	BET Surface area (m^2/g)
Raw Pepsin	0.6376
S1.1	1.648
S1.2	1.2312
S2.1	0.3122
S2.2	0.4565
S3.2	0.6575

Inverse gas chromatography (iGC) was used as a complementary technique to determine the surface area and surface energetics of each of the samples. The results showed the same trend to that of BET surface area analysis (Table 5.6), while the specific values differ which is common for organic samples (Almazán-Almazán et al., 2008).

When calculating the surface energy (SE) of the samples, the Dorris-Gray method was employed (as pictured in Figures 9.25 to 9.33 in the Appendix) as it often shows more accurate results (Shi et al., 2011). It is important to note that the absolute value of surface energy cannot be taken for certain as the lower surface area coverages could not calculated for some samples, which led to sampling of only the highest energy surface sites. The trend followed by the SE can however be used to determine which sample has a higher or lower SE value. The surface energy of proteins differs depending on the length of the protein chain, however, the higher apparent surface energy for raw pepsin coincides with that for other crystalline materials

(Hamieh, 2024). Equation 8 (Section 3.4.2) was used to calculate the total surface energy as seen in Table 5.6 below which revealed that excipient-containing samples had a higher total surface energy. This refers to the excess energy present in the surface of the material which makes it strongly attractive to external molecules. The higher total surface energy observed for the samples produced under harsher conditions (S1.2, S2.2, and S3.2) may be related to their morphological characteristics where rougher, more creased surfaces present a greater number of high-energy interactions sites, contributing to increased SE (Williams, 2015).

The surface heterogeneity can also be analysed from the SE data (Figures 9.25-9.27, 9.29, 9.31, 9.33 in the Appendix) show the dispersive surface energy distribution which measures the variation in Van der Waals interaction forces across a surface. Based on these distributions, S2.2 and S3.2 showed the broadest distribution, showing a greater degree of heterogeneity in the samples (Thielmann & Pearse, 2002). Samples without excipient (S1.1 and S1.2) and one of the samples with pepsin & mannitol standard (S2.2) showed a narrower and more homogeneous distribution, suggesting a more uniform SE which is consistent with their more spherical morphologies (Thielmann & Pearse, 2002).

Both mannitol-containing formulations have increased surface energy which can be explained by the increased porosity and roughness in the morphology of those samples as compared to non-excipient containing samples (Han et al., 2019). Non-excipient-containing samples (S1.1, S1.2) also have more round morphology which usually accounts for a lower surface energy (Molleman & Hiemstra, 2018). The high total surface energy of S3.2 (829.14 mJ/m^2) suggests strong inter-particle interactions. The creased morphology of lactose-containing particles likely exposes a higher number of high-energy surface sites, giving rise to stronger cohesive forces between particles. According to literature, lactose usually lowers surface energy due to its ability to smooth particle surfaces, which was not the case for these particles (Jiang et al., 2005).

In order to accurate analyse the surface energy trend for samples with higher surface area measurements and lower total surface energy, or vice versa, an additional variable was added which multiplies the two parameters. By doing such, the grams of sample can be directly correlated to its surface energy, where a higher value represents the surface being more thermodynamically eager to interact with a solvent. The lactose-containing sample still exhibits the highest total surface energetic capacity driven by its high specific and dispersive surface energy components. In contrast, one of the non-excipients containing samples (S1.1), yields the lowest product (253.17 mJ/g), suggesting that its surface is more unreactive towards a solvent.

Table 5.6. Summary of results from iGC, including surface area and surface energetics for all six samples.

Sample	BET Surface Area (m^2/g)	Specific Surface Energy (mJ/m^2)	Dispersive Surface Energy (mJ/m^2)	Total Surface Energy (mJ/m^2)	BET Surface Area × Total SE (mJ/g)
Raw Pepsin	1.1803	237.41	72.12	309.53	365.34
S1.1	1.6476	108.82	44.84	153.66	253.17
S1.2	1.3726	218.14	60.64	278.78	382.65
S2.1	0.9251	230.51	58.77	289.28	267.61
S2.2	1.1032	411.23	87.31	498.54	550.00
S3.2	1.1072	705.67	123.47	829.14	918.02

5.3. Comparison of the effect of powder properties on processability

To more accurately assess the impact of all of the solid-state characteristics, flowability analyses, dissolution performance and surface area and energetics of each of the samples, a spearman correlation matrix was conducted (Figure 5.9). Parameters with $|r|>$ 0.7 are highlighted in the matrix and considered to represent strong correlations. It is important to note that correlation analysis does not include the difference in chemical composition of the materials, surface roughness or whether the sample is amorphous or crystalline and is hence only a partial picture of the complex relationship between the samples. Furthermore, the number of samples are quite limited which increases the possibility of sporous correlations not providing insights to the relationship between the variables.

Water content showed to be a key parameter, with its strongest interaction being with D50% showing a negative correlation (r = -0.77), which confirms the observation that samples with harsher spray drying accumulated more residual moisture, leading to agglomeration and increased size. It also showed a negative correlation with λ (r = -0.71) suggesting that higher water content is associated with faster dissolution. This is further supported by the positive correlation with BET surface area (r = 0.66), where higher water content samples show greater surface area probably due to the more porous and wrinkled morphology. Together these all suggest that for these samples, water content could be seen as a linking parameter between spray drying conditions, particle morphology and dissolution.

From the flowability parameters, the Hausner ratio had the highest r values compares to FFC results, consistent with the observation that the two measures capture different aspects of flow behaviour. The matrix revealed that total surface energy was the strongest predictor of flowability by Hausner ratio, having a negative correlation (r = -0.83). This means that samples with higher SE exhibited poor flow (as pictured in Figure 5.7), which is consistent with the understanding that higher SE promotes stronger inter-particle cohesive forces, increasing resistance to powder movement. Excipient-containing samples also showed a higher degree of heterogeneity, indicating a greater number of high energy interaction sites on their surface

which reduces flowability (Thielmann & Pearse, 2002). This was most evident for the lactose-containing sample having the highest SE and among the poorest flowability results. The figure below (Figure 5.7) shows there is a noticeable trend amongst samples, more specifically for excipient-containing samples between total SE and Hausner ratio. There was also a positive correlation between Hausner ratio and BET surface area from iGC (r = 0.77), also pictured below, suggesting that samples with greater surface area have better flow, however, the trend for such is less clear. The results suggest that packing-related flow behaviour is probably more strongly governed by SE than stress-induced flow.

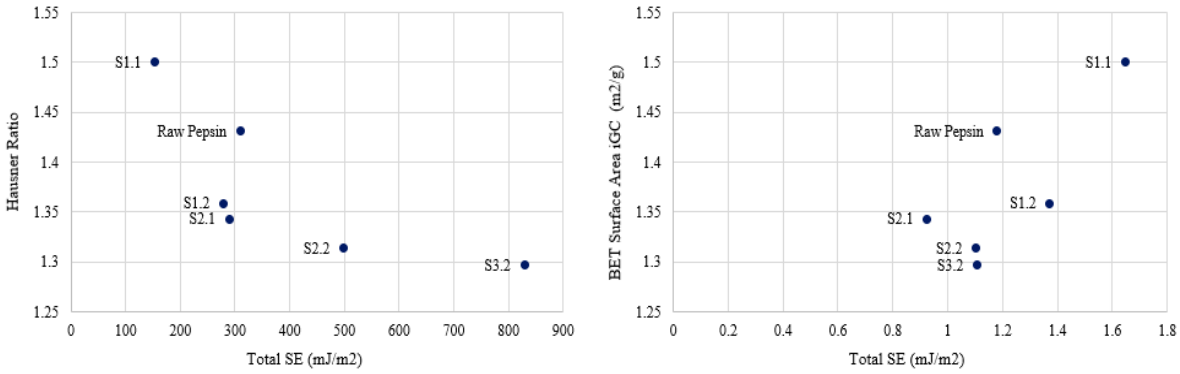

Figure 5.7. Plots for Total Surface Energy (mJ/m^2) versus Hausner ratio and Total Surface Energy (mJ/m^2) versus BET Surface Area (m^2/g) from iGC. Raw pepsin is crystalline, while all other samples are amorphous, and S1 samples contain only pepsin, S2 samples contain pepsin & mannitol, and S3 sample contains pepsin & lactose.

As for dissolution, the strongest correlation was that between initial dissolution rate and D50% (r = -0.90), indicating that larger particle size is associated with slower initial dissolution. This can also be seen pictured below in Figure 5.8 where there is a clear trend in samples. It also proves that crystalline and amorphous samples behave differently in terms of their dissolution profiles, as seen by raw pepsin not fitting the general trend seen by the amorphous samples. This is consistent with the Noyes-Whitney equation; however, the relationship was not as straightforward especially in samples non-excipient containing samples, suggesting that morphology played a role. There was also a strong negative correlation with SE (r = -0.75), suggesting that higher surface energy is associated with slower initial dissolution rate. While this may seem contradictory given that the lactose-containing sample showed fast dissolution and high SE, the correlation is again potentially driven by the morphology of the sample. This, however, cannot be said with certainty due to the small sample size and the fact that there could be other parameters not accounted for.

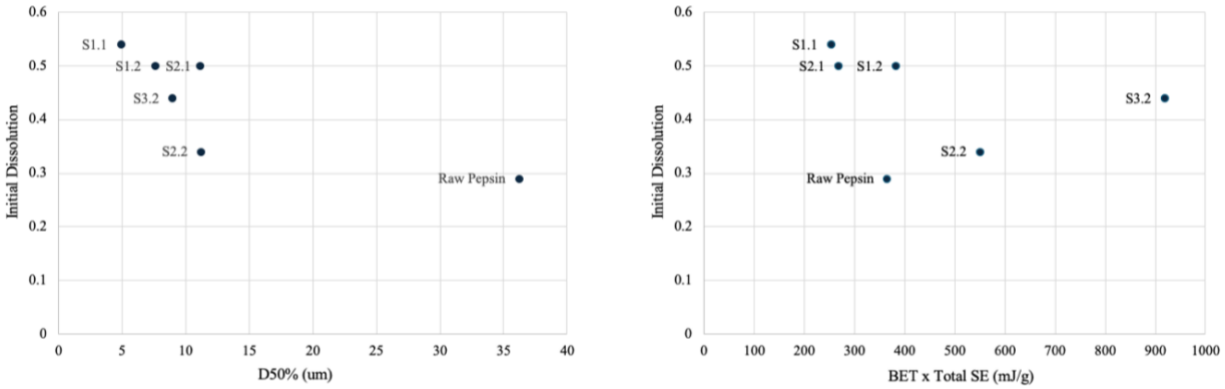

Figure 5.8. Plots for D50% (μm) versus Initial Dissolution and Total Surface Energy (mJ/m^2) versus Initial Dissolution. Raw pepsin is crystalline, while all other samples are amorphous, and S1 samples contain only pepsin, S2 samples contain pepsin & mannitol, and S3 sample contains pepsin & lactose.

Total surface energy showed strong correlations with other parameters aside from flowability by Hausner ratio and dissolution, including the strong positive correlation between total SE and pycnometric density (r = 0.83). This may reflect the influence of adding excipient where adding mannitol and lactose increased the density and altered the SE. The BET surface area × Total SE (mJ/g) parameters show a strong negative correlation with λ (r = -0.83) and t_{25} (r = -0.83), as well as a moderate correlation with t_{50} (r = -0.71). These all indicate that samples with a higher surface energetic capacity tend to dissolve more rapidly. The correlation with initial dissolution rate is weaker, suggesting that while SE governs the overall dissolution, and that early dissolution is captured by t_{25}, it is able to determine the instantaneous rate at which dissolution initiates to a lower degree. This is consistent with both the lactose-containing sample and one of the mannitol-containing samples (S2.2) which both carry high energetic capacity yet differ in their initial slopes, again indicating that other factors such as morphology could be affecting.

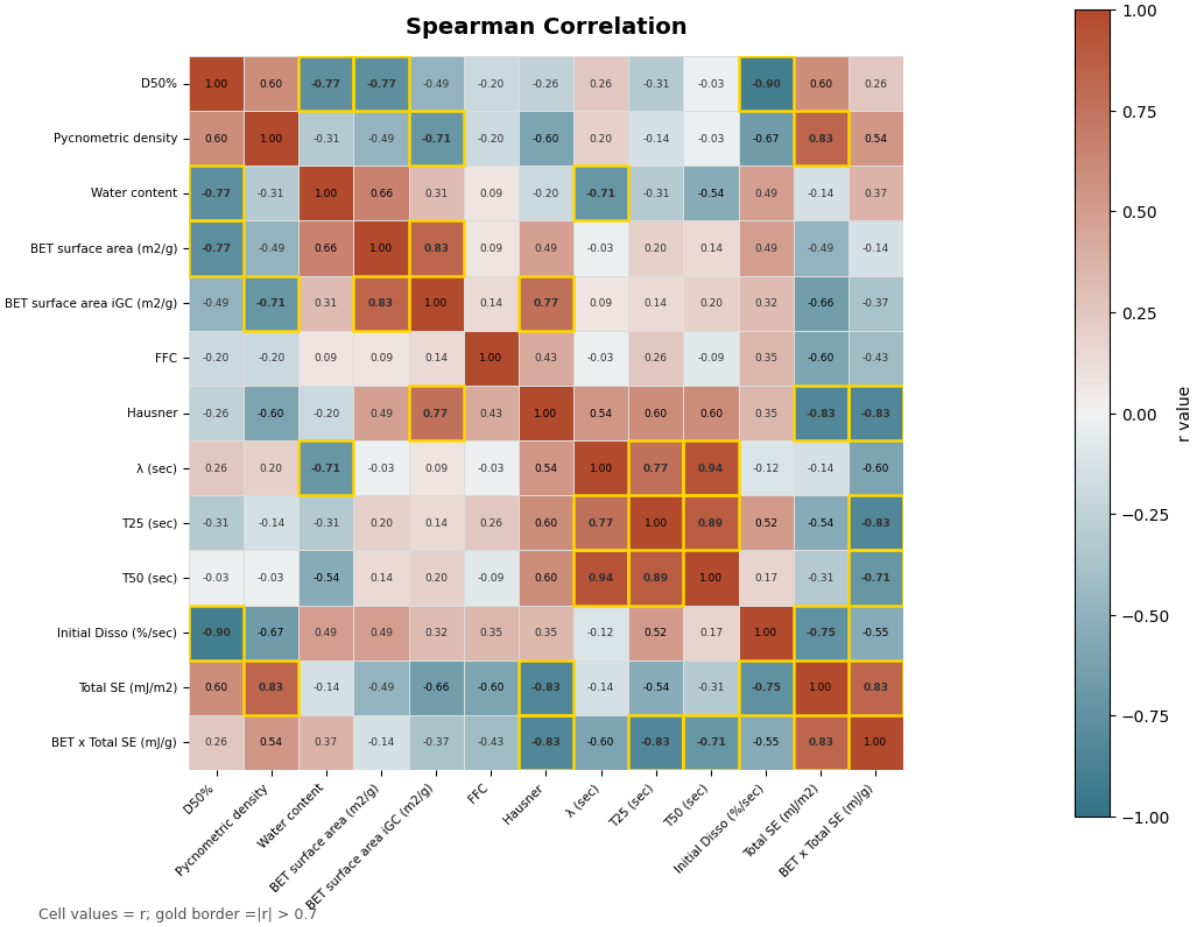

Figure 5.9. Spearman correlation matrix for all data presented previously including, Particle size distribution (D50%), Pycnometric density, Water content, BET surface area, BET surface area from iGC, Flow Function Coefficient (FFC), Hausner ratio, the various dissolution parameters including, λ, t_{25} , t_{50} and Initial Dissolution, and Total surface energy (SE). The legend on the right indicates the strength of correlation where -1 < r < 1.

6. Conclusions

Particle engineering via spray drying and the addition of excipient was shown to significantly influence powder characteristics, which in turn governs the processability of pepsin powder. All spray dried samples were converted into an amorphous form which increased hygroscopicity, surface energy (for samples with mannitol, or lactose under the high temperature condition), and cohesion in comparison to crystalline raw pepsin. These changes had an effect on both the flowability and *in vitro* dissolution behaviour.

All samples exhibited cohesive to very cohesive flow, attributed to the overall small particle size, the potentially denatured state of the pepsin and the increased water content for most samples. Despite this, mannitol-containing formulations showed the best flowability due to their more spherical morphology and smoother particle surface. Lactose-containing samples displayed the poorest flow, due to their creased morphology and highest total surface energy. Surface energy was shown to be the strongest predictor of flowability. For this set of samples, particle morphology proved to be the best determinant of dissolution, with porosity and surface roughness potentially enhancing wetting. Excipient-containing samples showed enhanced dissolution overall, with mannitol formulations dissolving faster. In general, the increased agglomeration seen in excipient-containing samples may have contributed to the elevated SE values, which promoted faster initial dissolution through enhanced wetting, and a suggested increase in particle cohesion and reduced flowability.

Water content was a potential linking parameter connecting the spray drying conditions, particle morphology, agglomeration and processability. Higher residual moisture led to increased agglomeration, reduced flowability and accelerated dissolution through its plasticising effect.

Overall, findings showed that no single parameter governs processability and therefore, optimizing powder for pharmaceutical manufacturing requires an evaluation of spray drying conditions, excipient selection, morphology and surface energetics. Moreover, due to the exploratory nature of this study, further research would have to be conducted to prove and support the conclusions found for this set of samples.

7. Future perspectives

While this study provides valuable insights into the effect of particle engineering on the processability of spray-dried pepsin formulations, the results opened up several avenues for further investigation. From a characterization standpoint, it would be interesting to explore more accurate methods to quantify morphological differences between powder samples. Future studies could implement dynamic image analysis, analysis of SEM images using artificial intelligence, or X-ray computed microtomography, all of which would be able to pinpoint shape and surface differences between samples (van der Haven et al., 2025). To complement this, iGC measurements could be re-taken by considering lower injection probes to accurately assess the samples' surface energy and surface area.

In terms of formulation, future work could investigate a larger set of conditions for each of the already used excipients, or other excipient systems aside from mannitol and lactose monohydrate, such as polymer blends or surfactants, to have a broader understanding of their effect on processability. Furthermore, since pepsin was potentially denatured under the conditions used for this study, it could be beneficial to repeat the study with a model protein that allowed for spray drying under less extreme pH conditions to better investigate the processability outcomes. Regarding the particle engineering method, alternatives to spray drying could be attempted like freeze drying or supercritical fluid-assisted methods which offer better control over particle size, morphology and solid-state characteristics.

From an experimental design perspective, the robustness of the findings could be further strengthened by having a larger number of spray-drying conditions and greater size condition variation. Repeated measurements of each sample would also help strengthen the statistical analyses and allow for assessment of linearity and reproducibility across the data.

8. References

Akkerman, M., Rauh, V. M., Christensen, M., Johansen, L. B., Hammershøj, M., & Larsen, L. B. (2016). Effect of heating strategies on whey protein denaturation—Revisited by liquid chromatography quadrupole time-of-flight mass spectrometry. *Journal of Dairy Science*, *99*(1), 152–166. https://doi.org/10.3168/jds.2015-9924

Akseli, I., Hilden, J., Katz, J. M., Kelly, R. C., Kramer, T. T., Mao, C., Osei-Yeboah, F., & Strong, J. C. (2019). Reproducibility of the Measurement of Bulk/Tapped Density of Pharmaceutical Powders Between Pharmaceutical Laboratories. *Journal of Pharmaceutical Sciences*, *108*(3), 1081–1084. https://doi.org/10.1016/j.xphs.2018.10.009

Almazán-Almazán, M. C., Pérez-Mendoza, M., Fernández-Morales, I., Domingo-García, M., & López-Garzón, F. J. (2008). Use of specific surface areas in inverse gas chromatography studies at zero surface coverage. *Journal of Chromatography A*, *1190*(1), 271–277. https://doi.org/10.1016/j.chroma.2008.02.112

Al-Zoubi, N., Gharaibeh, S., Aljaberi, A., & Nikolakakis, I. (2021). Spray Drying for Direct Compression of Pharmaceuticals. *Processes*, *9*(2), 267. https://doi.org/10.3390/pr9020267

Bałdys, W., Wileńska, M., Bürger, J., Blatkiewicz, M., Piątkowski, M., Sobulska, M., Hashemloo, Z., Kharaghani, A., & Jaskulski, M. (2025). Quantitative analysis of key spray drying variables' impact on maltodextrin powder parameters. *Drying Technology*, *43*(15–16), 2262–2282. https://doi.org/10.1080/07373937.2025.2583332

Bansal, A. K. (2002). *Product Development Issues of Powders for Injection*.

Bhakay, A., Rahman, M., Dave, R. N., & Bilgili, E. (2018). Bioavailability Enhancement of Poorly Water-Soluble Drugs via Nanocomposites: Formulation–Processing Aspects and Challenges. *Pharmaceutics*, *10*(3), 86. https://doi.org/10.3390/pharmaceutics10030086

Bonakdar, T., & Ghadiri, M. (2017). Effect of Structure on Strength of Agglomerates using Distinct Element Method. *EPJ Web of Conferences*, *140*, 15015. https://doi.org/10.1051/epjconf/201714015015

Brum, J., & Burnett, D. (2011). Quantification of Surface Amorphous Content Using Dispersive Surface Energy: The Concept of Effective Amorphous Surface Area. *AAPS PharmSciTech*, *12*(3), 887–892. https://doi.org/10.1208/s12249-011-9655-5

Campos, L. A., & Sancho, J. (2003). The active site of pepsin is formed in the intermediate conformation dominant at mildly acidic pH. *FEBS Letters*, *538*(1–3), 89–95. https://doi.org/10.1016/s0014-5793(03)00152-2

Chan, L. W., & Heng, P. W. S. (2005). Drug Substance and Excipient Characterization. In *Handbook of Pharmaceutical Granulation Technology* (2nd ed.). CRC Press.

Das, S. C., Larson, I., Morton, D. A. V., & Stewart, P. J. (2011). Determination of the Polar and Total Surface Energy Distributions of Particulates by Inverse Gas Chromatography. *Langmuir*, *27*(2), 521–523. https://doi.org/10.1021/la104135z

Dash, S., Murthy, P. N., Nath, L., & Chowdhury, P. (2010). *KINETIC MODELING ON DRUG RELEASE FROM CONTROLLED DRUG DELIVERY SYSTEMS*.

Dedroog, S., Adriaensens, P., & Van den Mooter, G. (2022). Gaining Insight into the Role of the Solvent during Spray Drying of Amorphous Solid Dispersions by Studying

Evaporation Kinetics. *Molecular Pharmaceutics*, *19*(5), 1604–1618. https://doi.org/10.1021/acs.molpharmaceut.2c00095

Drug delivery: The conceptual perspectives and therapeutic applications. (2023). In *Polymer-Drug Conjugates* (pp. 1–38). Academic Press. https://doi.org/10.1016/B978-0-323-91663-9.00010-2

El Hosry, L., Elias, V., Chamoun, V., Halawi, M., Cayot, P., Nehme, A., & Bou-Maroun, E. (2025). Maillard Reaction: Mechanism, Influencing Parameters, Advantages, Disadvantages, and Food Industrial Applications: A Review. *Foods*, *14*(11), 1881. https://doi.org/10.3390/foods14111881

Emami, F., Keihan Shokooh, M., & Mostafavi Yazdi, S. J. (2023). Recent progress in drying technologies for improving the stability and delivery efficiency of biopharmaceuticals. *Journal of Pharmaceutical Investigation*, *53*(1), 35–57. https://doi.org/10.1007/s40005-022-00610-x

Emami, F., Vatanara, A., Park, E. J., & Na, D. H. (2018). Drying Technologies for the Stability and Bioavailability of Biopharmaceuticals. *Pharmaceutics*, *10*(3), 131. https://doi.org/10.3390/pharmaceutics10030131

Forny, L., Marabi, A., & Palzer, S. (2011). Wetting, disintegration and dissolution of agglomerated water soluble powders. *Powder Technology, 9th International Symposium on Agglomeration and 4th International Granulation Workshop, 2009*, *206*(1), 72–78. https://doi.org/10.1016/j.powtec.2010.07.022

Gabbott, P., Clarke, P., Mann, T., Royall, P., & Shergill, S. (n.d.). *A High-Sensitivity, High-Speed DSC Technique: Measurement of Amorphous Lactose*.

Giesche, H. (1998). *Surface Area, Density and Porosity of Powders* (pp. 274–286).

Greene, J. (2021). *Automotive Plastics and Composites*. https://doi.org/10.1016/B978-0-12-818008-2.00009-X

Haas, J., Kim, B. J., Atamer, Z., Wu, C., & Dallas, D. C. (2024). Effects of spray drying and freeze drying on the protein profile of whey protein concentrate. *Journal of Food Science*, *89*(11), 7477–7493. https://doi.org/10.1111/1750-3841.17349

Hamad, M. L., Bowman, K., Smith, N., Sheng, X., & Morris, K. R. (2010). Multi-scale pharmaceutical process understanding: From particle to powder to dosage form. *Chemical Engineering Science, Pharmaceutical Engineering Science- A Key for Tomorrow's Drugs*, *65*(21), 5625–5638. https://doi.org/10.1016/j.ces.2010.01.037

Hamieh, T. (2024). Inverse Gas Chromatography to Characterize the Surface Properties of Solid Materials. *Chemistry of Materials*, *36*(5), 2231–2244. https://doi.org/10.1021/acs.chemmater.3c03091

Han, B., Wang, X., Zheng, J., Liang, S., Xiao, K., Yu, J., Qian, Z., & Huang, X. (2019). Determination of Surface Energy Parameters of Hydrophilic Porous Membranes via a Corrected Contact Angle Approach. *Langmuir*, *35*(47), 15009–15016. https://doi.org/10.1021/acs.langmuir.9b02508

Haque, M. A., Chen, J., Aldred, P., & Adhikari, B. (2015). Drying and denaturation characteristics of whey protein isolate in the presence of lactose and trehalose. *Food Chemistry*, *177*, 8–16. https://doi.org/10.1016/j.foodchem.2014.12.064

He, X., Barone, M. R., Marsac, P. J., & Sperry, D. C. (2008). Development of a rapidly dispersing tablet of a poorly wettable compound—Formulation DOE and mechanistic

study of effect of formulation excipients on wetting of celecoxib. *International Journal of Pharmaceutics*, *353*(1), 176–186. https://doi.org/10.1016/j.ijpharm.2007.11.045

Holm, R. (2024). Parenteral formulations. *European Journal of Pharmaceutical Sciences*, *200*, 106841. https://doi.org/10.1016/j.ejps.2024.106841

Jakubowska, E., & Lulek, J. (2021). The application of freeze-drying as a production method of drug nanocrystals and solid dispersions – A review. *Journal of Drug Delivery Science and Technology*, *62*, 102357. https://doi.org/10.1016/j.jddst.2021.102357

Jiang, R., Zhang, P., Wang, L., Liu, H., Pan, W., & Wang, C. (2005). [Effect of surface modification on surface energy of lactose and performance of dry powder inhalations]. *Yao Xue Xue Bao = Acta Pharmaceutica Sinica*, *40*(4), 373–376.

Karde, V., & Ghoroi, C. (2014). Influence of surface modification on wettability and surface energy characteristics of pharmaceutical excipient powders. *International Journal of Pharmaceutics*, *475*(1), 351–363. https://doi.org/10.1016/j.ijpharm.2014.09.002

Kim, A. I., Akers, M. J., & Nail, S. L. (1998). The physical state of mannitol after freeze-drying: Effects of mannitol concentration, freezing rate, and a noncrystallizing cosolute. *Journal of Pharmaceutical Sciences*, *87*(8), 931–935. https://doi.org/10.1021/js980001d

Klimša, V., Mašková, L., Kašpar, O., Ruphuy, G., & Štěpánek, F. (2024). Rapid screening of ternary amorphous formulations by a spray drying robot. *International Journal of Pharmaceutics*, *651*, 123739. https://doi.org/10.1016/j.ijpharm.2023.123739

Krantz, M., Zhang, H., & Zhu, J. (2009). Characterization of powder flow: Static and dynamic testing. *Powder Technology*, *194*(3), 239–245. https://doi.org/10.1016/j.powtec.2009.05.001

Kwatra, S., Taneja, G., & Nasa, N. (2012). Alternative Routes of Drug Administration-Transdermal, Pulmonary & Parenteral. *Indo Global Journal of Pharmaceutical Sciences*, *02*(04), 409–426. https://doi.org/10.35652/IGJPS.2012.47

Kwon, Y.-B., Kang, J.-H., Han, C.-S., Kim, D.-W., & Park, C.-W. (2020). The Effect of Particle Size and Surface Roughness of Spray-Dried Bosentan Microparticles on Aerodynamic Performance for Dry Powder Inhalation. *Pharmaceutics*, *12*(8), 765. https://doi.org/10.3390/pharmaceutics12080765

Laitinen, R., Lahtinen, J., Silfsten, P., Vartiainen, E., Jarho, P., & Ketolainen, J. (2010). An optical method for continuous monitoring of the dissolution rate of pharmaceutical powders. *Journal of Pharmaceutical and Biomedical Analysis*, *52*(2), 181–189. https://doi.org/10.1016/j.jpba.2010.01.011

Lechanteur, A., & Evrard, B. (2020). Influence of Composition and Spray-Drying Process Parameters on Carrier-Free DPI Properties and Behaviors in the Lung: A review. *Pharmaceutics*, *12*(1), 55. https://doi.org/10.3390/pharmaceutics12010055

Lu, Y., Tang, N., Lian, R., Qi, J., & Wu, W. (2014). Understanding the relationship between wettability and dissolution of solid dispersion. *International Journal of Pharmaceutics*, *465*(1), 25–31. https://doi.org/10.1016/j.ijpharm.2014.02.004

Maas, S. G., Schaldach, G., Littringer, E. M., Mescher, A., Griesser, U. J., Braun, D. E., Walzel, P. E., & Urbanetz, N. A. (2011). The impact of spray drying outlet temperature on the particle morphology of mannitol. *Powder Technology*, *213*(1), 27–35. https://doi.org/10.1016/j.powtec.2011.06.024

Masum, A. K. M., Chandrapala, J., Huppertz, T., Adhikari, B., & Zisu, B. (2020). Influence of drying temperatures and storage parameters on the physicochemical properties of spray-dried infant milk formula powders. *International Dairy Journal*, *105*, 104696. https://doi.org/10.1016/j.idairyj.2020.104696

Mehta, M., Kothari, K., Ragoonanan, V., & Suryanarayanan, R. (2016). Effect of Water on Molecular Mobility and Physical Stability of Amorphous Pharmaceuticals. *Molecular Pharmaceutics*, *13*(4), 1339–1346. https://doi.org/10.1021/acs.molpharmaceut.5b00950

Mehta, T., Najafian, S., Patel, K., Lacombe, J., & Chaudhuri, B. (2025). Optimization of Carrier-Based Dry Powder Inhaler Performance: A Review. *Pharmaceutics*, *17*(1), 96. https://doi.org/10.3390/pharmaceutics17010096

Milanesi, A., Diana, G., Candiani, A., Sodano, A., Rassè, P., Foglio Bonda, A., Bari, E., Torre, M. L., Segale, L., & Giovannelli, L. (2025). Spray drying: From a traditional technology to modern biotechnological applications. *International Journal of Pharmaceutics: X*, *10*, 100449. https://doi.org/10.1016/j.ijpx.2025.100449

Mohammadi-Jam, S., & Waters, K. E. (2014). Inverse gas chromatography applications: A review. *Advances in Colloid and Interface Science*, *212*, 21–44. https://doi.org/10.1016/j.cis.2014.07.002

Molleman, B., & Hiemstra, T. (2018). *Size and shape dependency of surface energy of metallic nanoparticles: Unifying the atomic and thermodynamic approach*.

Montanari, D., Agostini, A., Bonini, M., Corti, G., & Ventisette, C. D. (2017). The Use of Empirical Methods for Testing Granular Materials in Analogue Modelling. *Materials*, *10*(6), 635. https://doi.org/10.3390/ma10060635

Müller, T., Scherließ, R., Schiewe, J., Smal, R., Weiler, C., & Steckel, H. (2015). Applicability of the one-step DVS method for the determination of amorphous amounts for further different hydrophilic and hydrophobic drugs. *European Journal of Pharmaceutics and Biopharmaceutics*, *94*, 333–341. https://doi.org/10.1016/j.ejpb.2015.06.004

Nguyen, H. G. T., Horn, J. C., Bleakney, M., Siderius, D. W., & Espinal, L. (2019). Understanding Material Characteristics through Signature Traits from Helium Pycnometry. *Langmuir*, *35*(6), 2115–2122. https://doi.org/10.1021/acs.langmuir.8b03731

Osanlóo, D. T., Fransson, J., Bergenståhl, B., & Millqvist-Fureby, A. (2023). Effects of drying methods on physical properties and morphology of trehalose/mannitol mixtures. *Drying Technology*, *41*(4), 503–522. https://doi.org/10.1080/07373937.2022.2103564

Particle, Powder, and Compact Characterization. (2017). In *Developing Solid Oral Dosage Forms* (pp. 271–293). Academic Press. https://doi.org/10.1016/B978-0-12-802447-8.00010-8

(PDF) Bulk Flow Optimisation of Amorphous Solid Dispersion Excipient Powders through Surface Modification. (n.d.). *ResearchGate*. https://doi.org/10.3390/pharmaceutics15051447

Pinto, J. T., Faulhammer, E., Dieplinger, J., Dekner, M., Makert, C., Nieder, M., & Paudel, A. (2021). Progress in spray-drying of protein pharmaceuticals: Literature analysis of trends in formulation and process attributes. *Drying Technology*, *39*(11), 1415–1446. https://doi.org/10.1080/07373937.2021.1903032

Powder characterization—Methods, standards, and state of the art. (2021). In *Fundamentals of Laser Powder Bed Fusion of Metals* (pp. 491–527). Elsevier. https://doi.org/10.1016/B978-0-12-824090-8.00006-8

Powder Flow. (2024). USP.

Price, G., & Patel, D. A. (2026). Drug Bioavailability. In *StatPearls*. StatPearls Publishing. http://www.ncbi.nlm.nih.gov/books/NBK557852/

Ragab, D. M., & Rohani, S. (2009). Particle Engineering Strategies via Crystallization for Pulmonary Drug Delivery. *Organic Process Research & Development*, *13*(6), 1215–1223. https://doi.org/10.1021/op900013a

Rajeshwari, R., Divya Dhatri, K., & Mahalaxmi, R. (2020). Hot-melt extrusion technique: A novel continuous manufacturing method for enteric-coated pellets. *Journal of Applied Pharmaceutical Science*. https://doi.org/10.7324/JAPS.2021.110702

Rastegari, A. A., Buzari, B., & Bordbar, A.-K. (2017). Thermal stability of pepsin: A predictive thermodynamic model of a multi-domain protein. *Biochemistry and Biophysics Reports*, *9*, 295–301. https://doi.org/10.1016/j.bbrep.2017.01.005

Saadatkhah, N., Carillo Garcia, A., Ackermann, S., Leclerc, P., Latifi, M., Samih, S., Patience, G. S., & Chaouki, J. (2020). Experimental methods in chemical engineering: Thermogravimetric analysis—TGA. *The Canadian Journal of Chemical Engineering*, *98*(1), 34–43. https://doi.org/10.1002/cjce.23673

Shah, D. S., Moravkar, K. K., Jha, D. K., Lonkar, V., Amin, P. D., & Chalikwar, S. S. (2023). A concise summary of powder processing methodologies for flow enhancement. *Heliyon*, *9*(6), e16498. https://doi.org/10.1016/j.heliyon.2023.e16498

Shanmugam, S. (2015). Granulation techniques and technologies: Recent progresses. *BioImpacts : BI*, *5*(1), 55–63. https://doi.org/10.15171/bi.2015.04

Shi, B., Wang, Y., & Jia, L. (2011). Comparison of Dorris–Gray and Schultz methods for the calculation of surface dispersive free energy by inverse gas chromatography. *Journal of Chromatography A*, *1218*(6), 860–862. https://doi.org/10.1016/j.chroma.2010.12.050

Sichina, W. J. (n.d.). *Measurement of Tg by DSC*.

Solid-State Characterization and Techniques. (2017). In *Developing Solid Oral Dosage Forms* (pp. 59–84). Academic Press. https://doi.org/10.1016/B978-0-12-802447-8.00003-0

Tabernero, A., Martín del Valle, E. M., & Galán, M. A. (2012). Supercritical fluids for pharmaceutical particle engineering: Methods, basic fundamentals and modelling. *Chemical Engineering and Processing: Process Intensification*, *60*, 9–25. https://doi.org/10.1016/j.cep.2012.06.004

Tay, J. Y. S., Liew, C. V., & Heng, P. W. S. (2017). Powder Flow Testing: Judicious Choice of Test Methods. *AAPS PharmSciTech*, *18*(5), 1843–1854. https://doi.org/10.1208/s12249-016-0655-3

Tharanon, W., Guo, Y., Peerapattana, J., & Sun, C. C. (2024). A systematic comparison of four pharmacopoeial methods for measuring powder flowability. *International Journal of Pharmaceutics*, *661*, 124454. https://doi.org/10.1016/j.ijpharm.2024.124454

Thielmann, F., & Pearse, D. (2002). Determination of surface heterogeneity profiles on graphite by finite concentration inverse gas chromatography. *Journal of Chromatography A, First International Conference on Inverse Gas Chromatography*, *969*(1), 323–327. https://doi.org/10.1016/S0021-9673(02)00896-8

Thomas, L. C., Instruments, T., Drive, L., & Castle, N. (n.d.). *Modulated DSC® Paper #2 Modulated DSC® Basics; Calculation and Calibration of MDSC® Signals*.

Tinke, A. P., Govoreanu, R., Weuts, I., Vanhoutte, K., & De Smaele, D. (2009). A review of underlying fundamentals in a wet dispersion size analysis of powders. *Powder Technology*, *196*(2), 102–114. https://doi.org/10.1016/j.powtec.2009.08.005

USP. (2011). *Dissolution*.

USP. (2016). *Injections*. USP.

Valenti, S., Barrio, M., Negrier, P., Romanini, M., Macovez, R., & Tamarit, J.-L. (2021). Comparative Physical Study of Three Pharmaceutically Active Benzodiazepine Derivatives: Crystalline versus Amorphous State and Crystallization Tendency. *Molecular Pharmaceutics*, *18*(4), 1819–1832. https://doi.org/10.1021/acs.molpharmaceut.1c00081

van der Haven, D. L. H., Andreasen, J. L., Zafar, U., Fragkopoulos, I. S., & Elliott, J. A. (2025). Single-particle geometries of pharmaceutical powders from X-ray tomography; a simple and reliable sample preparation method. *Tomography of Materials and Structures*, *8*, 100067. https://doi.org/10.1016/j.tmater.2025.100067

Visser, J. (1989). Van der Waals and other cohesive forces affecting powder fluidization. *Powder Technology*, *58*(1), 1–10. https://doi.org/10.1016/0032-5910(89)80001-4

Vranić, E. (2004). BASIC PRINCIPLES OF DRUG- EXCIPIENTS INTERACTIONS. *Bosnian Journal of Basic Medical Sciences*, *4*(2), 56–58. https://doi.org/10.17305/bjbms.2004.3421

Wahab, W., Alshamsi, R., Alharsousi, B., Alnuaimi, M., Alhammadi, Z., & Al-Zaitone, B. (2025). Recent Developments in Pharmaceutical Spray Drying: Modeling, Process Optimization, and Emerging Trends with Machine Learning. *Pharmaceutics*, *17*(12), 1605. https://doi.org/10.3390/pharmaceutics17121605

Wang, C., Song, S., Gunawardana, C. A., Sun, D. J., & Sun, C. C. (2022). Effects of shear cell size on flowability of powders measured using a ring shear tester. *Powder Technology*, *396*, 555–564. https://doi.org/10.1016/j.powtec.2021.11.015

Wang, Y., Koynov, S., Glasser, B. J., & Muzzio, F. J. (2016). A method to analyze shear cell data of powders measured under different initial consolidation stresses. *Powder Technology*, *294*, 105–112. https://doi.org/10.1016/j.powtec.2016.02.027

Williams, D. R. (2015). Particle Engineering in Pharmaceutical Solids Processing: Surface Energy Considerations. *Current Pharmaceutical Design*, *21*(19), 2677–2694. https://doi.org/10.2174/1381612821666150416100319

Wong, S. M., Kellaway, I. W., & Murdan, S. (2006). Enhancement of the dissolution rate and oral absorption of a poorly water soluble drug by formation of surfactant-containing microparticles. *International Journal of Pharmaceutics*, *317*(1), 61–68. https://doi.org/10.1016/j.ijpharm.2006.03.001

Wu, L., Miao, X., Shan, Z., Huang, Y., Li, L., Pan, X., Yao, Q., Li, G., & Wu, C. (2014). Studies on the spray dried lactose as carrier for dry powder inhalation. *Asian Journal of Pharmaceutical Sciences*, *9*(6), 336–341. https://doi.org/10.1016/j.ajps.2014.07.006

Yang, B., Min Huang, W., Li, C., & Hoe Chor, J. (2005). Effects of moisture on the glass transition temperature of polyurethane shape memory polymer filled with nano-carbon

powder. *European Polymer Journal*, *41*(5), 1123–1128. https://doi.org/10.1016/j.eurpolymj.2004.11.029

Zhang, Y., Williams III, R. O., & Tucker, H. O. (2020). Formulation strategies in immunotherapeutic pharmaceutical products. *World Journal of Clinical Oncology*, *11*(5), 275–282. https://doi.org/10.5306/wjco.v11.i5.275

Ziaee, A., Albadarin, A. B., Padrela, L., Ung, M.-T., Femmer, T., Walker, G., & O'Reilly, E. (2020). A rational approach towards spray drying of biopharmaceuticals: The case of lysozyme. *Powder Technology*, *366*, 206–215. https://doi.org/10.1016/j.powtec.2020.02.057

9. Appendices

Figure 9.1. Illustration of the harsh spray drying process used for samples S1.2, S2.2 and S3.2. Significant deposition of powder on the cyclone walls can be seen.

Appendix A: Solid-state characterizations

X-ray Powder Diffraction (XRPD)

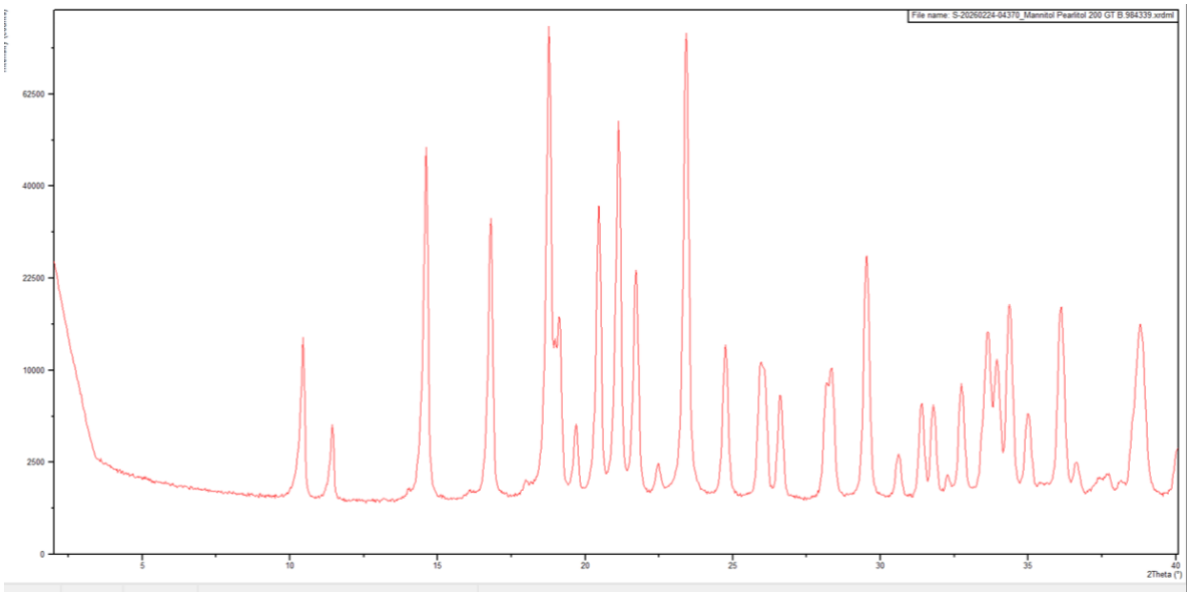

Figure 9.2. XRPD image of mannitol.

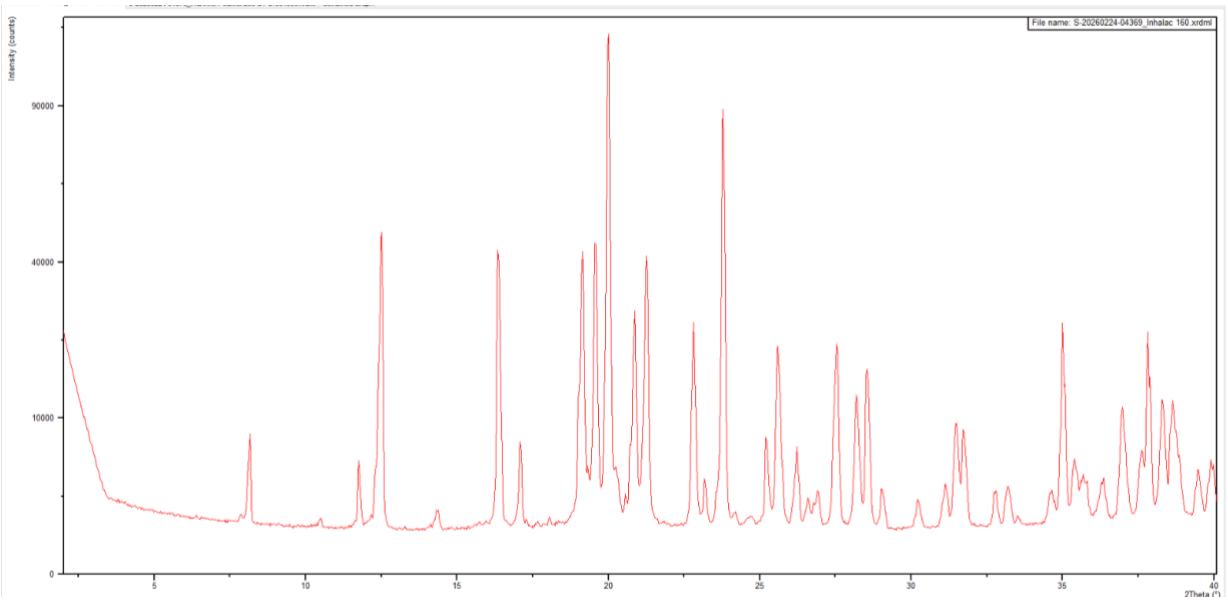

Figure 9.3. XRPD image of lactose monohydrate.

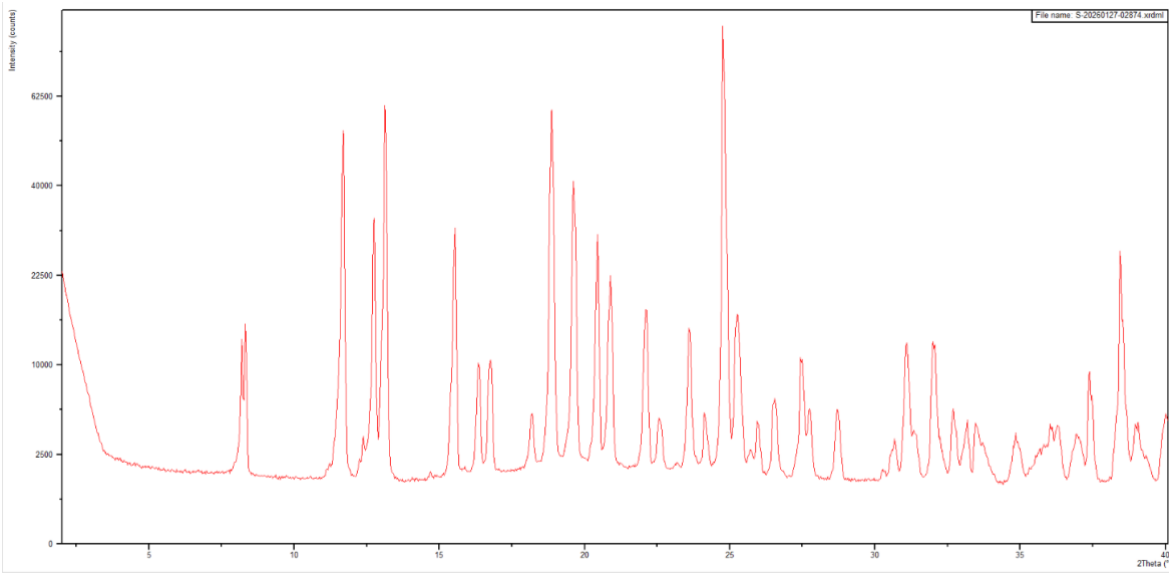

Figure 9.4. XRPD image of raw pepsin.

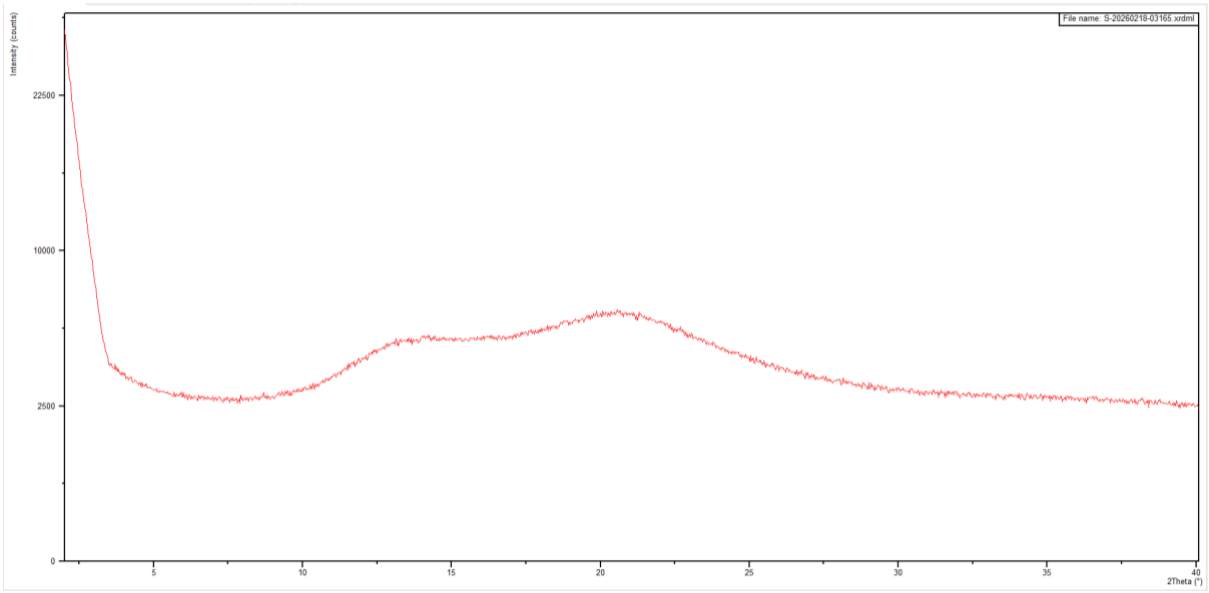

Figure 9.5. XRPD image of sample S1.1 containing pepsin under the standard, lower temperature spray drying conditions.

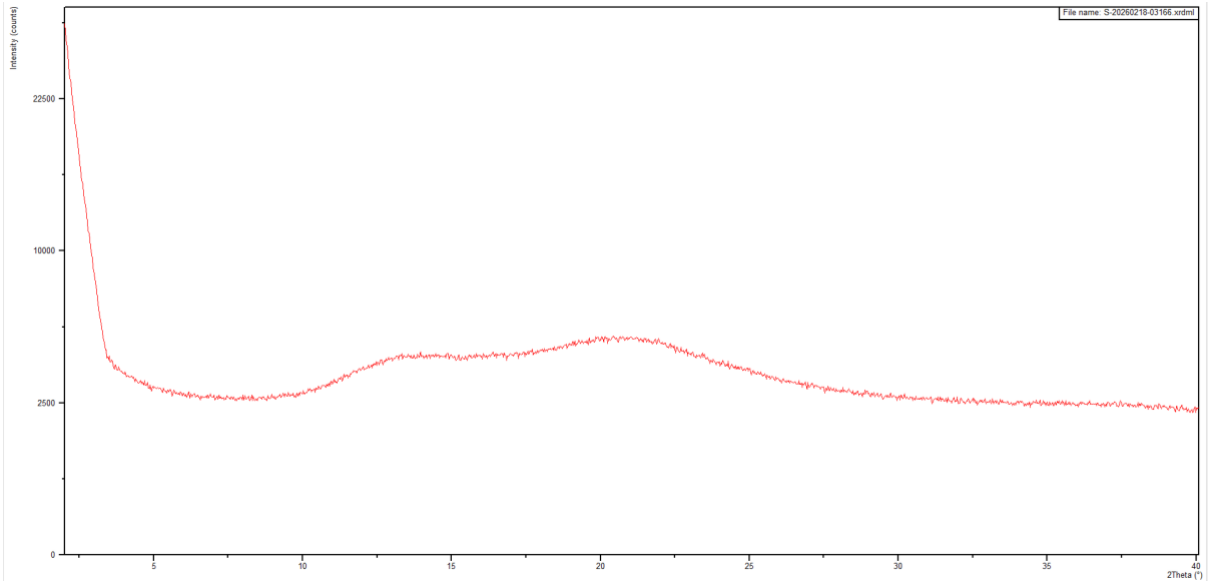

Figure 9.6. XRPD image of sample S1.2 containing pepsin under the high temperature spray drying conditions.

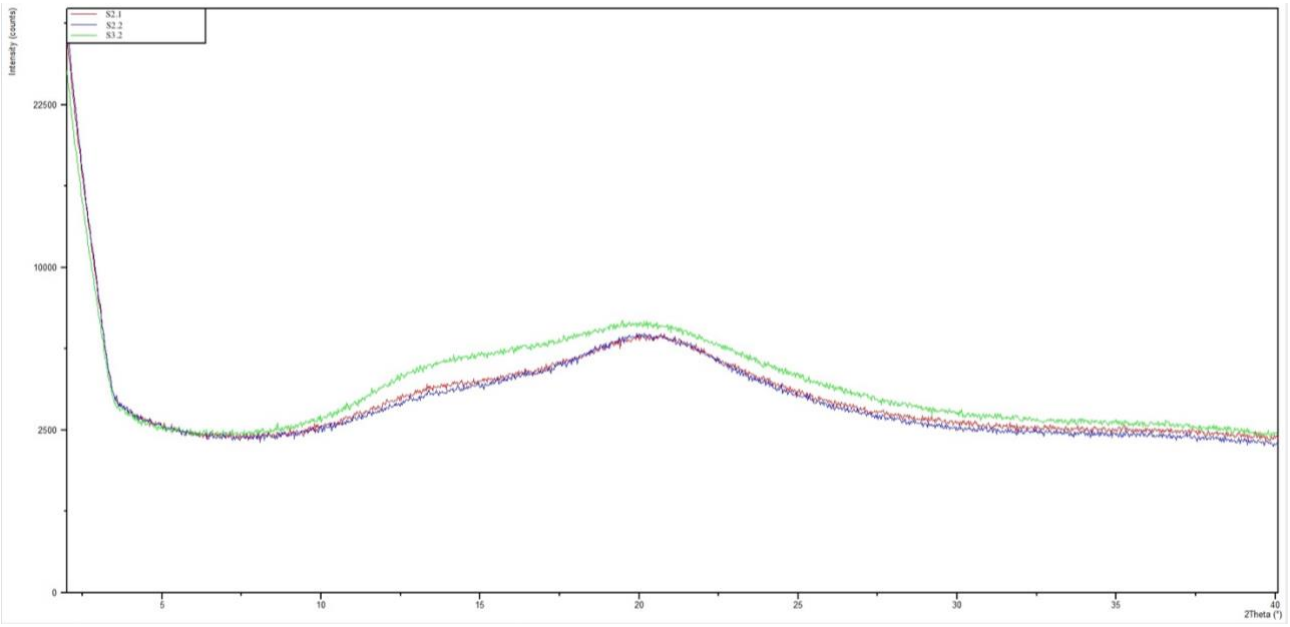

Figure 9.7. XRPD image of all excipient-containing samples S2.1 (red), S2.2 (blue) and S3.2 (green) in that order.

Thermo-gravimetric Analysis (TGA)

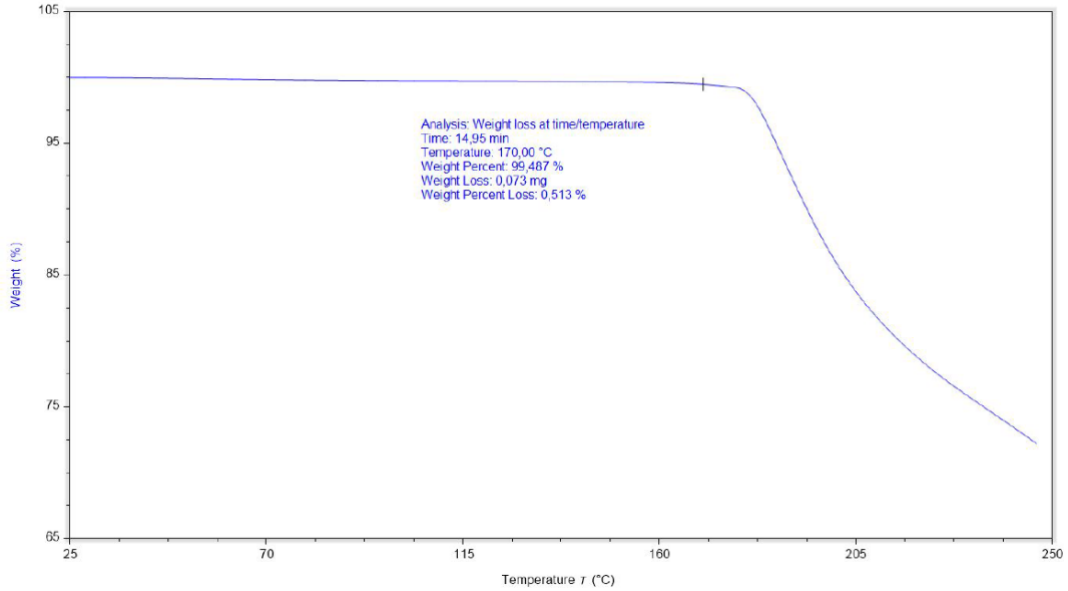

Figure 9.8. TGA analysis of raw pepsin

Differential Scanning Calorimetry (DSC)

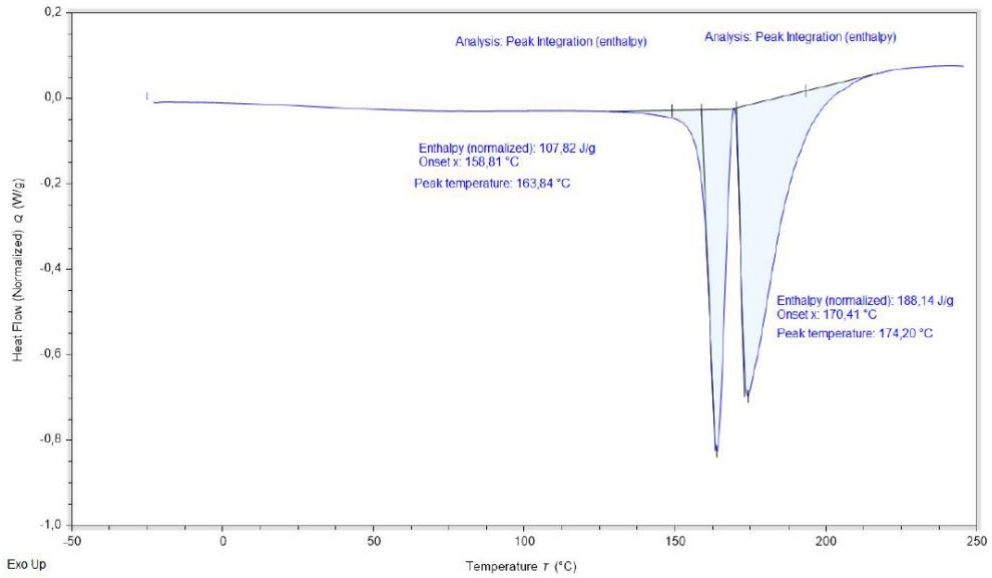

Figure 9.9. TM- DSC of raw pepsin.

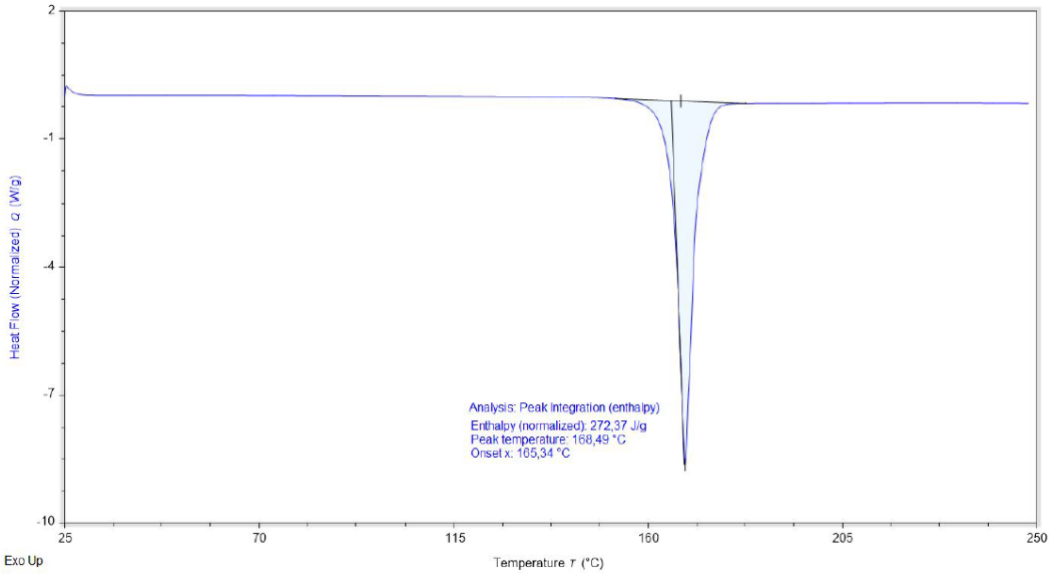

Figure 9.10. TM- DSC of Mannitol Pearlitol 200 GB.

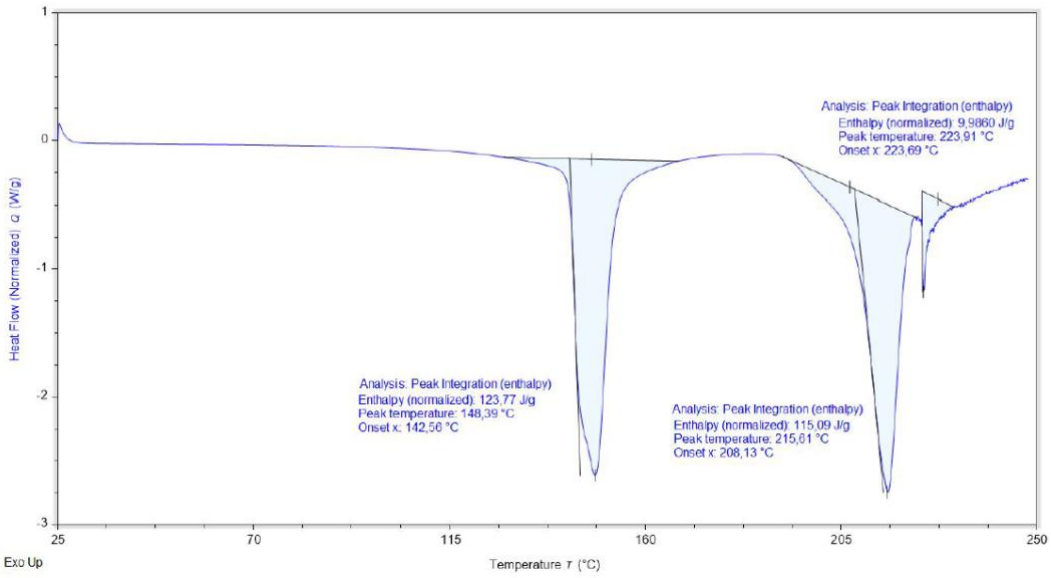

Figure 9.11. TM- DSC of Lactose monohydrate Inhalac 160.

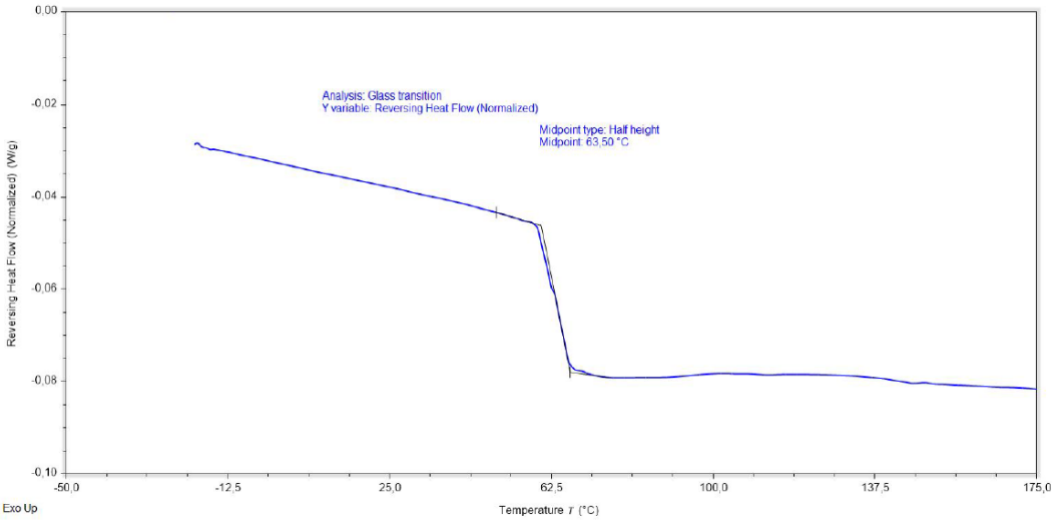

Figure 9.12. TM- DSC of S1.1.

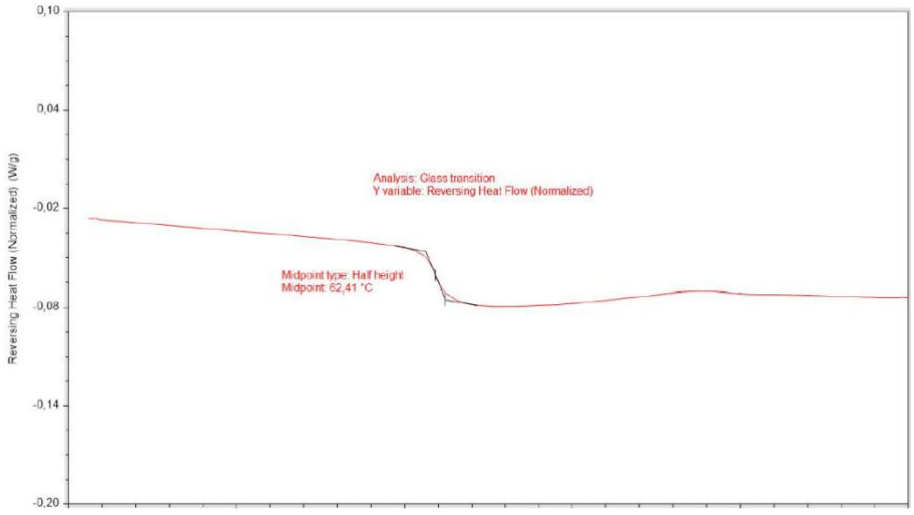

Figure 9.13. TM- DSC of S1.2.

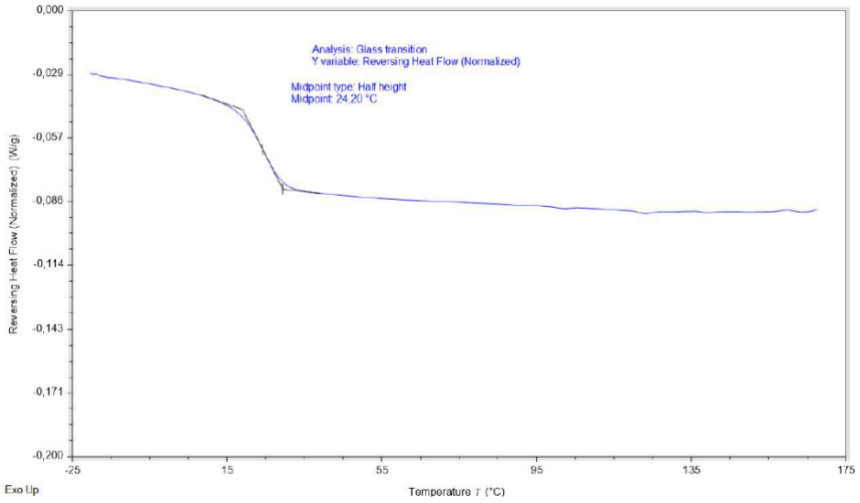

Figure 9.14. TM- DSC of S2.1.

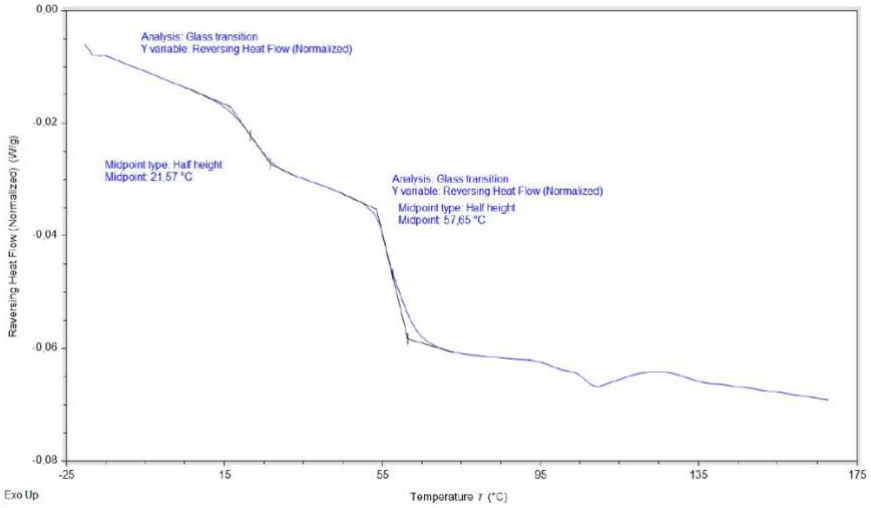

Figure 9.15. TM- DSC of S2.2.

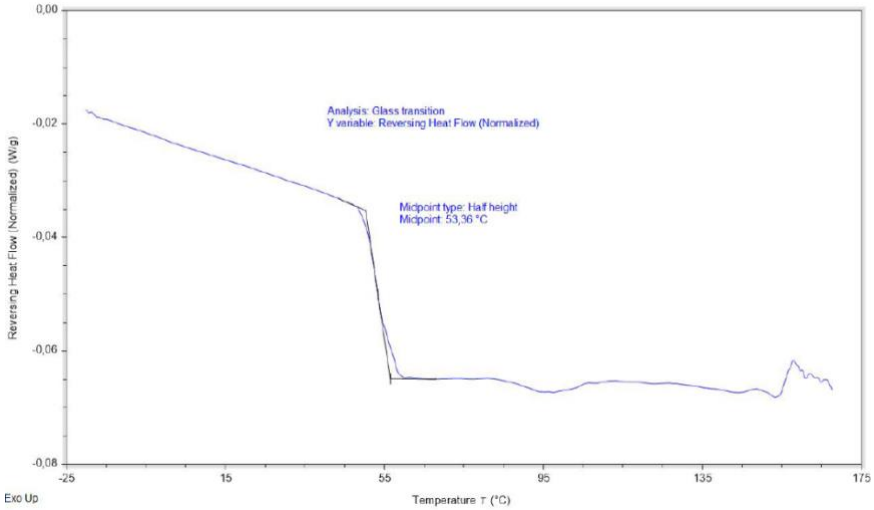

Figure 9.16. TM- DSC of S3.2.

Appendix B: Processability parameters

Ring Shear Tester

Table 9.1. Raw Ring Shear Tester data for all six samples with three replicates, except for sample S2.2 which only had one replicate.
("Solid-State Characterization and Techniques," 2017)

Sample	SIGMA1 [kF	FC [kPa]	SIGMA1 [Pa	FC [Pa]	FFC	FFRHO	TAU,C [Pa]	RHOB [kg/m	PHIE [°]	PHILIN [°]	PHISF [°]
Raw Pepsin	1.546	0.957	1546	957	1.62	1.08	276	669	50.8	30.1	40.9
	2.551	1.343	2551	1343	1.9	1.33	380	699	47.5	31.1	39.9
	4.023	1.8	4023	1800	2.24	1.63	500	728	45.1	31.8	39
S1.1	1.559	1.011	1559	1011	1.54	0.74	296	479	51.7	29.2	41.5
	2.52	1.423	2520	1423	1.77	0.89	437	501	45.9	26.9	39.2
	3.935	1.872	3935	1872	2.1	1.1	551	525	43.9	29.1	38.1
S1.2	1.528	0.846	1528	846	1.8	0.88	246	489	47.6	29.7	39.9
	2.661	1.252	2661	1252	2.12	1.09	352	514	45.5	31.3	40.2
	4.248	1.792	4248	1792	2.37	1.27	502	537	43.8	31.5	39.6
S2.1	1.427	0.775	1427	775	1.84	0.69	211	377	49.6	32.9	38.9
	2.264	1.118	2264	1118	2.03	0.77	305	383	47.5	32.7	37.3
	3.581	1.662	3581	1662	2.16	0.84	447	389	47	33.4	36.9
S2.2	3.606	2.247	3606	2247	1.6	0.51	510	319	58.8	41.1	50.3
S3.2	1.734	1.067	1734	1067	1.62	0.68	282	421	53.7	34.2	44.4
	2.971	1.654	2971	1654	1.8	0.79	421	440	52.6	36	44.8
	4.699	2.393	4699	2393	1.96	0.9	621	460	50	35.1	43.8

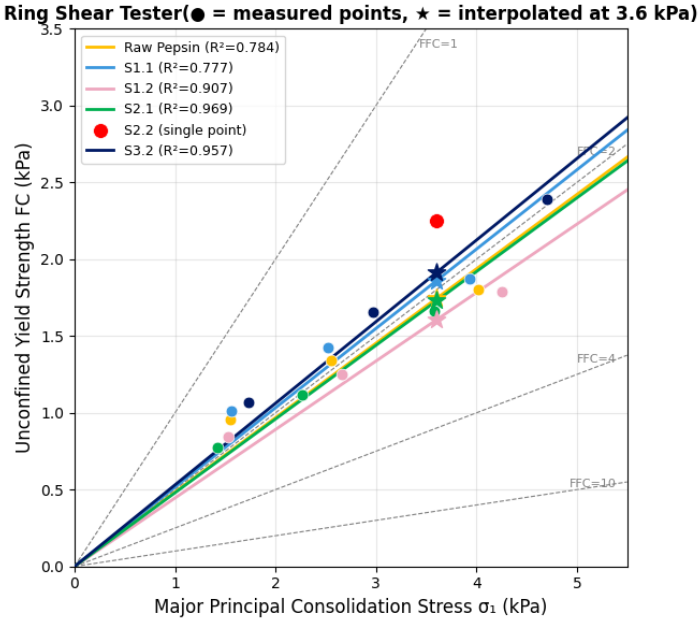

Figure 9.17. Ring shear tester graph showing both raw data points for each sample, shown with dots, and the interpolated FC (kPa), shown with stars.

Bulk and Tapped Density

Table 9.2. Bulk and tapped density characteristics for all six experimental samples.

Sample	Bulk density (g/cm^3)	Tap density (g/cm^3)
Raw Pepsin	0.51	0.73
S1.1	0.34	0.51
S1.2	0.39	0.53
S2.1	0.35	0.47
S2.2	0.35	0.46
S3.2	0.37	0.48

BET Surface Area

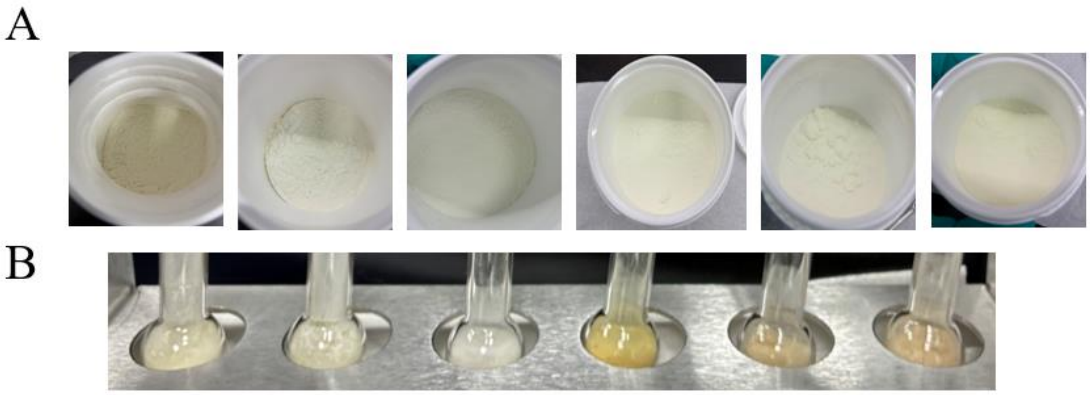

Figure 9.18. A) Samples prior to BET surface area analysis, B) Samples after BET surface area analysis. The order of the samples from left to right is; Raw pepsin, S1.1, S1.2, S2.1, S2.2, S3.2.

Inverse Gas Chromatography (iGC)

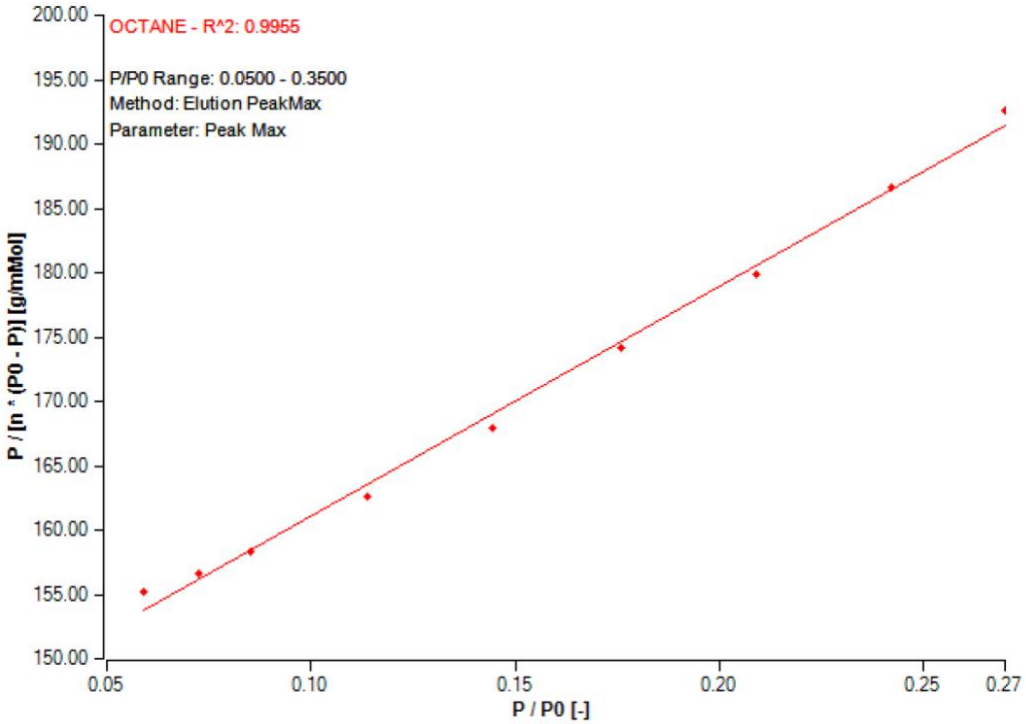

Figure 9.19. BET SSA curve for raw pepsin

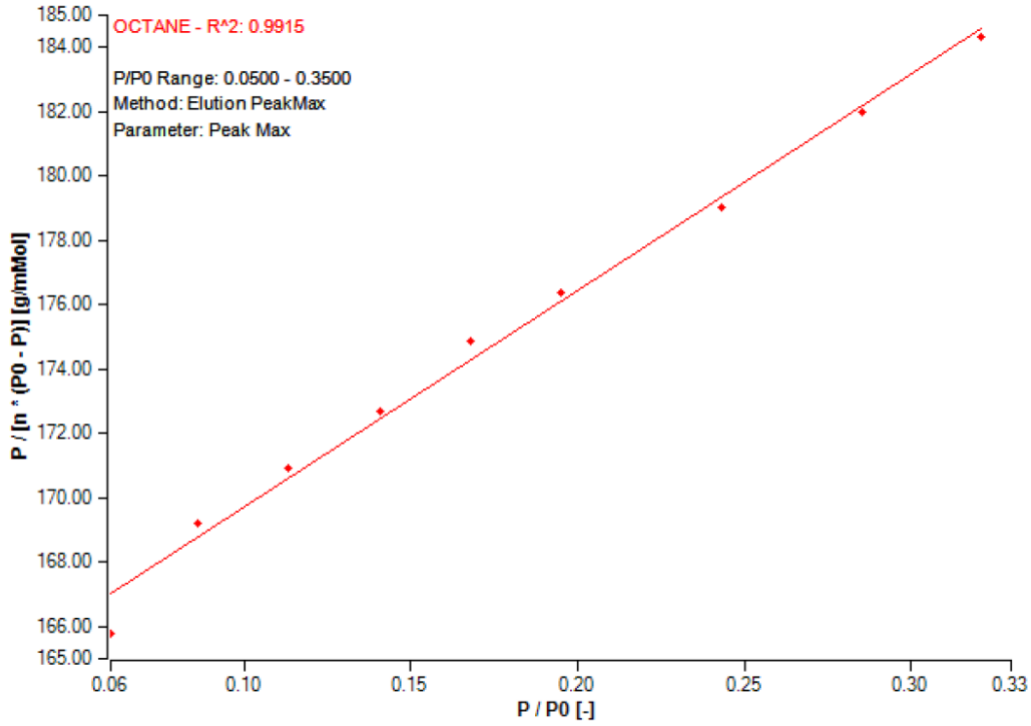

Figure 9.20. BET SSA curve for S1.1

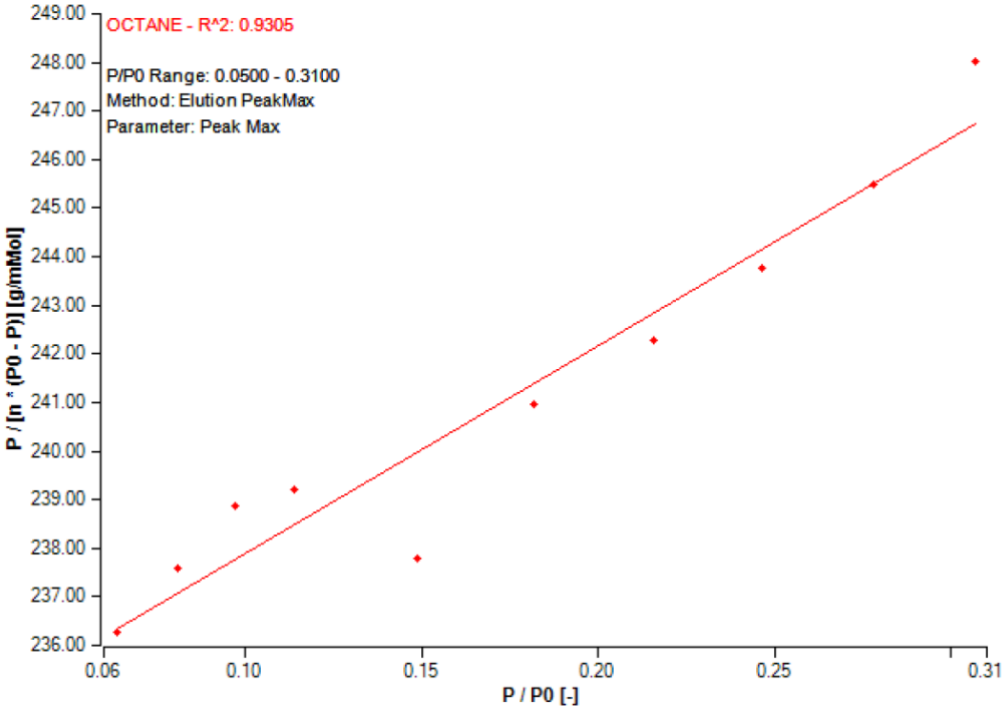

Figure 9.21. BET SSA curve for S1.2

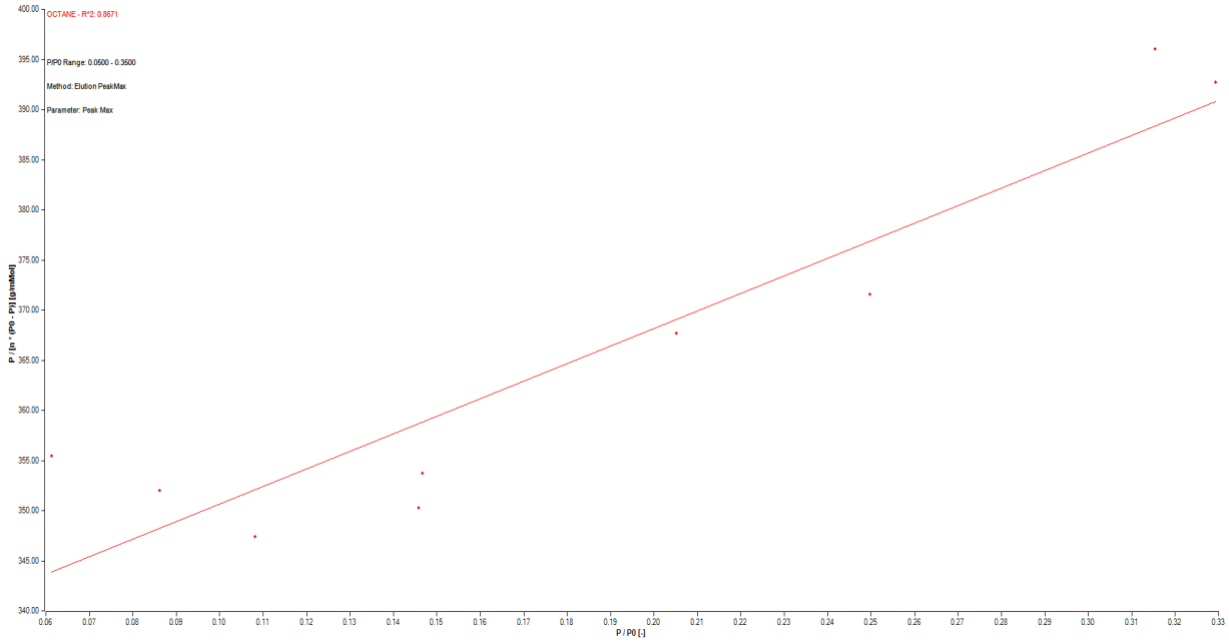

Figure 9.22. BET SSA curve for S2.1

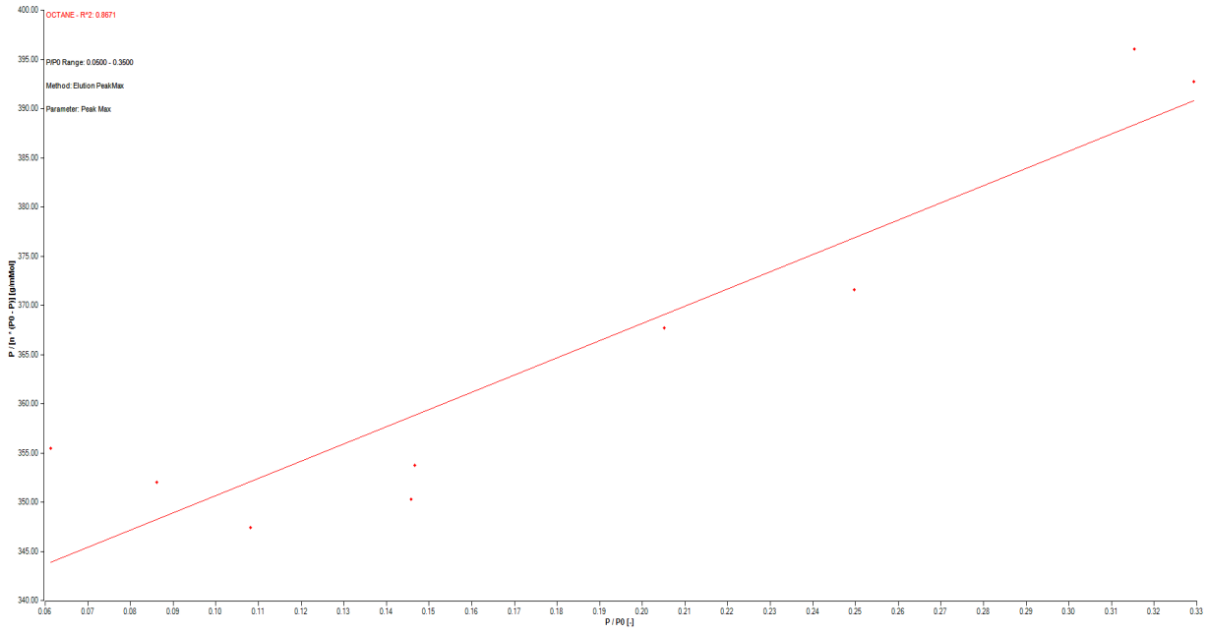

Figure 9.23. BET SSA curve for S2.2

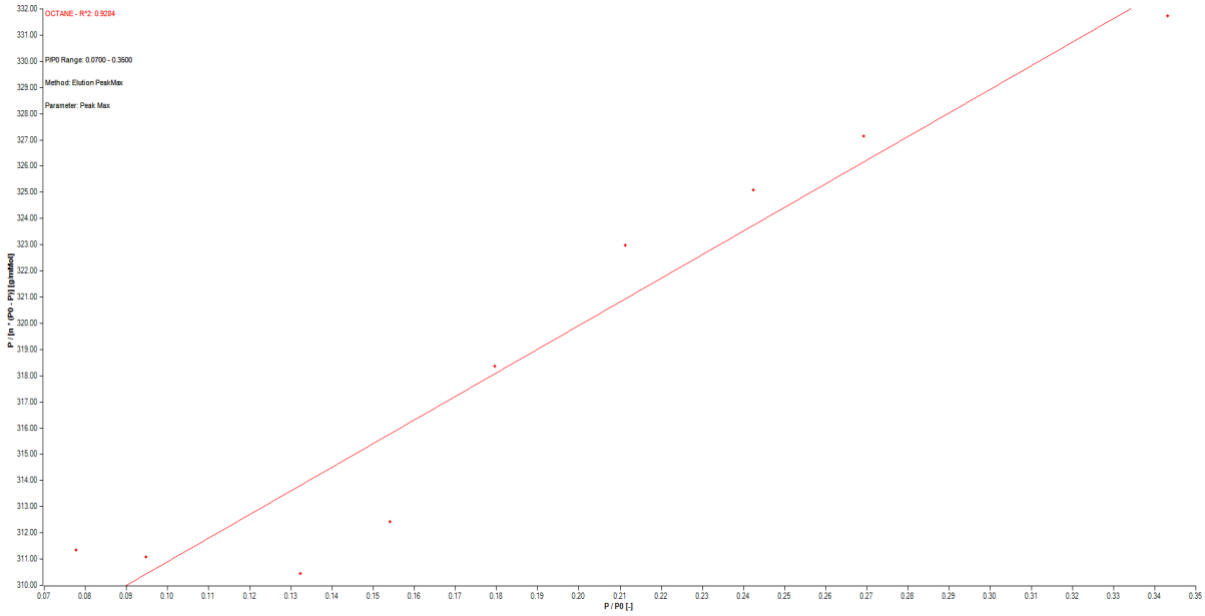

Figure 9.24. BET SSA curve for S3.2

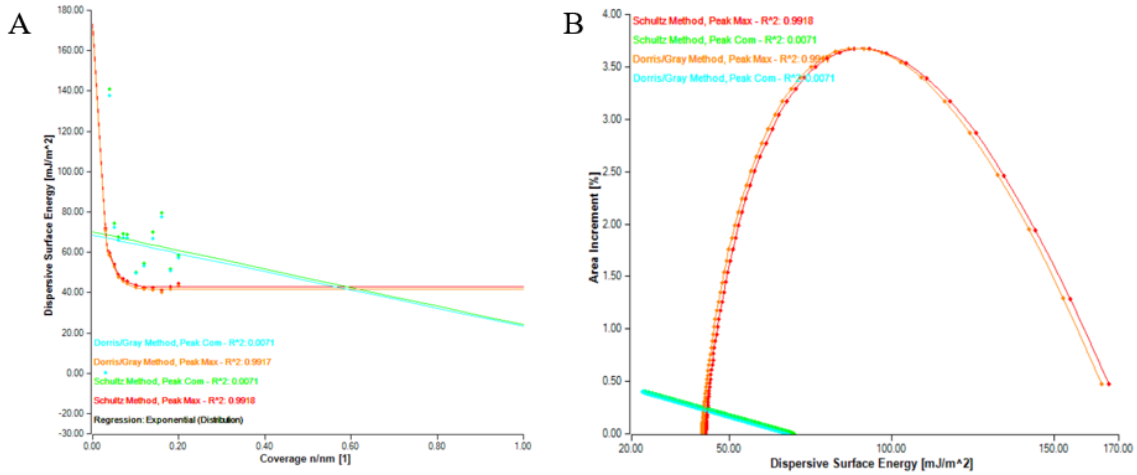

Figure 9.25. SE analysis for raw pepsin a) dispersive surface energy b) dispersive surface energy distribution

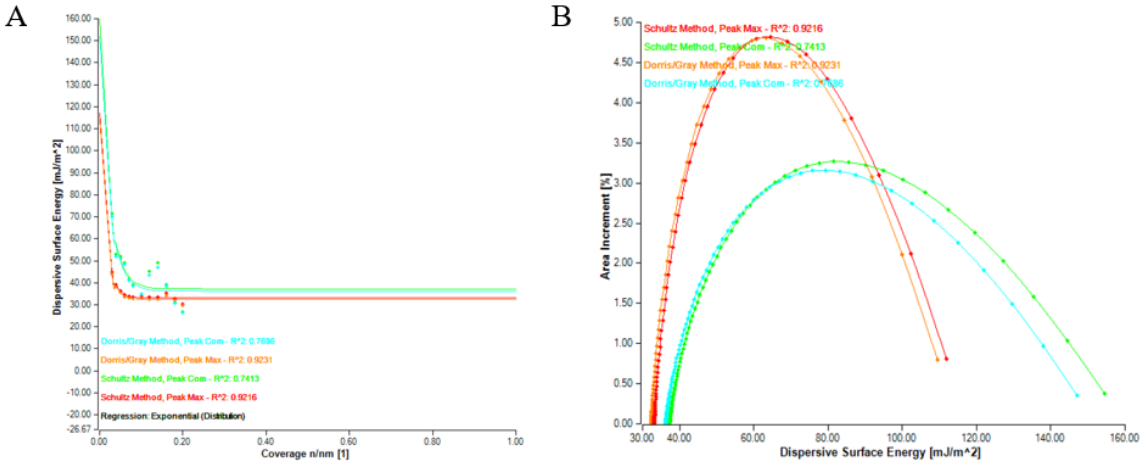

Figure 9.26. SE analysis for S1.1 a) dispersive surface energy b) dispersive surface energy distribution

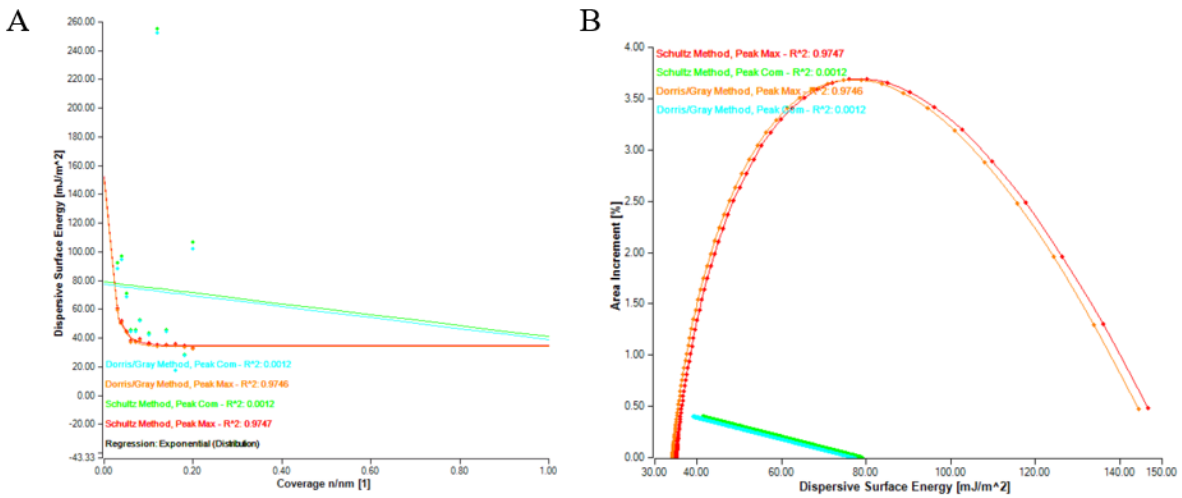

Figure 9.27. SE analysis for S1.2 a) dispersive surface energy b) dispersive surface energy distribution

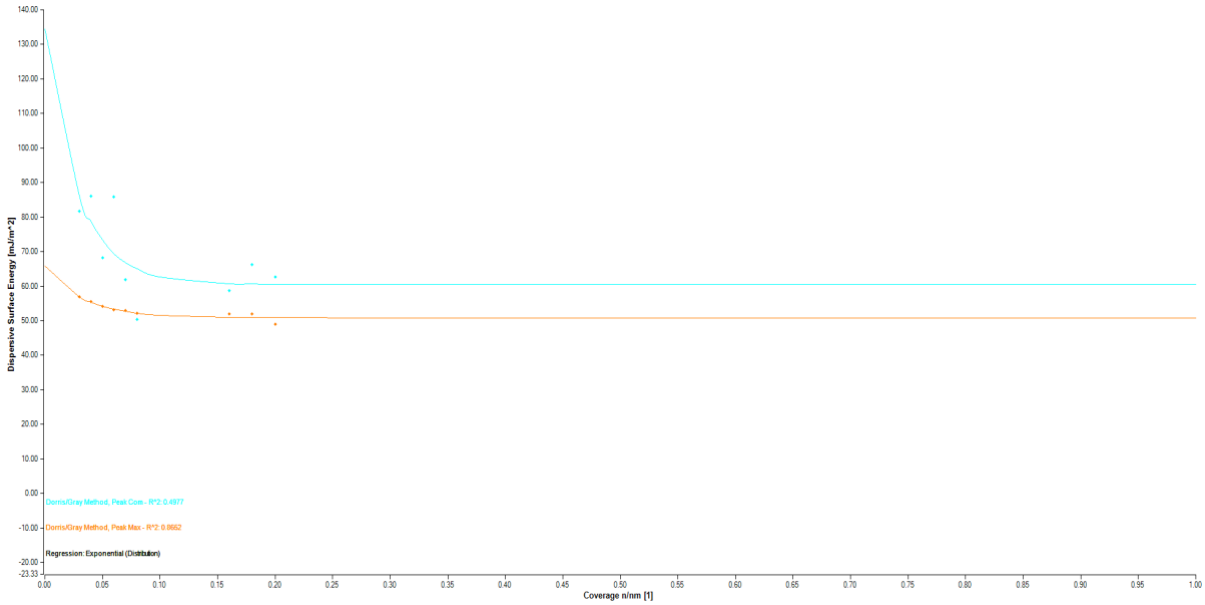

Figure 9.28. SE analysis for S2.1, dispersive surface energy

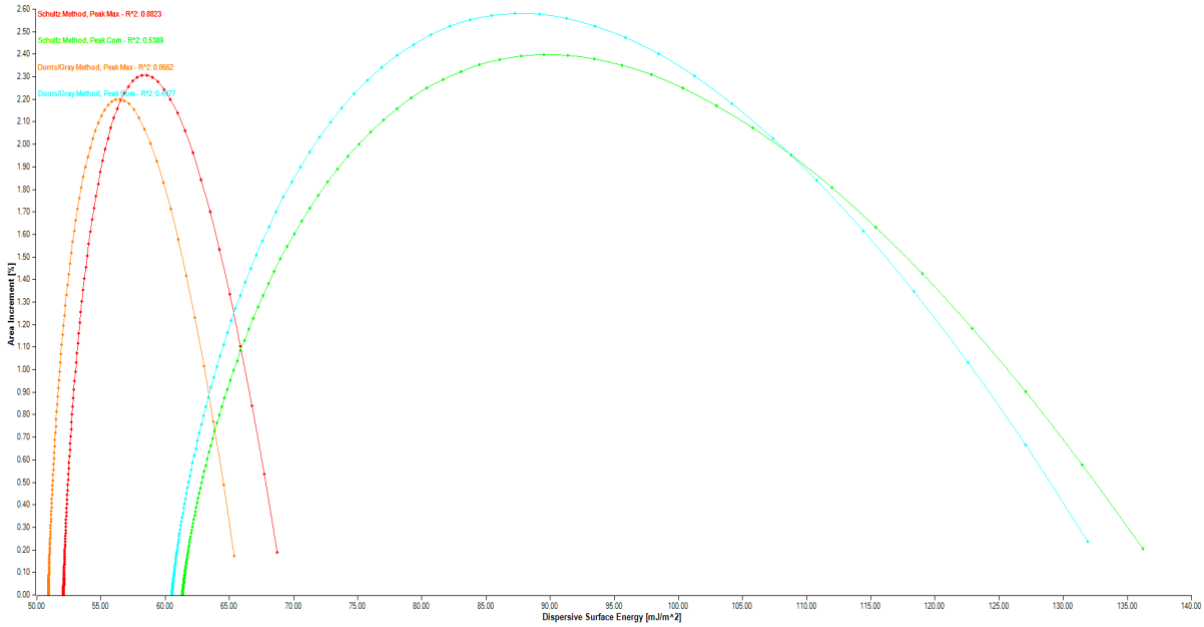

Figure 9.29. SE analysis for S2.1, dispersive surface energy distribution

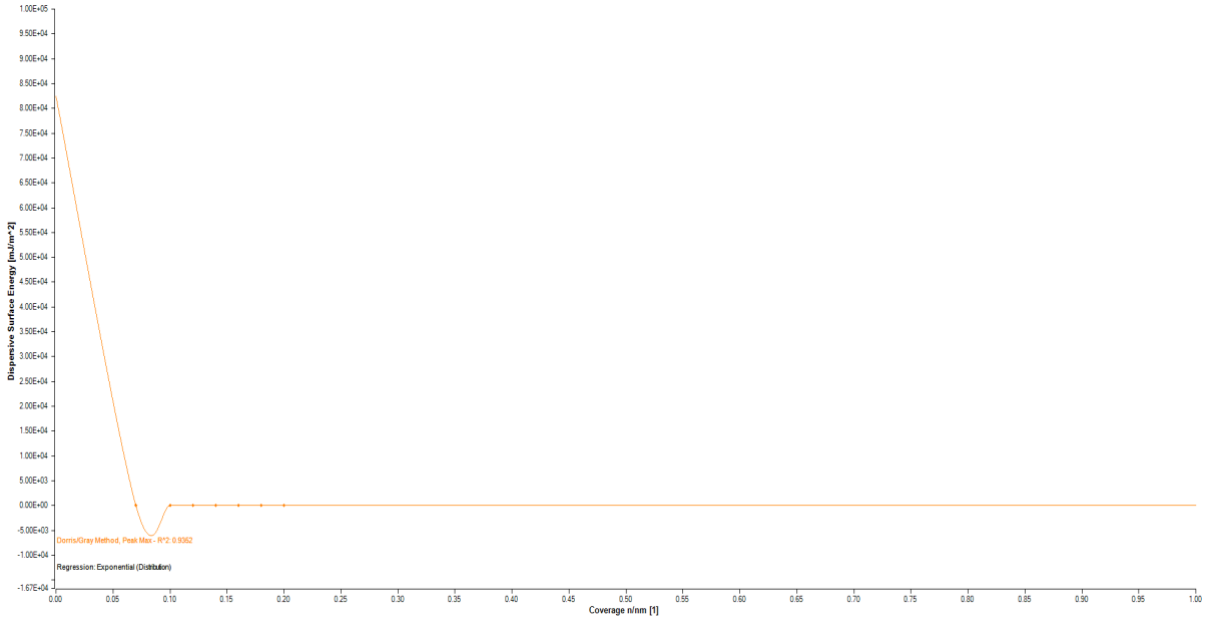

Figure 9.30. SE analysis for S2.2, dispersive surface energy

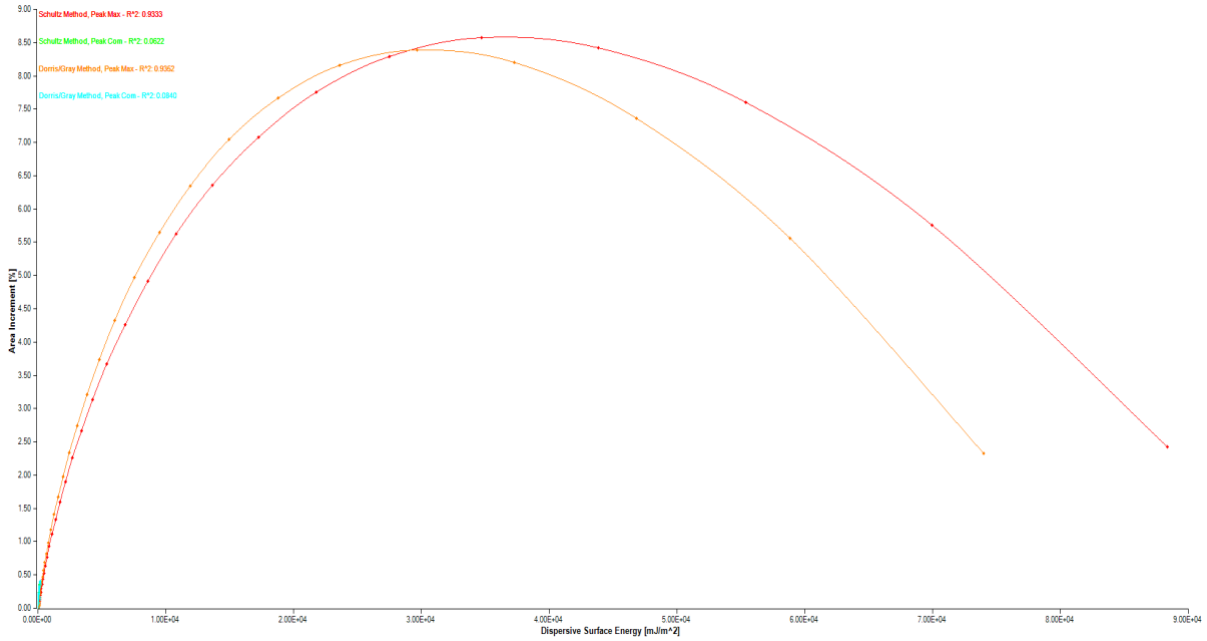

Figure 9.31. SE analysis for S2.2, dispersive surface energy distribution

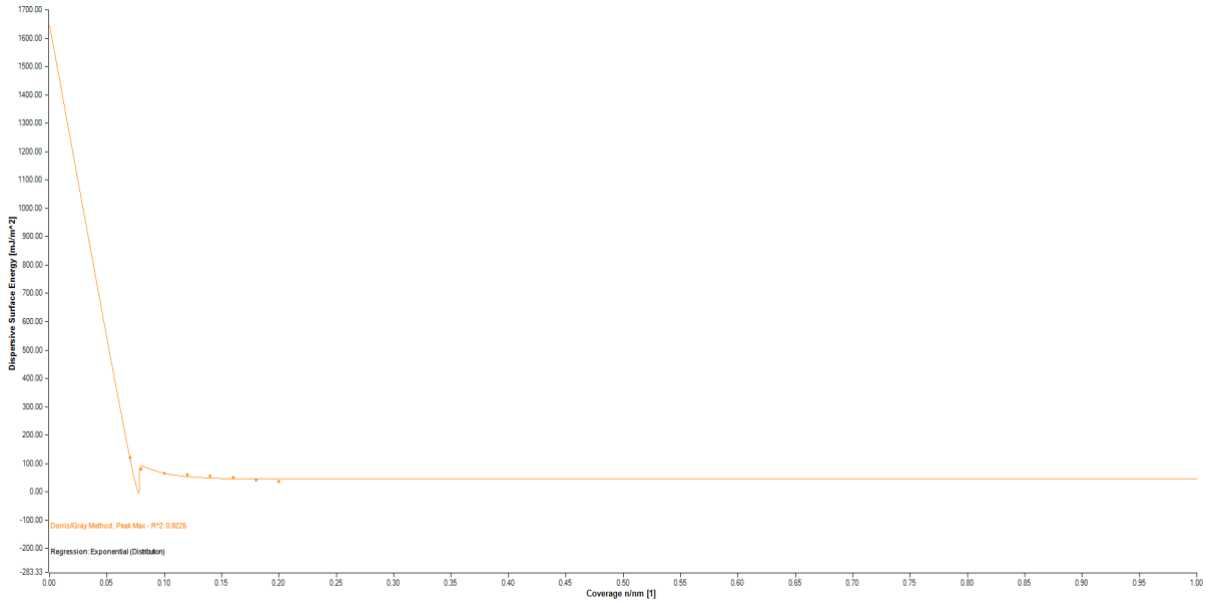

Figure 9.32. SE analysis for S3.2, dispersive surface energy

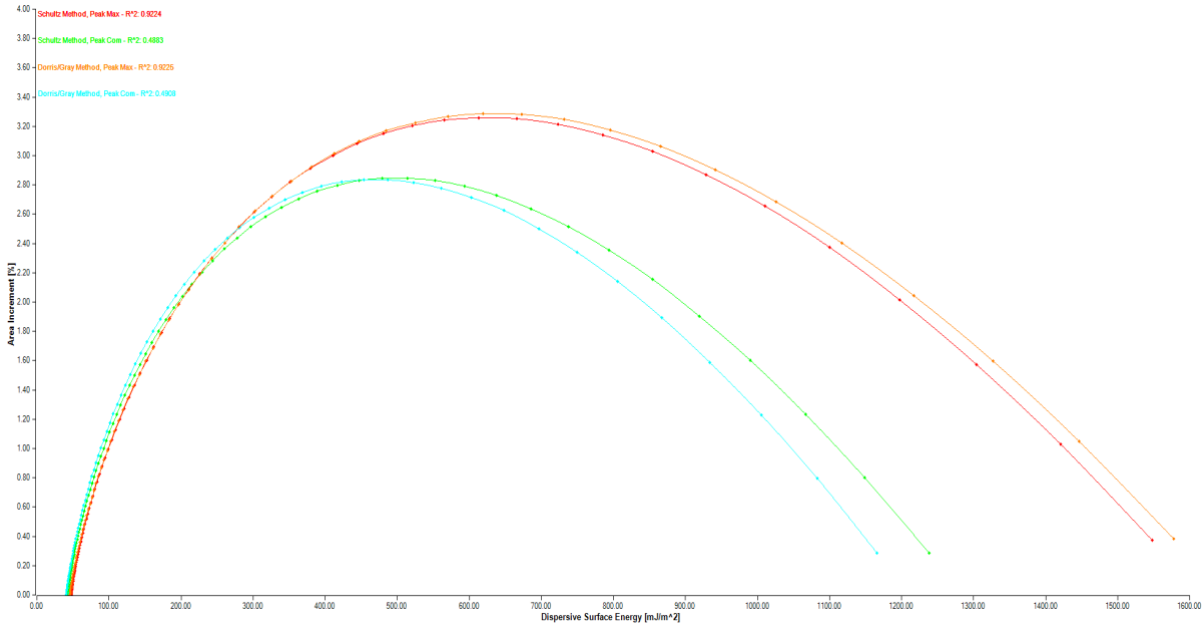

Figure 9.33. SE analysis for S3.2, dispersive surface energy distribution

Appendix C : Statistical Analyses

Ring Shear Tester

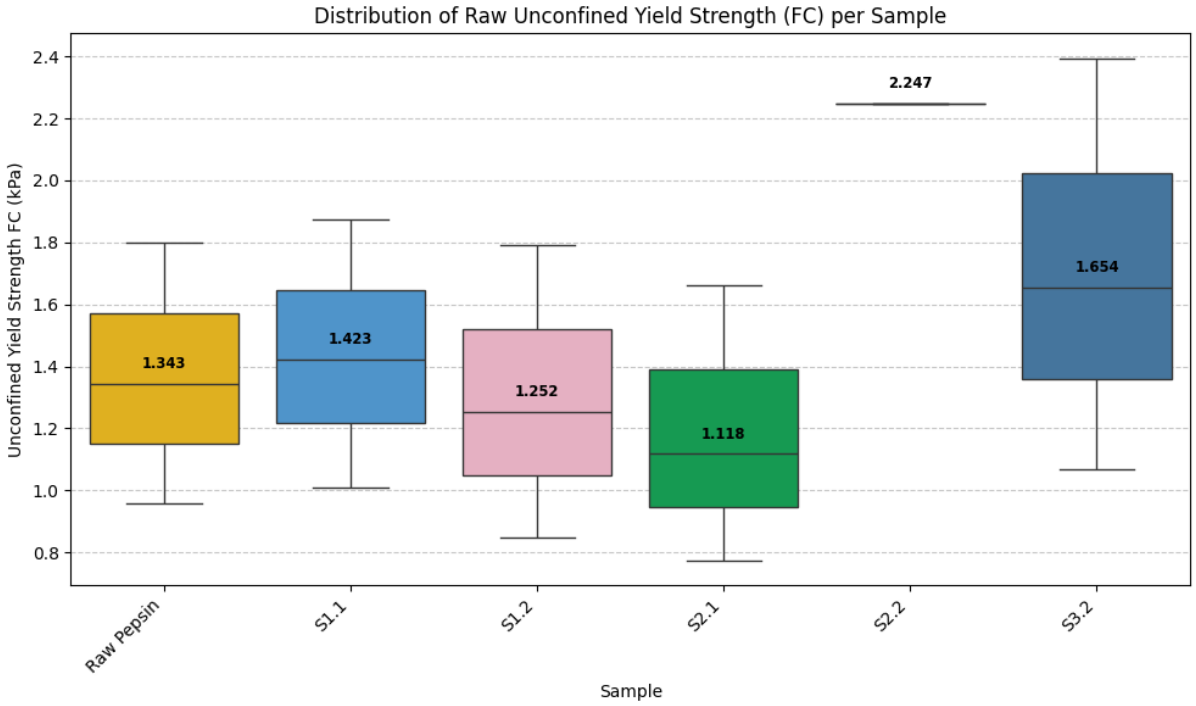

Figure 9.34. Boxplot of all ring shear tester data for each of the samples including their medians.

Table 9.3. Non-parametric Kruskal-Wallis statistical test performed on all sample medians.

Kruskal-Wallis H-Statistic	3.5000
Kruskal-Wallis p-value	0.6234

Dissolution

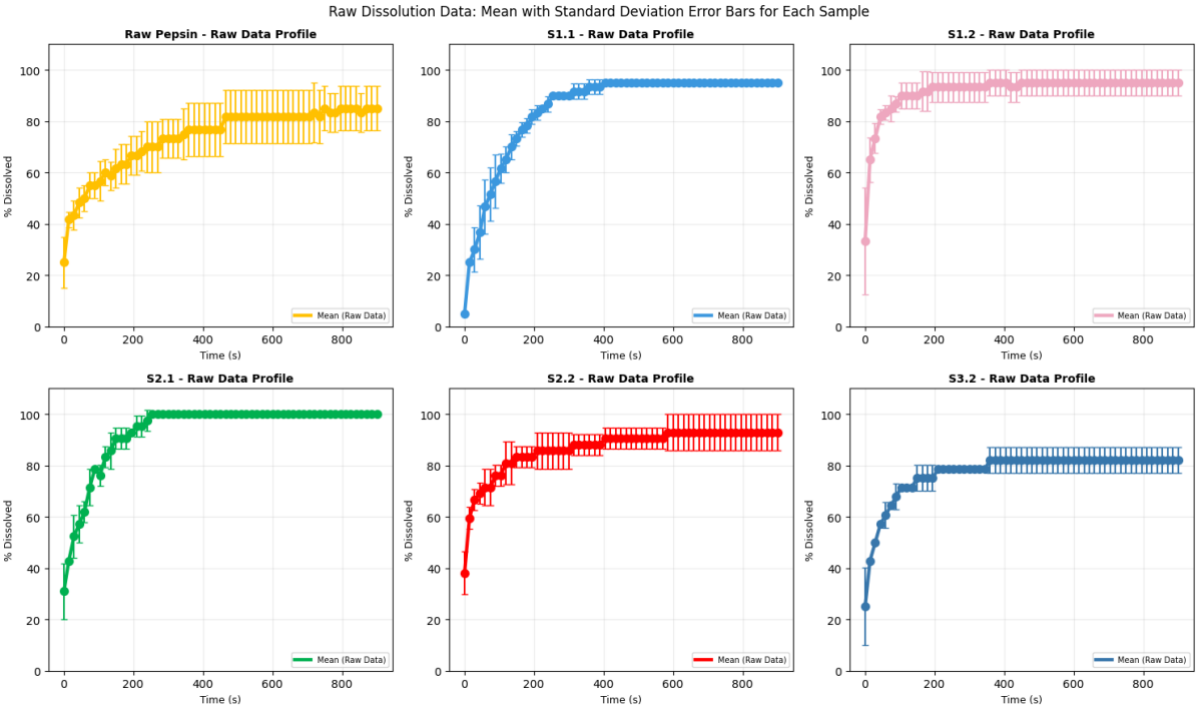

Figure 9.35. Mean % dissolution results for in vitro dissolution for all six samples. The error bars shown represent the standard deviation for each data set.

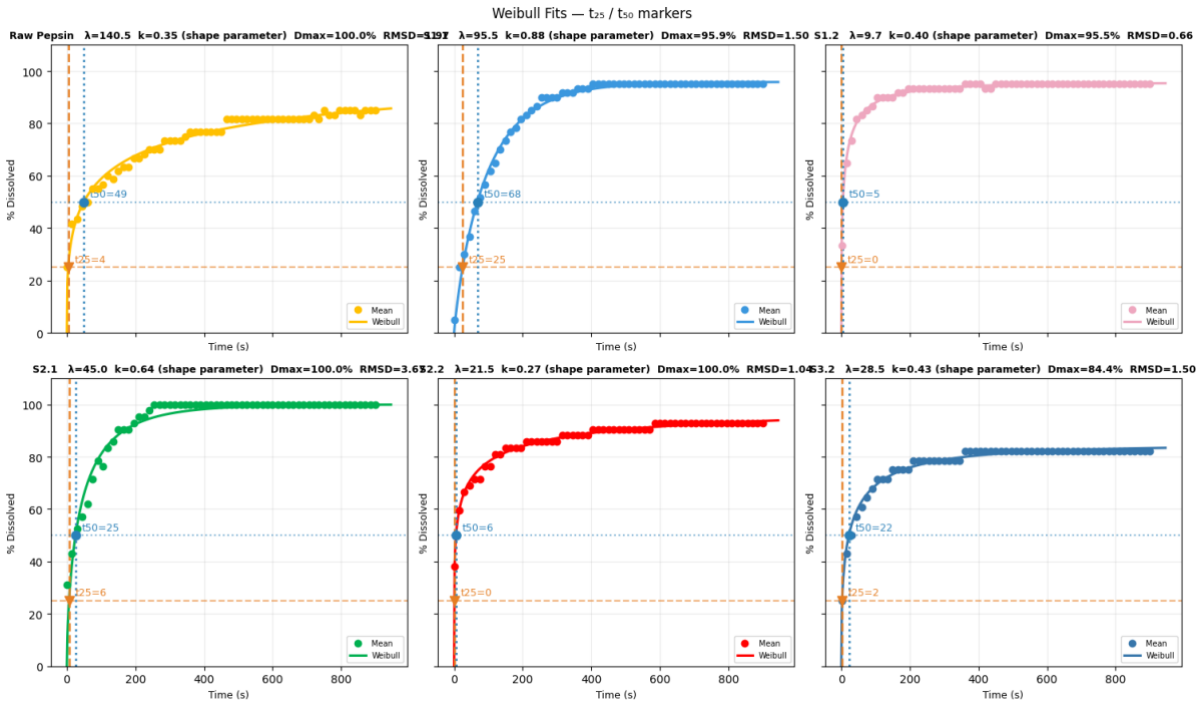

Figure 9.36. Fit of Weibull model for all six samples alongside the calculated t25 and t50 data representing the time at which 25% or 50% of the sample was dissolved. The RMSD is shown above each plot representing the difference between calculated and raw data for each of the samples.

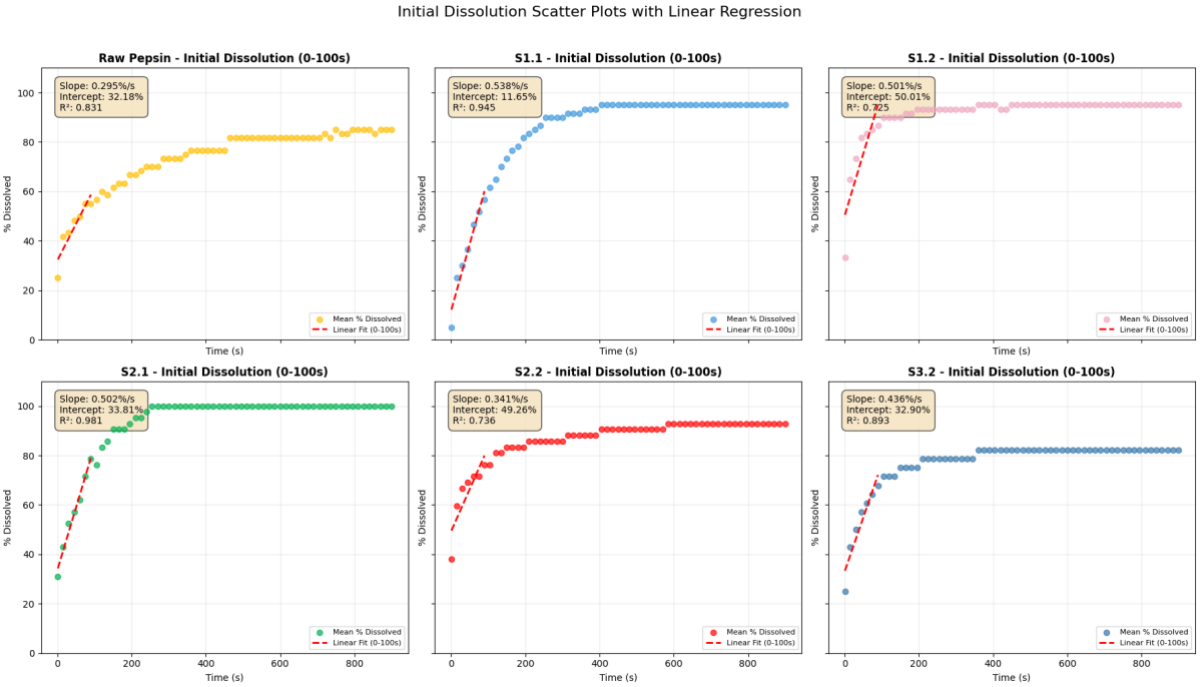

Figure 9.37. Initial dissolution curves representing the first 100 seconds of dissolution for each of the six samples. The slope, intercept and r^2 are shown for each of the data sets.

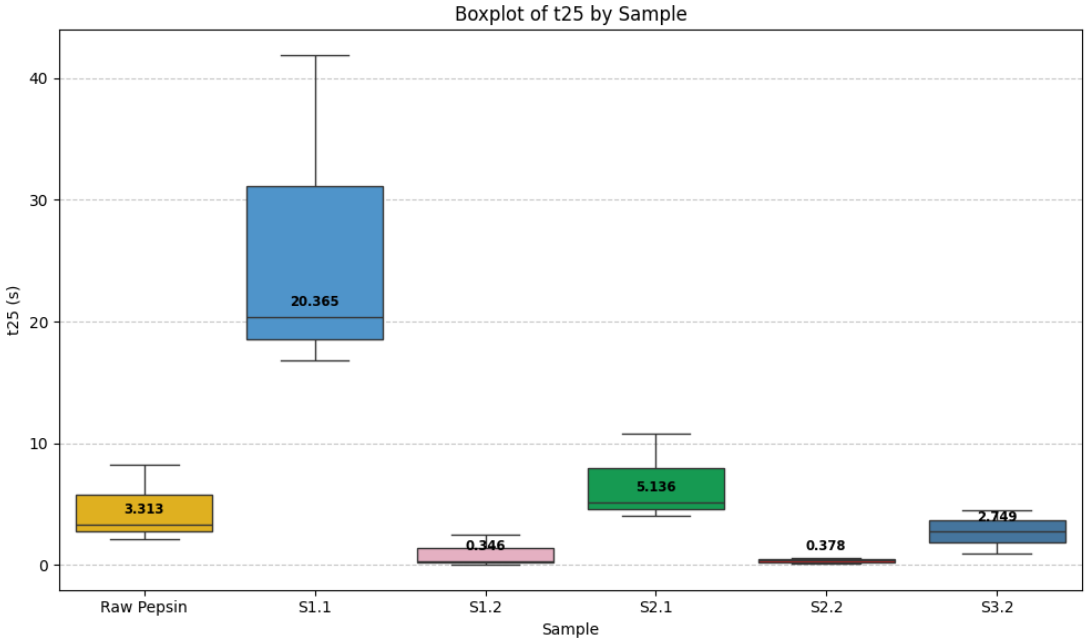

Figure 9.38. Boxplot of all t25 data for each of the samples including their medians.

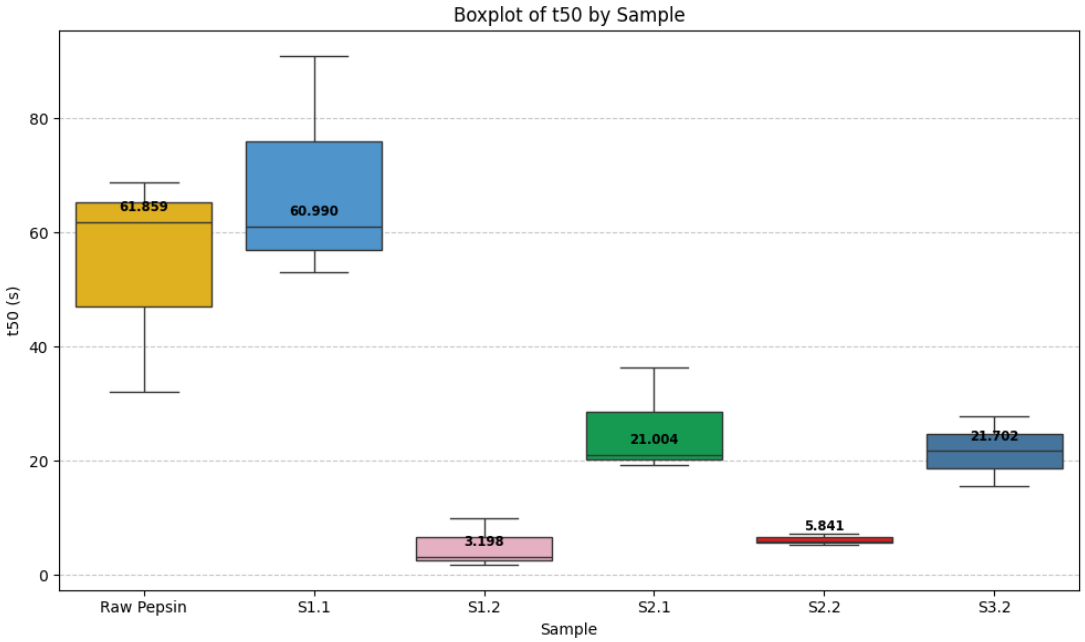

Figure 9.39. Boxplot of all t50 data for each of the samples including their medians.

Table 9.4. For lambda

Kruskal-Wallis H-Statistic	13.18
Kruskal-Wallis p-value	0.022

Table 9.5. For t25

Kruskal-Wallis H-Statistic	13.97
Kruskal-Wallis p-value	0.016

Table 9.6. For t50

Kruskal-Wallis H-Statistic	9.59
Kruskal-Wallis p-value	0.088

Table 9.7. For initial slope

Kruskal-Wallis H-Statistic	15.06
Kruskal-Wallis p-value	0.010

Appendix D: Python Code

Ring Shear Tester

```
#Importing all necessary packages and defining variables.
import numpy as np
import matplotlib.pyplot as plt
from scipy.stats import linregress
import pandas as pd
import matplotlib.pyplot as plt
import seaborn as sns
from scipy.stats import kruskal
import numpy as np
import matplotlib.pyplot as plt

#The sample data is given such that the two values represent the major
principal consolidation stress (σ₁, kPa) and the unconfined yield
strength (FC, kPa), in that order.
samples_data = {
    'Raw Pepsin':[(1.546, 0.957), (2.551, 1.343), (4.023, 1.800)],
    'S1.1':[(1.559, 1.011), (2.520, 1.423), (3.935, 1.872)],
    'S1.2':[(1.528, 0.846), (2.661, 1.252), (4.248, 1.792)],
    'S2.1':[(1.427, 0.775), (2.264, 1.118), (3.581, 1.662)],
    'S2.2':[(3.606, 2.247)],
    'S3.2':[(1.734, 1.067),  (2.971, 1.654), (4.699, 2.393)],
}

raw_data_list = []
for sample_name, points in samples_data.items():
    for sigma1, fc in points:
        raw_data_list.append({'Sample': sample_name, 'SIGMA1 (kPa)':
sigma1, 'FC (kPa)': fc})

df_raw = pd.DataFrame(raw_data_list)

#Creating boxplots for the median FC raw data from each of the six
samples to compare all against each other
colors = {
    'Raw Pepsin': '#FFC000',
    'S1.1': '#3B97DE',
    'S1.2': '#EEA7BF',
```

```
    'S2.1': '#00B050',
    'S2.2': '#FF0000',
    'S3.2': '#3776AB',
}

plt.figure(figsize=(10, 6))
sns.boxplot(x='Sample', y='FC (kPa)', data=df_raw, palette=colors,
hue='Sample', legend=False)

plt.ylabel('Unconfined Yield Strength FC (kPa)')
plt.xlabel('Sample')
plt.title('Distribution of Raw Unconfined Yield Strength (FC) per
Sample')
plt.grid(axis='y', linestyle='--', alpha=0.7)
plt.xticks(rotation=45, ha='right')

# Calculate medians for annotation
medians = df_raw.groupby('Sample')['FC (kPa)'].median()

# Add median annotations to the boxplot
for i, sample in enumerate(medians.index):
    median_val = medians[sample]
    plt.text(i, median_val + 0.05, f'{median_val:.3f}',
             horizontalalignment='center', size='small', color='black',
weight='semibold')

plt.tight_layout()
plt.show()

# Extract FC values for each sample from samples_raw_fc
fc_values_for_kruskal = [data for data in samples_raw_fc.values() if
len(data) > 0]

# Performing Kruskal-Wallis H-test as the statistical analyses since
normality cannot be accurately calculated considering the small data
pool
h_statistic, p_value_kruskal = kruskal(*fc_values_for_kruskal)

print(f"Kruskal-Wallis H-statistic: {h_statistic:.4f}")
print(f"Kruskal-Wallis p-value: {p_value_kruskal:.4f}")

#Interpolating FFC at a single consolidation stress to be able to
compare all samples against each other
target_stress = 3.606  # kPa

#Every FFC value corresponds to a differrent flow system as described
below
def classify_ffc(ffc):
    if ffc < 1:    return 'Not flowing'
```

```
    elif ffc < 2:  return 'Very cohesive'
    elif ffc < 4:  return 'Cohesive'
    elif ffc < 10: return 'Easy-flowing'
    else:          return 'Free-flowing'

regressions = {}   # store slope/intercept for plotting
summary     = []  # store results for table

for name, points in samples_data.items():
    sigma_vals = np.array([p[0] for p in points])
    fc_vals    = np.array([p[1] for p in points])

    if len(points) < 2:
        print(f" {name}: only 1 data point, interpolation not
possible")
        regressions[name] = None
        summary.append({
            'Sample':         name,
            'SIGMA1 (kPa)':   'N/A',
            'FC at 3.6 kPa':  'N/A',
            'FFC at 3.6 kPa': 'N/A',
            'Flowability':    'N/A',
            'R²':             'N/A'
        })
        continue

    # Calculate slope for regression through the origin (y = mx)
    # The formula for slope 'm' is sum(xi*yi) / sum(xi^2)
    slope = np.sum(sigma_vals * fc_vals) / np.sum(sigma_vals**2)
    intercept = 0.0 # Force intercept to zero

    # Calculate R-squared for regression through the origin
    y_predicted = slope * sigma_vals
    ss_residual = np.sum((fc_vals - y_predicted)**2)
    ss_total = np.sum((fc_vals - np.mean(fc_vals))**2)

    if ss_total > 0:
        r_squared = 1 - (ss_residual / ss_total)
    else:
        r_squared = 1.0 if ss_residual == 0 else 0.0 # Handle case if
ss_total is zero

    regressions[name] = (slope, intercept, r_squared) # Store slope,
intercept, and r_squared

    fc_interp  = slope * target_stress + intercept
    ffc_interp = target_stress / fc_interp
```

```
#Sample S2.2 was exluded from interpolation analysis as only one data
point was obtained
    summary.append({
        'Sample':         name,
        'SIGMA1 (kPa)':   target_stress,
        'FC at 3.6 kPa':  round(fc_interp, 4),
        'FFC at 3.6 kPa': round(ffc_interp, 4),
        'Flowability':    classify_ffc(ffc_interp),
        'R²':             round(r_squared, 4)
    })

df_summary = pd.DataFrame(summary)
print("\nDescriptive Summary at σ₁ = 3.6 kPa:")
print("=" * 65)
print(df_summary.to_string(index=False))

#Plotting all the raw data and interpolated FC points for all six
samples
x_max   = 5.5
x_range = np.linspace(0, x_max, 200)

colors = {
    'Raw Pepsin': '#FFC000',
    'S1.1':'#3B97DE',
    'S1.2':'#EEA7BF',
    'S2.1':'#00B050',
    'S2.2':'#FF0000',
    'S3.2':'#001965',
}

fig, ax = plt.subplots(figsize=(6, 6))

# FFC boundary lines to represent the different types of flow exhibited
by each of the samples
y_limit_top = 3.5 # From ax.set_ylim(0, 3.5)
x_limit_right = x_max # From ax.set_xlim(0, x_max)

for ffc_val, label_text in [(1, 'FFC=1'), (2, 'FFC=2'),
                        (4, 'FFC=4'), (10, 'FFC=10')]:
    ax.plot(x_range, x_range / ffc_val,
            color='grey', linewidth=0.8, linestyle='--', zorder=1)

    # Label position for the FFC values
    y_at_x_max = x_limit_right / ffc_val

    if y_at_x_max <= y_limit_top:
        # If the line reaches x_max within y_limit_top, place label
near x_max
```

```
        label_x_pos = x_limit_right * 0.98 # A little inside the right
edge
        label_y_pos = label_x_pos / ffc_val
        ax.text(label_x_pos, label_y_pos, label_text,
                fontsize=8, color='grey', va='center', ha='right')
    else:
        # If the line exits vertically before reaching x_max, place
label near y_limit_top
        label_y_pos = y_limit_top * 0.98 # A little below the top edge
        label_x_pos = label_y_pos * ffc_val # calculate x from y = x /
ffc_val
        ax.text(label_x_pos, label_y_pos, label_text,
                fontsize=8, color='grey', va='top', ha='left') #
va='top' to align top of text with y_pos

# Plotting each sample
for name, points in samples_data.items():
    sigma_vals = np.array([p[0] for p in points])
    fc_vals    = np.array([p[1] for p in points])
    color      = colors[name]

    if regressions[name] is not None:
        slope, intercept, r_squared_val = regressions[name] # Unpack
all three

        # Regression line
        ax.plot(x_range, slope * x_range + intercept,
                color=color, linewidth=2, zorder=3,
                label=f'{name} (R²={r_squared_val:.3f})') # Use
r_squared_val for label

        # Measured points
        ax.scatter(sigma_vals, fc_vals,
                   color=color, s=60, zorder=5,
                   edgecolors='white', linewidths=0.5)

        # Interpolated point at 3.606 kPa
        fc_interp = slope * target_stress + intercept
        ax.scatter(target_stress, fc_interp,
                   color=color, s=150, marker='*', zorder=6)

    else:
        # S2.2 — single point only, no line
        ax.scatter(sigma_vals, fc_vals,
                   color=color, s=100, zorder=5,
                   edgecolors='white', linewidths=0.5,
                   label=f'{name} (single point)')

# Formatting of the graph area
```

```
ax.set_xlim(0, x_max)
ax.set_ylim(0, 3.5)
ax.set_xlabel('Major Principal Consolidation Stress σ₁ (kPa)',
fontsize=12)
ax.set_ylabel('Unconfined Yield Strength FC (kPa)', fontsize=12)
ax.set_title('Ring Shear Tester'
             '(● = measured points, ★ = interpolated at 3.6 kPa)',
             fontsize=12, fontweight='bold')
ax.legend(loc='upper left', fontsize=9)
ax.grid(True, alpha=0.3)

plt.tight_layout()
plt.show()
```

Dissolution

```
#Importing all required packages necessary for the analysis of
dissolution data
import numpy as np
import pandas as pd
import matplotlib.pyplot as plt
from scipy.optimize import curve_fit
from scipy.stats import f_oneway, sem
import re

#Importing the raw dissolution data file. The data within such can be
seen in Table _ in Appendix A.
FILE          = "/content/Dissolution.xlsx"
N_SAMPLES     = 6
N_REPS        = 3
SAMPLE_LABELS = ['Raw Pepsin', 'S1.1', 'S1.2', 'S2.1', 'S2.2', 'S3.2']
INITIAL_DISSO    = 100

COLORS = plt.cm.tab10(np.linspace(0, 0.62, N_SAMPLES))

#Plotting all raw data for each sample including standard deviation
depicted with errror bars
fig, axes = plt.subplots(2, 3, figsize=(15, 9))

# Defining colors
colors_map = {
    'Raw Pepsin': '#FFC000',
    'S1.1':'#3B97DE',
    'S1.2':'#EEA7BF',
    'S2.1':'#00B050',
    'S2.2':'#FF0000',
    'S3.2':'#3776AB',
    }

for idx, (samp, ax) in enumerate(zip(SAMPLE_LABELS, axes.flatten())):
```

```
    c = colors_map.get(samp)
    mu = mean_pct[samp]
    sd = sd_pct[samp]

    # Plot the mean line explicitly with increased thickness
    ax.plot(time, mu, "-", color=c, lw=3, zorder=5, label="Mean (Raw
Data)")

    # Plot individual data points as scatter points
    ax.scatter(time, mu, color=c, s=50, zorder=6)

    # Adding error bars
    ax.errorbar(time, mu, yerr=sd, fmt='none', ecolor=c, capsize=3,
zorder=4)

    ax.set_title(f"{samp} - Raw Data Profile", fontsize=10,
fontweight="bold")
    ax.set_xlabel("Time (s)", fontsize=9)
    ax.set_ylabel("% Dissolved", fontsize=9)
    ax.legend(fontsize=7, loc="lower right")
    ax.grid(alpha=0.25)
    ax.set_ylim(0, 110) # Set y-axis limit from 0 to 110
    ax.tick_params(labelleft=True, labelbottom=True) # Explicitly show
tick labels for all subplots

plt.suptitle(
    "Raw Dissolution Data: Mean with Standard Deviation Error Bars for
Each Sample",
    fontsize=12
)
plt.tight_layout()
plt.savefig("05_raw_data_profiles.png", dpi=150, bbox_inches="tight")
plt.show()

#Plotting the average % Dissolved for each of the samples based on
Table _ in Appendix A.
fig, ax = plt.subplots(figsize=(9, 6))

# Defining colors
colors_map = {
    'Raw Pepsin': '#FFC000',
    'S1.1':'#3B97DE',
    'S1.2':'#EEA7BF',
    'S2.1':'#00B050',
    'S2.2':'#FF0000',
    'S3.2':'#3776AB',
    }

for idx, samp in enumerate(SAMPLE_LABELS):
```

```
    c = colors_map.get(samp)
    mu = mean_pct[samp]
    sd = sd_pct[samp]
    p  = mean_fits[samp]

    ax.plot(time, mu, "o", color=c, ms=5, alpha=0.8)
    y_fit = weibull(t_fine, p["lambda"], p["k"], p["Dmax"])
    ax.plot(t_fine, y_fit, "-", color=c, lw=2,
            label=f"{samp}")

ax.set_xlabel("Time (s)", fontsize=11)
ax.set_ylabel("% Dissolved", fontsize=11)
ax.set_title("All Samples – Mean Profiles + Weibull Fits", fontsize=13)
ax.legend(fontsize=8.5, title="Sample", title_fontsize=9)
ax.grid(alpha=0.25)
ax.set_ylim(0, 110)
plt.tight_layout()
plt.savefig("02_all_samples_overlay.png", dpi=150, bbox_inches="tight")
plt.show()

#Organizing the data file and making sure the system is reading it
correctly
raw  = pd.read_excel(FILE, sheet_name=0)
time = raw.iloc[:, 0].values.astype(float)

data = {}
sample_n_reps = {}

# Storing information on columnn names based on the raw data file
all_cols = raw.columns.tolist()

#Ensuring the system can correctly identify the column names
for samp in SAMPLE_LABELS:
    sample_cols = []
    samp_regex_part = samp.replace('.', '\\.')
    pattern = rf"^{samp_regex_part} ?% Dissolved\.\d+$"

    for col in all_cols:
        if re.match(pattern, col):
            sample_cols.append(col)

    # Sorting columns in consecutive order of replicates
    sample_cols.sort()
    sample_n_reps[samp] = len(sample_cols)
    data[samp] = raw[sample_cols].values.astype(float) # shape (T, R)

mean_pct = {s: data[s].mean(axis=1) for s in SAMPLE_LABELS if s in
data}
```

```
#Defining the Weibull model equation
def weibull(t, lam, k, dmax):
    return dmax * (1.0 - np.exp(-((t / lam) ** k)))

#Defining the tx function used to calculate the time taken to reach a
certain dissolution percentage (t25, t50)
def tx(lam, k, dmax, x_pct):
    if x_pct >= dmax:
        return np.nan
    return lam * (-np.log(1.0 - x_pct / dmax)) ** (1.0 / k)

#Defining the initial dissolution rate as performed by a linear fit on
the early data points
def initial_slope(t, y, cutoff):
    """
    Linear slope over 0–cutoff. Returned alongside a warning flag
    if k deviates from 1 (where it's least reliable).
    """
    mask = t <= cutoff
    if mask.sum() < 2:
        return np.nan
    return max(float(np.polyfit(t[mask], y[mask], 1)[0]), 0.0)

#Giving a certain fit to given time and dissolution data by applying
bounds.
def fit_weibull(t, y):
    y_max = float(np.nanmax(y))

#The upper bound for Dmax is set to  100.0
    p0    = [float(np.median(t[t > 0])), 1.0, min(max(y_max * 1.05,
80.0), 100.0)]
    bnds  = (
        [t[t > 0].min() * 0.01, 0.10, y_max * 0.50],
        [t.max() * 20.0,        10.0,         100.0],
            )
    try:
        return curve_fit(weibull, t, y, p0=p0, bounds=bnds,
maxfev=30000)
    except RuntimeError:
        return None, None

#Applying the functions defined above to the mean percentage
dissolution data for each sample and storing all obtained data
mean_fits = {}

for samp in SAMPLE_LABELS:
    t = time
```

```
    y = mean_pct[samp]
    popt, pcov = fit_weibull(t, y)
    if popt is None:
        print(f"WARNING: mean fit failed for {samp}")
        continue
    lam, k, dmax = popt
    se = np.sqrt(np.diag(pcov))
    slope = initial_slope(t, y, INITIAL_DISSO)

    mean_fits[samp] = {
        "lambda": lam, "lambda_SE": se[0],
        "k"     : k,   "k_SE"     : se[1],
        "Dmax"  : dmax,"Dmax_SE"  : se[2],
        "t25"   : tx(lam, k, dmax, 25),
        "t50"   : tx(lam, k, dmax, 50),
        "init_slope"  : slope,
    }

#Calculating the Root Mean Square Deviation (RMSD) for each of the
sample's mean Weibull fit
import numpy as np

SAMPLE_LABELS = ['Raw Pepsin', 'S1.1', 'S1.2', 'S2.1', 'S2.2', 'S3.2']

def weibull(t, lam, k, dmax):
    return dmax * (1.0 - np.exp(-((t / lam) ** k)))

def calculate_rmsd(t_obs, y_obs, lam, k, dmax):
    """Calculates the Root Mean Square Deviation between observed data
and Weibull fit."""
    y_fit = weibull(t_obs, lam, k, dmax)
    rmsd = np.sqrt(np.mean((y_obs - y_fit)**2))
    return rmsd

for samp in SAMPLE_LABELS:
    if samp in mean_fits:
        p = mean_fits[samp]
        rmsd_val = calculate_rmsd(time, mean_pct[samp], p["lambda"],
p["k"], p["Dmax"])
        mean_fits[samp]["RMSD"] = rmsd_val

#Applying the Weibull sample to each individual replicate of each
sample instead of just the mean.
rep_rows = []

for samp in SAMPLE_LABELS:
    if samp not in sample_n_reps or sample_n_reps[samp] == 0:
        print(f"Skipping sample {samp}: No replicate data or replicates
found.")
```

```
        continue

    for r in range(sample_n_reps[samp]):
        t = time
        y = data[samp][:, r]
        popt, _ = fit_weibull(t, y)
        if popt is None:
            print(f"Warning: Replicate fit failed for {samp} R{r+1}")
            continue
        lam, k, dmax = popt
        rep_rows.append({
            "Sample": samp, "Replicate": f"R{r+1}",
            "lambda": lam, "k": k, "Dmax": dmax,
            "t25"   : tx(lam, k, dmax, 25),
            "t50"   : tx(lam, k, dmax, 50),
            "init_slope": initial_slope(t, y, INITIAL_DISSO),
        })

#Importing packages to plot the data calculated above
import numpy as np
import pandas as pd
import matplotlib.pyplot as plt
from scipy.optimize import curve_fit
from scipy.stats import f_oneway, sem

t_fine = np.linspace(0, time.max() * 1.05, 600)
TX_STYLES = {
    "t25": ("--", "v", 25, "#e67e22"),
    "t50": (":" , "o", 50, "#2980b9"),
}

fig, axes = plt.subplots(2, 3, figsize=(15, 9), sharey=True,
sharex=True)

# Defining colors
colors_map = {
    'Raw Pepsin': '#FFC000',
    'S1.1':'#3B97DE',
    'S1.2':'#EEA7BF',
    'S2.1':'#00B050',
    'S2.2':'#FF0000',
    'S3.2':'#3776AB',
    }

for idx, (samp, ax) in enumerate(zip(SAMPLE_LABELS, axes.flatten())):
  c = colors_map.get(samp)

  if samp not in mean_pct or samp not in mean_fits:
```

```
        ax.set_title(f"{samp} (Data Not Available)", fontsize=9,
fontweight="bold")
        ax.set_xlabel("Time (s)", fontsize=9)
        ax.set_ylabel("% Dissolved", fontsize=9)
        ax.grid(alpha=0.25)
        continue

  mu = mean_pct[samp]
  p  = mean_fits[samp]
  ax.plot(time, mu, "o", color = c, ms=6, zorder=5, label="Mean") #
Fixed: use specific color 'c'

  y_fit = weibull(t_fine, p["lambda"], p["k"], p["Dmax"])
  ax.plot(t_fine, y_fit, "-", color = c, lw=2.2, label="Weibull") #
Fixed: use specific color 'c'

  # Marking t25, t50 on both axes
  for key, (ls, mk, lvl, mc) in TX_STYLES.items():
        t_val = p[key]
        if np.isnan(t_val):
            continue
        ax.axvline(t_val, ls=ls, color=mc, lw=2.0, alpha=0.9)
        ax.axhline(lvl,   ls=ls, color=mc, lw=1.5, alpha=0.6)
        ax.plot(t_val, lvl, marker=mk, color=mc, markersize=8,
zorder=10)
        ax.text(t_val + time.max() * 0.02, lvl + 2.0,
                f"{key}={t_val:.0f}", fontsize=9, color=mc)

  rmsd_text = f"  RMSD={p['RMSD']:.2f}" if 'RMSD' in p else ""
  ax.set_title(
        f"{samp}   λ={p['lambda']:.1f}  k={p['k']:.2f} ({k_note})
Dmax={p['Dmax']:.1f}%" + rmsd_text,
        fontsize=9, fontweight="bold"
    )
  ax.set_xlabel("Time (s)", fontsize=9)
  ax.set_ylabel("% Dissolved", fontsize=9)
  ax.legend(fontsize=7, loc="lower right")
  ax.grid(alpha=0.25)
  ax.set_ylim(0, 110)

plt.suptitle(
    "Weibull Fits — t₂₅ / t₅₀ ",
    fontsize=12
)
plt.tight_layout()
plt.savefig("01_weibull_mean_fits.png", dpi=150, bbox_inches="tight")
plt.show()

#Plotting all initial slope figures for each of the samples
```

```
from scipy.stats import linregress

fig, axes = plt.subplots(2, 3, figsize=(18, 10), sharey=True,
sharex=True)

# Defining colors
colors_map = {
    'Raw Pepsin': '#FFC000',
    'S1.1':'#3B97DE',
    'S1.2':'#EEA7BF',
    'S2.1':'#00B050',
    'S2.2':'#FF0000',
    'S3.2':'#3776AB',
    }

for idx, (samp, ax) in enumerate(zip(SAMPLE_LABELS, axes.flatten())):
    c = colors_map.get(samp)
    mu = mean_pct[samp]

    # Plot all raw data points as scatter
    ax.scatter(time, mu, color=c, label='Mean % Dissolved', alpha=0.7,
zorder=5)

    # Filter data for initial dissolution time points for linear
regression
    mask = time <= INITIAL_DISSO
    t_initial = time[mask]
    y_initial = mu[mask]

    if len(t_initial) > 1:
        slope, intercept, r_value, p_value, std_err =
linregress(t_initial, y_initial)
        r_squared = r_value**2

        # Plot the regression line only within the initial dissolution
time frame (100 seconds)
        t_reg = np.array([t_initial.min(), t_initial.max()])
        y_reg = intercept + slope * t_reg
        ax.plot(t_reg, y_reg, color='red', linestyle='--', linewidth=2,
                label=f'Linear Fit (0-{INITIAL_DISSO}s)', zorder=6)

        # Adding regression lines to the plot
        ax.text(0.05, 0.95, f'Slope: {slope:.3f}%/s\nIntercept:
{intercept:.2f}%\nR²: {r_squared:.3f}',
                transform=ax.transAxes, fontsize=10,
verticalalignment='top', bbox=dict(boxstyle='round,pad=0.5',
fc='wheat', alpha=0.7))
    else:
```

```
        ax.text(0.5, 0.5, 'Not enough data for linear regression in
early phase',
                transform=ax.transAxes, fontsize=10,
verticalalignment='center', horizontalalignment='center', color='gray')


    ax.set_title(f'{samp} - Initial Dissolution (0-{INITIAL_DISSO}s)',
fontsize=12, fontweight='bold')
    ax.set_xlabel('Time (s)', fontsize=10)
    ax.set_ylabel('% Dissolved', fontsize=10)
    ax.grid(alpha=0.25)
    ax.set_ylim(0, 110) # Set y-axis limit to 0-110
    ax.legend(fontsize=8, loc='lower right')

plt.suptitle('Initial Dissolution Scatter Plots with Linear
Regression', fontsize=16, y=1.02)
plt.tight_layout()
plt.savefig("07_initial_dissolution_scatter_regression.png", dpi=150,
bbox_inches="tight")
plt.show()

summary_rows = []
for samp in SAMPLE_LABELS:
    mf = mean_fits[samp] # mean fit data

    summary_rows.append({
        "Sample": samp,
        "λ": f"{mf['lambda']:.2f}",
        "k": f"{mf['k']:.2f}",
        "Dmax (%)": f"{mf['Dmax']:.2f}",
        "t₂₅ (s)": f"{mf['t25']:.2f}",
        "t₅₀ (s)": f"{mf['t50']:.2f}",
        "Init slope (%/s)": f"{mf['init_slope']:.2f}",
    })

summary_df = pd.DataFrame(summary_rows)
display(summary_df)

import seaborn as sns
import itertools
from scipy.stats import mannwhitneyu
import matplotlib.pyplot as plt

#Creating boxplot showing medians for both t25 and t50 data
metrics_to_analyze = ['t25', 't50']

colors = {
    'Raw Pepsin': '#FFC000',
    'S1.1':'#3B97DE',
```

```
    'S1.2':'#EEA7BF',
    'S2.1':'#00B050',
    'S2.2':'#FF0000',
    'S3.2':'#3776AB',
}

for metric in metrics_to_analyze:
    plt.figure(figsize=(10, 6))
    ax = sns.boxplot(x='Sample', y=metric, data=rep_df, palette=colors,
hue='Sample', legend=False)
    plt.xlabel('Sample')
    plt.ylabel(f'{metric} (s)')
    plt.title(f'Boxplot of {metric} by Sample')
    plt.grid(axis='y', linestyle='--', alpha=0.7)

    # Calculating medians for annotation
    medians = rep_df.groupby('Sample')[metric].median()

    # Add median annotations to the boxplot
    for i, sample in enumerate(medians.index):
        median_val = medians[sample]
        ax.text(i, median_val + (ax.get_ylim()[1] * 0.02),
f'{median_val:.3f}',
                horizontalalignment='center', size='small',
color='black', weight='semibold')

    plt.tight_layout()
    plt.show()

#Performing non-parameteric Kruskal-Wallis test on lambda, t25, t50 and
initial slope to determine significance between samples
from scipy.stats import kruskal

# Parameters to analyze with Kruskal-Wallis
kruskal_metrics = ['t25', 't50', 'init_slope', 'lambda']

for metric in kruskal_metrics:
    print(f"\nAnalyzing metric: {metric}")

    # Collecting data for all samples for the set parameters
    sample_data_for_kruskal = []
    valid_samples = []

    for samp in SAMPLE_LABELS:
        # Enough replicates must be ensured (at least 2) in each sample
to have a meaningful comparison
        if samp in sample_n_reps and sample_n_reps[samp] >= 2:
            data_points = rep_df[rep_df['Sample'] ==
samp][metric].dropna().values
```

```
            if len(data_points) > 0:
                sample_data_for_kruskal.append(data_points)
                valid_samples.append(samp)
            else:
                print(f"  Warning: No valid data points for {samp} in
{metric}. Skipping this sample.")
        else:
            print(f"  Warning: Not enough replicates for {samp}
({sample_n_reps.get(samp, 0)}) in {metric}. Skipping this sample.")

    if len(sample_data_for_kruskal) < 2:
        print(f"  Not enough valid samples (at least 2 with data) to
perform Kruskal-Wallis test for {metric}.")
        continue

    # Performing Kruskal-Wallis H-test
    try:
        h_statistic, p_value = kruskal(*sample_data_for_kruskal)
        print(f"  Kruskal-Wallis H-statistic for {metric}:
{h_statistic:.2f}")
        print(f"  P-value for {metric}: {p_value:.3f}")

        if p_value < 0.05:
            print(f"  Conclusion: Significant differences detected
between samples for {metric} (p < 0.05).")
        else:
            print(f"  Conclusion: No significant differences detected
between samples for {metric} (p >= 0.05).")
    except ValueError as e:
        print(f"  Error performing Kruskal-Wallis test for {metric}:
{e}")
```

Correlation analysis

```
#Importing necessary packages
import numpy as np
import pandas as pd
import matplotlib.pyplot as plt
import matplotlib.gridspec as gridspec
import seaborn as sns
from scipy import stats

#All data from each of the samples used for the correlation
calculations
data = {
    "Sample":["Raw Pepsin", "S1.1", "S1.2", "S2.1", "S2.2", "S3.2"],
    "D50% (um)":[36.2, 4.89, 7.54, 11.1, 11.2, 8.94],
    "Pycnometric density (g/cm3)":[1.6149, 1.5467, 1.5707, 1.5998,
1.597, 1.6263],
```

```
    "Water content (%)":[0.6, 5.2, 7.9, 3.1, 4.9, 7.6],
    "BET surface area (m2/g)":[0.6376, 1.648, 1.2312, 0.3122, 0.4565,
0.6575],
    "BET surface area iGC (m2/g)":[1.1803, 1.6476, 1.3726, 0.746665,
0.970615, 0.967767],
    "FFC":[2.0649, 1.9368, 2.2442, 2.0843, 1.6, 1.8832],
    "Hausner ratio":[1.431, 1.5, 1.359, 1.343, 1.314, 1.297],
    "λ (sec)":[140.50, 95.48, 9.69, 45.03, 21.52, 28.48],
    "T25 (sec)":[3.96, 24.68, 0.48, 6.37, 0.22, 2.45],
    "T50 (sec)":[49.19, 67.66, 4.56, 25.32, 5.59, 22.11],
    "Initial Disso (%/sec)":[0.29, 0.54, 0.50, 0.50, 0.34, 0.44],
    "Total SE (mJ/m2)":[309.53, 153.66, 278.78, 289.28, 498.54,
829.14],
    "BET x Total SE mJ/g": [365.34, 253.17, 382.65, 267.62, 549.99,
918.02],
}

df = pd.DataFrame(data).set_index("Sample")
oooo
#Since normality cannot be accurately determined, spearman correlation
is calculated
spearman_r, spearman_p = pd.DataFrame(), pd.DataFrame()

cols = df.columns.tolist()

pr_mat  = np.zeros((len(cols), len(cols)))
pp_mat  = np.zeros((len(cols), len(cols)))
sr_mat  = np.zeros((len(cols), len(cols)))
sp_mat  = np.zeros((len(cols), len(cols)))

for i, c1 in enumerate(cols):
    for j, c2 in enumerate(cols):
        pr, pp = stats.pearsonr(df[c1], df[c2])
        sr, sp = stats.spearmanr(df[c1], df[c2])
        pr_mat[i, j] = pr;  pp_mat[i, j] = pp
        sr_mat[i, j] = sr;  sp_mat[i, j] = sp

spearman_r = pd.DataFrame(sr_mat, index=cols, columns=cols)
spearman_p = pd.DataFrame(sp_mat, index=cols, columns=cols)

print("\n\nSPEARMAN CORRELATION MATRIX")
print(spearman_r.round(3).to_string())

#Creating a correlation matrix based on the Spearman data
import os

THRESHOLD = 0.7   # |r| above this gets a highlight border
```

```
#Creating a heatmap which colors the correlation value in a different
color depending on the strength
def annotate_heatmap(ax, r_df, p_df, fontsize=6.5):
    """Write r-value inside each cell.
    Cells where |r| > THRESHOLD get a gold border to flag strong
correlations.
    Self-correlation is excluded from highlighting.
    """
    n = len(r_df)
    for i in range(n):
        for j in range(n):
            r = r_df.iloc[i, j]
            p = p_df.iloc[i, j]
            strong = (abs(r) > THRESHOLD) and (i != j)
            text_color = "#333333" if strong else ("black" if abs(r) >
0.5 else "#333333")
            ax.text(j + 0.5, i + 0.5,
                    f"{r:.2f}",
                    ha="center", va="center",
                    fontsize=fontsize, color=text_color,
                    fontweight="bold" if strong else "normal")
            if strong:
                rect = plt.Rectangle((j, i), 1, 1,
                                     fill=False,
                                     edgecolor="#FFD700",
                                     linewidth=1.8,
                                     zorder=3)
                ax.add_patch(rect)

#Defining the units
SHORT = {c: c.replace(" (um)", "").replace(" (g/cm3)", "")
              .replace(" (%)", "").replace(" m2/g", "")
              .replace(" mJ/m2", "").replace(" ratio", "")
         for c in cols}
labels = [SHORT[c] for c in cols]

fig = plt.figure(figsize=(20, 9))
fig.patch.set_facecolor("white")

gs = gridspec.GridSpec(1, 3, figure=fig, width_ratios=[1, 1, 0.05],
wspace=0.35)

cmap = sns.diverging_palette(220, 20, s=80, l=45, as_cmap=True)
vmin, vmax = -1, 1

#Spearman correlation results
ax2 = fig.add_subplot(gs[1])
ax2.set_facecolor("white")
sns.heatmap(spearman_r, annot=False, cmap=cmap, vmin=vmin, vmax=vmax,
```

```
            linewidths=0.4, linecolor="#dddddd",
            xticklabels=labels, yticklabels=labels,
            ax=ax2, cbar=False, square=True)
annotate_heatmap(ax2, spearman_r, spearman_p)
ax2.set_title("Spearman Correlation", color="black", fontsize=14,
              fontweight="bold", pad=14)
ax2.tick_params(colors="black", labelsize=7.5)
plt.setp(ax2.get_xticklabels(), rotation=45, ha="right")
plt.setp(ax2.get_yticklabels(), rotation=0)

# Defining the color bar representing the different colors based on
correlation strength
cax = fig.add_subplot(gs[2])
sm = plt.cm.ScalarMappable(cmap=cmap, norm=plt.Normalize(vmin=-1,
vmax=1))
sm.set_array([])
cb = fig.colorbar(sm, cax=cax)
cb.set_label("r value", color="black", fontsize=10)
cb.ax.yaxis.set_tick_params(color="black")
plt.setp(cb.ax.yaxis.get_ticklabels(), color="black")
cax.set_facecolor("white")

# Legend below the matrix
fig.text(0.5, 0.01,
         "Cell values = r; gold border =|r| > 0.7",
         ha="center", va="bottom", color="#555555", fontsize=9)
```